ABSTRACT

LI, MENGNAN. High Resolution Boiling Simulation Using Interface Tracking Method. (Under the direction of Dr. Igor A. Bolotnov).

Boiling, as one of the most efficient heat transfer mechanisms, is widely used in various engineering systems. Better understanding and modeling of this process remains a major challenge in multiphase flow research. In light water reactor (LWR) nuclear power plants, the distribution of vapor in the reactor core sub-channels affects the heat transfer rate and may cause unfavorable conditions, such as departure from nucleate boiling (DNB) phenomenon. DNB, in turn, may cause fuel cladding damage, which may lead to reactor unplanned shutdowns and even accidents. The advances in *High-Performance Computing* (HPC) in recent years make it possible to apply direct numerical simulation (DNS) approach to a wide variety of bubble hydrodynamics and thermodynamics studies. After the interface tracking methods (ITM) are introduced to DNS, the instantaneous velocity and temperature field at, and around, the interface can be calculated in two-phase flow simulations. ITM approach provides not only detailed physical description associated with thermal and hydrodynamic processes but also the shape of the evolving interface, which may provide new insight on the understanding of boiling phenomenon and help the model development for multiphase computational fluid dynamics (M-CFD) in the near future.

The high resolution boiling simulations in the presented research are conducted in full three-dimensional (3D) transient representation with the unstructured grid. This approach allows us to investigate the boiling phenomenon in various conditions with lower computational cost (by utilizing local mesh refinement for bubble growth region). To represent more accurate contact angle during nucleate boiling, the contact angle force model developed in the research group has been coupled with the evaporation and condensation algorithm. The Bubble Tracking Algorithm (BTA) which collects the detailed information regarding the individual bubble behavior in level-

set method is brought into the evaporation and condensation model to support multi-bubble growth simulations and collect heat transfer information of interest (e.g. evaporation heat flux, bubble departure diameter, etc.) under various boiling conditions.

The verification of the evaporation and condensation model has been performed by comparing the bubble growth rate with analytical solutions. Both pool boiling and flow boiling simulations are performed with the ITM boiling model in PHASTA. The simulated bubble nucleation frequency in pool boiling simulation is validated against experimentally-based correlations. The bubble evolution and growth rate is compared with experimental data to validate the model performance under flow boiling condition. The multi-bubble flow boiling simulation explores the potential of current model in solving boiling problems with complex geometries.

The presented research lays the foundation of high resolution boiling simulation in PHASTA. To the author's best knowledge, it's the first time that an ITM-based boiling model can conduct boiling simulations with 3D unstructured mesh. Compared to the structured grid-based solvers which are challenging to apply to complex engineering geometries, this boiling model implementation is capable of conducting high resolution large scale boiling simulations in engineering geometries and resolves the detailed hydrodynamics and thermodynamics information for quantities of interest at/around the interface. It can help fulfill the numerical data gap between the local physical phenomena and the engineering scale application in the future.

High Resolution Boiling Simulation Using Interface Tracking Method

by
Mengnan Li

A dissertation submitted to the Graduate Faculty of
North Carolina State University
in partial fulfillment of the
requirements for the degree of
Doctor of Philosophy

Nuclear Engineering

Raleigh, North Carolina
2019

APPROVED BY:

Dr. Igor A. Bolotnov Committee Chair	Dr. Nam T. Dinh
Dr. J. Michael Doster	Dr. Hong Luo
Dr. W. David Pointer	

DEDICATION

To my parents and my love

BIOGRAPHY

The author graduated from Sichuan University, China with a bachelor's degree in Nuclear Engineering in 2014. She joined the nuclear engineering department of North Carolina State University in 2014 and started to work with Dr. Igor Bolotnov. She obtained her master's degree in 2016. Her research focuses on the ITM boiling model development and high resolution boiling simulation. The author is expected to continue her research in nuclear engineering.

ACKNOWLEDGEMENTS

First, I would like to thank Dr. Igor Bolotnov for guiding my research in the past four and half years. It is a greatest honor for me to be his student. His talent, knowledge and great passion on the research has deeply influenced me. I have learnt so much while working with him. During my Ph.D. study, he always has faith in me. He encourages me to push the limits and embraces bigger challenges than I think I am capable of. Beyond research, he is like a friend who is willing to share experiences and thoughts. Without his guidance and help, I would not be able to make such achievements during my Ph.D. study.

Next, I would also like to thank Dr. Nam Dinh, Dr. J. Michael Doster, Dr. W. David Pointer, and Dr. Hong Luo for serving as my committee. Your insights and suggestions are most valuable to me.

I also want to give special thanks to Dr. W. David Pointer for offering me an internship in Oak Ridge National Laboratory in 2016. Besides, I would like to thank my friends and colleagues at North Carolina State University, Ellen O'Brien, Jun Fang, Goujing Hou, Han Bao, Jinyong Feng, Yuqiao Fan, Matt Zimmer, Joe Cambareri, Nadish Saini, Yuwei Zhu, Kaiyue Zeng, Hao-Ping Chang, Yangmo Zhu, Xu Han, Alp Tezbasaran, Anil Gurgen, Konor Frick and many others. It has been a pleasure for me to work with you in the past four and half years.

Finally, I would like to give my special thanks to my parents and my dear Linyu for your support and company.

The support by the Department of Energy's Nuclear Energy University Program's Integrated Research Project "Development and Application of a Data-Driven Methodology for Validation of Risk-Informed Safety Margin Characterization Models" and Consortium for Advanced Simulation of Light Water Reactors (http://www.casl.gov), an Energy Innovation Hub

(http://www.energy.gov/hubs) for Modeling and Simulation of Nuclear Reactors under U.S. Department of Energy [grant number DE-AC05-00OR22725] is gratefully acknowledged.

TABLE OF CONTENTS

LIST OF TABLES

LIST OF FIGURES

LIST OF SYMBOLS AND ABBREVIATIONS

Abbreviation

2D	Two Dimensional
3D	Three Dimensional
LWR	Light Water Reactor
PWR	Pressurized Water Reactor
DNB	Departure from Nucleate Boiling
M-CFD	Multiphase Computational Fluid Dynamics
DNS	Direct Numerical Simulation
LOCA	Loss-Of-Coolant Accident
HPC	High-Performance Computing
ITM	Interface Tracking Method
ONB	Onset of Nucleate Boiling
CHF	Critical Heat Flux
DFFB	Dispersed Flow Film Boiling
OSV	Onset of Significant Voids
LS	Level-Set Method
CLS	Conservative Level-Set
MAC	Marker And Cell method

FT	Front Tracking method
VOF	Volume Of Fluid
RANS	Reynolds-Averaged Navier-Stokes (equations)
LES	Large-Eddy Simulation
DES	Detached Eddy Simulation
INS	Incompressible Navier-Stokes (equations)
BTA	Bubble Tracking Algorithm
MPI	Message Passing Interface
GCI	Grid Convergence Index

Notation

P_b	Pressure inside the bubble (Pa)
P_l	Pressure in the surrounding liquid (Pa)
R_c	Radius of the cavity mouth (m)
D_s	Diameter of the largest cavities present on the surface (m)
T_∞	Liquid bulk temperature (℃)
Na	Nucleation site density ($number/m^2$)
T_w	Wall temperature (℃)
T_{in}	Inlet temperature (℃)

t_{gr}	Bubble growth time (s)
t_{wt}	Bubble waiting time (s)
H_ε	Smoothed Heaviside function
d	Corrected distance field in the level set method (m)
u_i	Instantaneous velocity component (m/s)
u	Instantaneous velocity vector (m/s)
w	Pseudo velocity vector (m/s)
p	Static pressure (Pa)
t	Simulation time (s)
f_i	Body force component (N)
T	Absolution temperature of the fluid (K)
c_p	Specific heat at constant pressure $(kJ/(kg \cdot ℃))$
c_v	Specific heat at constant volume $(kJ/(kg \cdot ℃))$
S_{ij}	Strain rate tensor
k	Thermal conductivity $(W/(m \cdot K))$
T_{sat}	Saturation temperature (℃)
q''	Heat flux (W/m^2)
V_i	Volume of local element (m^3)
V_{shell}	Volume of temperature gradient data collection shell (m^3)

h_{fg}	Latent heat of vaporization (kJ/kg)
R	Bubble radius (m)
n_w	The unit normal vector
Ca	Capillary number
V_{cls}	Contact line speed (m/s)
F_c	Contact angle control force (N)
d_{wall}	Distance from the wall (m)
H	Height of the contact angle force application region (m)
T	Thickness of the contact angle force application region (m)
M_{adv}	The offset of the arc-tangent function along the X axis
Y_{adv}	The offset of the arc-tangent function along the Y axis
y	The vertical distance from the bubble apex to the free surface (m)
x	The distance from the inlet to the nucleation point (m)
ΔT_{sub}	Liquid subcooling (℃)
ΔT_{sup}	Liquid superheat (℃)
ΔT_w	Wall superheat (℃)
U	Bulk liquid velocity (m/s)
Pr	Prandtl number
g	The gravity of Earth (m/s^2)

Ja^*	The normalized Jakob number
f	Bubble release frequency $(1/s)$

Greek letters

ρ_l	Liquid density (kg/m^3)
ρ_g	Gas density (kg/m^3)
ε_l	Interface half-thickness in the level set equation (m)
ε_d	Interface half-thickness in the re-distancing equation (m)
ε_{BT}	Interface half-thickness for bubble tracking algorithm (m)
μ_l	Liquid dynamic viscosity $(N \cdot s/m^2)$
μ_g	Gas dynamic viscosity $(N \cdot s/m^2)$
ν	Liquid kinematic viscosity (m^2/s)
φ	Level set scalar variable (m)
τ_{ij}	Reynolds stress tensor (N/m^2)
θ	Dynamic Contact angle (°)
ϕ	Distance from the interface (m)
Φ	Static contact angle (°)
θ_{adv}	Advancing contact angle (°)
θ_{rec}	Receding contact angle (°)

σ	Surface tension (N/m)
τ	Pseudo time in re-distancing equations (s)
β	The bubble growth rate constant
α_l	Liquid thermal diffusivity (m^2/s)
δ_T	Thermal boundary layer thickness (m)
δ	Hydrodynamics boundary layer thickness (m)
δ_m	The average thickness of the microlayer (m)
ε	Relative error

CHAPTER 1. INTRODUCTION

1.1. Overview and Motivation

Boiling phenomenon accommodates large heat fluxes with relatively small driving temperature difference, which makes it ideal for applications that demands substantial heat transfer rates like *Light Water Reactor* (LWR) nuclear power plants, chemical thermal processing, heat treatment and manufacturing, microelectronic cooling, and numerous microscale devices (microelectromechanical systems, micro heat pipes, lab-on-chips, etc.). The distribution of steam in a boiling mixture affects the heat transfer rate and may cause unfavorable conditions. For example, the distribution of vapor in the LWR sub-channels can cause burn-out phenomenon at certain wall superheat known as *Departure from Nucleate Boiling* (DNB). DNB, in turn, may cause fuel cladding damage, which may lead to reactor unplanned shutdowns and even accidents. Due to its complex nature, better understanding and modeling of boiling process remains a major challenge in multiphase flow research. In the last eight decades, boiling phenomenon has been an enduring appeal to researchers. The modeling of two-phase boiling phenomena has evolved a wide range of approaches, from one-dimensional models, to quasi-multidimensional subchannel models, to three dimensional *Multiphase Computational Fluid Dynamic* (M-CFD) models, and recently to *Direct Numerical Simulations* (DNS) of multiphase flows where individual bubbles are fully resolved.

The one-dimensional models (e.g., homogeneous equilibrium models, phasic slip models, drift-flux models and two-fluid models) are widely used in system thermal hydraulics codes such as RELAP5[1], TRACE [2] and GOTHIC [3]. This type of simulations is used by the nuclear community to analyze various reactor transients and accident scenarios *Loss-Of-Coolant Accident* (LOCA). The quasi-multidimensional subchannel (the coolant flow region between nuclear fuel

rods) models are utilized by subchannel analysis codes like COBRA-TF [4] to evaluate nuclear reactor safety margins. However, simulations based on one-dimensional models and quasi-multidimensional subchannel models do not resolve the anisotropy in the coolant channel and completely rely on single- and/or two-phase closure correlations. Many of the closure correlations in these models are only valid for specific geometries and a limited range of fluid dynamics and heat transfer conditions. If the application regions from different correlations do not satisfactorily overlap with each other in the simulation, their predictive capability may degrade when applied to new scenarios.

The advances in *High-Performance Computing* (HPC) in recent years make it possible to apply M-CFD to a wide variety of bubble hydrodynamics and thermodynamics studies [5, 6]. The M-CFD method can resolve thermal and velocity fields adjacent to the wall boundaries and the void fraction within three-dimensional domain representing the flow geometry. Therefore, this type of simulations could provide detailed information about the location of vapor generation onset, axial temperature profile, and axial and radial void distribution in two-phase flow [5]. However, simulations based on the M-CFD models require certain interfacial exchange terms (including mass, momentum and energy exchanges) to obtain closure like the lift force [7], the turbulent dispersion force [8], the wall heat flux partitioning [9], etc. In addition, the development and validation of 3D M-CFD model and physics-informed data-driven modeling require data of high-quality and high-resolution. Considering the difficulties in acquiring the corresponding experimental data in prototypic conditions, two-phase simulations based on DNS approach becomes feasible for many engineering applications.

In recent years, the DNS approach has already shown to be a reliable data source for model development and validation of single-phase flow [10, 11]. After an *Interface Tracking Method*

(ITM) is coupled with a DNS solver, the instantaneous velocity and temperature field at, and around, the interface, which may not be straightforward to obtain by any of the methods discussed above, can be calculated in two-phase flow simulations. ITM approach provides not only detailed physics-based description associated with thermal and hydrodynamic processes but also the shape of the evolving interface. A number of simulations utilized ITM approach have been conducted for bubble dynamics and heat transfer problems [12-18]. However, the ITM boiling models have been proposed so far are all developed for 3D structured mesh or 2D unstructured mesh. Both types of ITM boiling models face extreme difficulties when applying to large scale boiling simulation with complex geometries. The 2D ITM boiling models doesn't have correct representation of 3D bubbles. The 3D ITM boiling model for structured mesh has been successfully applied to various boiling scenarios, but it requires huge amount of computation resource to accurately simulate the scale changes from nucleate bubble to high void fraction regime. In addition, the structured grid requirement makes it challenging to apply in complex engineering geometries. So, most ITM boiling models in the literature mainly focus on the boiling simulation in limited domains (e.g. single coolant channel, small water pool) and the fundamental study of the boiling heat transfer mechanism. Meanwhile, other simulation approaches studying the system thermal hydraulic in large scale cannot provide detailed information at and around the bubble interface and rely on highly empirical closure models. The ITM boiling model in this research aims to fill the numerical data gap between the study of local phenomenon and the large scale engineering application by performing high resolution high quality large scale boiling simulation in practical geometries. In order to perform large scale boiling simulation, the ITM boiling model is developed in consideration of conducting simulations with local mesh refinement, unstructured mesh and highly scalable algorithm for parallel computing.

This work focuses on the development, verification and validation of this 3D ITM boiling model and, also demonstrate the potential of this model in conducting large scale boiling simulation for engineering applications. The boiling simulations in the presented research are conducted in full 3D representation with the unstructured grid. This approach allows us to investigate the boiling phenomenon in various conditions with lower cost (by utilizing local mesh refinement for bubble growth region). The bubble dynamics information including bubble trajectory, growth rate, etc. is collected individually for each bubble using the modified and improved bubble tracking algorithm (BTA) [19]. Together with the massively parallel-computing capability of PHASTA (which is the advanced flow solver used for the presented research, and the abbreviation stands for **P**arallel, **H**ierarchic, higher-order accurate, **A**daptive, **S**tabilized, **T**ransient **A**nalysis), this work enables the high-resolution boiling simulations in subchannel scale (Appendix.B), including the challenging prototypic pressure/temperature conditions existing during normal operations in *Pressurized Water Reactor's* (PWR) core.

1.2. Boiling Regimes

Steam-water two-phase mixture can form a lot of different topological interface flow configurations. The two-phase boiling regimes summarized the most frequently observed flow pattern in boiling phenomenon. The ranges of occurrence of the major two-phase flow regimes are essential for the modeling and analysis of two-phase boiling systems. The frequently-used pool boiling and the flow boiling regimes are discussed in this section.

1.2.1. The Pool Boiling Regimes

The distribution of vapor in a boiling mixture forms various bubble topologies at different applied wall heat flux, which affects the heat transfer rate and flow dynamics of the system. The flow regime maps are introduced to quantify visually observed flow patterns in terms of measured quantities, so that the existence of a certain flow regime, or the transition from one flow regime to another can be predicted. For each flow regime, the dominating heat transfer mechanism and flow characteristics are different. In most system thermal hydraulics codes, the flow regime is an important criterion for heat transfer model selection. The different heat transfer mechanisms are often represented by a boiling curve. The typical version of the pool boiling curve [20] is shown in Figure 1.1 and was originally introduced by Nukiyama [21] to describe the relation between the wall heat flux and the wall superheat (the difference between wall temperature and the saturation temperature at system pressure). In the first region, heat transfer is dominated by natural convection and the energy accumulated at the vicinity of the heated surface is not enough to initiate nucleation. As the heat flux and the wall superheat increases, at one point the nucleation site starts to be active and bubbles appear on the heated surface, which is known as the *Onset of Nucleation Boiling Point* (ONB). In the partial nucleate boiling region, isolated bubbles nucleate, grow, depart, slide along the wall and eventually lift off. The heat transfer is dominated by a complex mixture of nature convection and nucleate boiling. As the wall heat flux increases, more and more

nucleation sites are activated, and the isolated bubbles grow larger and merge with other bubbles to form vapor columns and mushroom-shaped bubbles, which is known as fully developed nucleate boiling. In this region, the fraction of the wall surface area subject to nucleate boiling increases until bubble formation occupies the entire heated surface and the contribution of natural convection heat transfer is negligible. As bubble density increases, bubbles start to coalesce and form heat-insulating vapor films, which also impedes liquid return back to the surface. The heat transfer rate under this condition reduces dramatically. This point C is called *Critical Heat Flux* (CHF). Further increase in the wall heat flux leads to the post CHF boiling regimes: transition boiling and film boiling. In transition boiling region, the vapor films grow, and collapse

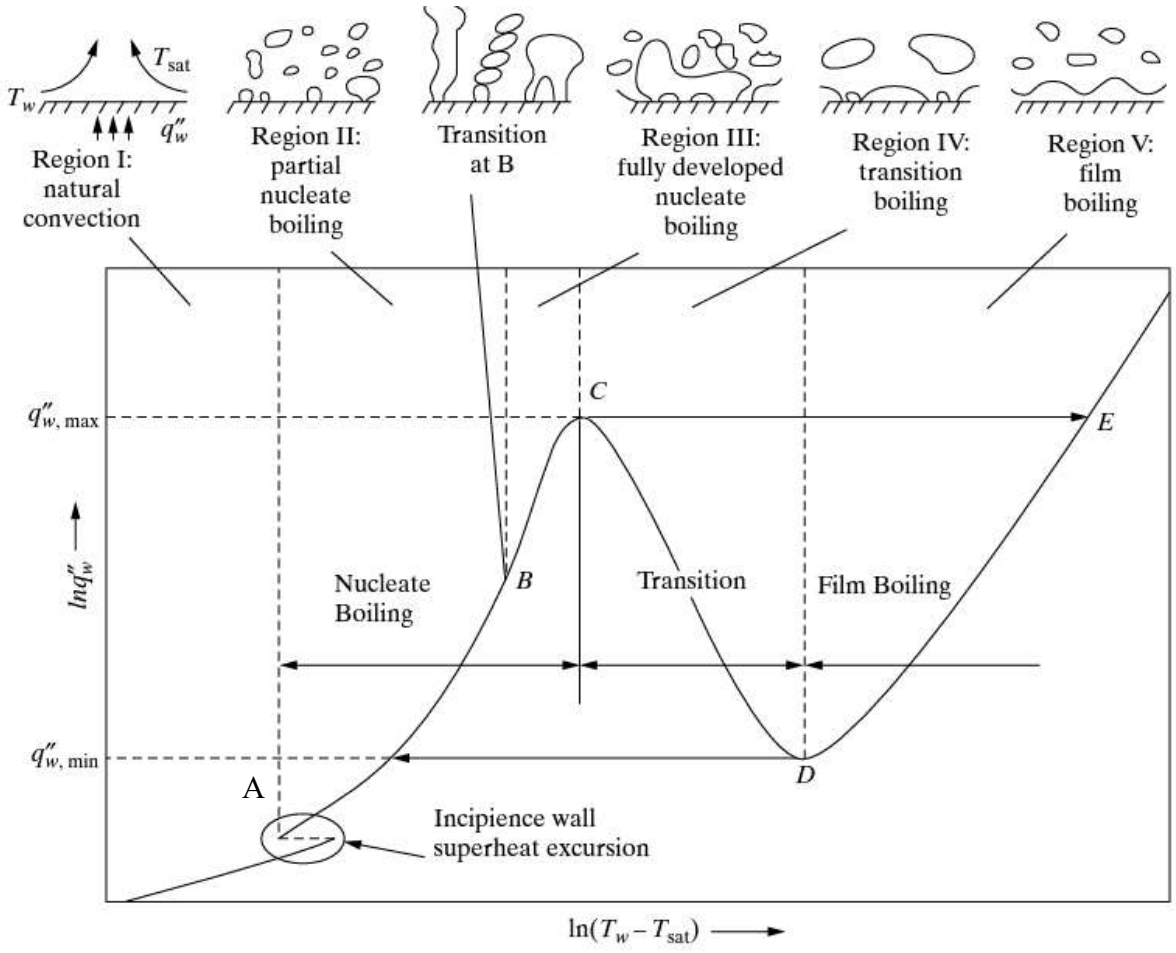

Figure 1.1. Typical pool boiling curve and associated flow regimes[20].

dynamically. As the wall superheat increases, the dry fraction of the heated surface increases. As

more and more wall surface covered by vapor film, the film boiling is achieved. There is no direct macroscopic contact between liquid and solid surface. The heat transfer coefficient decreases significantly compared to that of nucleate boiling due to conductivity, density and heat capacity properties of vapor.

Of these three boiling modes, **film** boiling is the easiest to analyze. The nucleate and transition boiling are much more complex and usually require empirical or mechanistic correlations as model closures.

1.2.2. The Flow Boiling Regimes

Flow boiling is considerably more complicated than pool boiling due to the coupling between flow hydrodynamics and boiling heat transfer processes. As the void fraction increases during flow boiling, the two-phase and boiling heat transfer regimes are developing along the heated channels. The configuration of the boiling channel also affects the heat transfer rate and the flow regime transition. The vertical upflow channel is often used in many thermal cooling systems (e.g. LWR coolant channel) since the buoyancy effect in such configuration can help the flow of the mixture which in turn improves the heat transfer rate. It is noted that the horizontal boiling channels and vertical downflow channels are also of interest in certain operating conditions.

The schematic flow boiling regimes are displayed in Figure 1.2. The two-phase flow patterns develop in a vertical upflow channel with uniform and moderate heat flux. When the inlet flow has a large subcooling, the entire flow channel remains to be subcooled. If the wall heat flux increases, the first bubble will form at some location downstream where the wall superheat is high enough to initiate nucleation. The flow regime at the exit can be bubbly flow, slug flow or annular flow, which depends on the wall heat flux and the inlet subcooling. If the inlet flow is saturated,

the boiling will start at the inlet region and has a large chance moving to *Dispersed Flow Film Boiling* (DFFB) regime and the single-phase pure vapor flow regime.

The subcooled flow boiling covers the region beginning from the location where the wall temperature exceeds the local liquid saturation temperature to the location where the thermodynamic quality reaches zero, corresponding to the saturated liquid state. There are three regions of subcooled flow boiling identified by earlier researchers as: (i) single-phase forced convection region, (ii) partial nucleate boiling, and (iii) fully developed nucleate boiling. A schematic representation of the subcooled flow boiling is shown in Figure 1.3. The inlet flow is highly subcooled. There is no volume fraction of vapor and the heat transfer is dominated by single-phase forced convection. At some location downstream, bubbles start to nucleate because of the local wall superheat while the bulk liquid is still subcooled. This location is identified as the

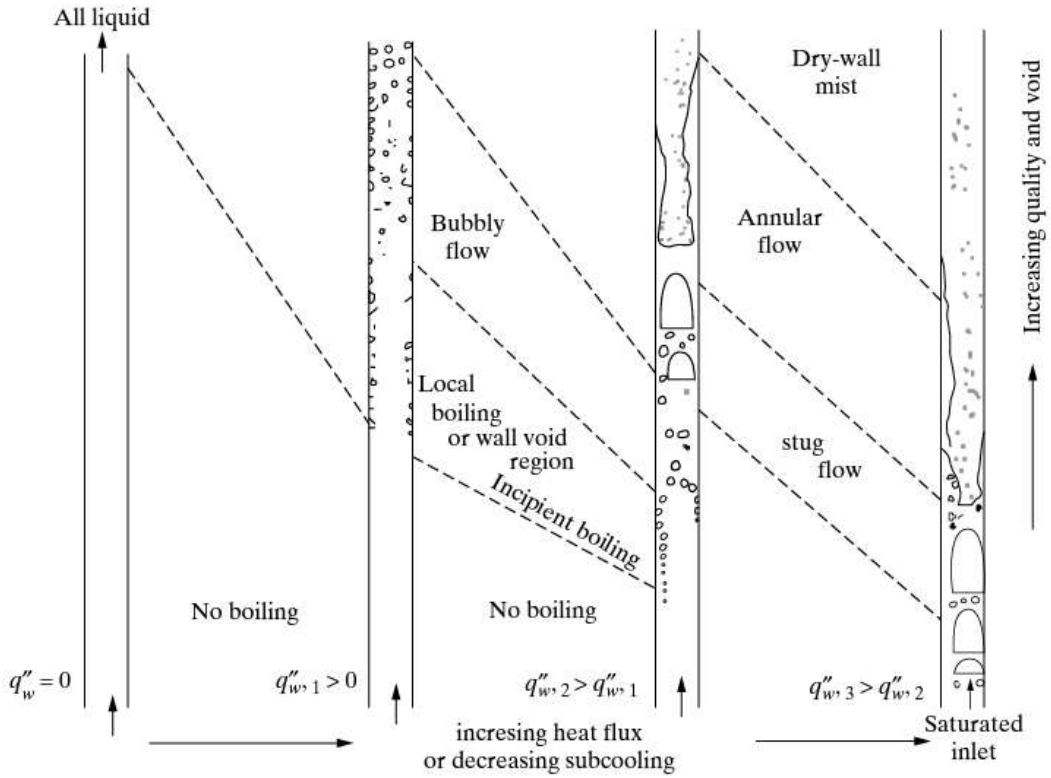

Figure 1.2. Development of two-phase flow patterns in flow boiling [20].

Onset of Nucleate Boiling (ONB). Downstream of ONB, the bubbles are still small enough to remain attached to the heater surface. As the bulk liquid temperature increases, the bubbles grow larger, begin to depart from the nucleation sites, slide along the heater surface, and eventually lift off from the wall. The location where the bubbles begin to lift off from the heated wall is called the location of *Onset of Significant Voids* (OSV). In the region between ONB and OSV, the void fraction is small but increases rapidly downstream of OSV. The heat transfer mechanism is a complex mixture of single-phase forced convection, evaporation, condensation and quenching. As the void fraction increases, a bubbly layer may form adjacent to the wall and eventually develop a thin film layer between the liquid and the heated wall surface. This leads to the *Departure from Nucleate Boiling* (DNB) event. The heat transfer coefficient deteriorates dramatically downstream from this point. In nuclear reactor, DNB may cause fuel cladding damage and result in reactor unplanned shutdowns and even accidents.

1.3. Heterogeneous Bubble Nucleation and Active Nucleation Sites

The defects of the heated surfaces like microscopic/nanoscopic cavities and crevices can trap minute pockets of air when the surface is submerged in the liquid. These pre-existing interface areas act as an embryo for bubble growth under low heat flux conditions. This phenomenon is referred to as heterogeneous bubble nucleation. Compared to homogenous boiling which requires large liquid superheats to initiate the nucleation process, heterogeneous boiling only needs a few degrees of wall superheat. Nucleation on the defects of the heated wall surface can take place within a thin, superheated liquid layer adjacent to the wall while the liquid bulk is subcooled. Hsu

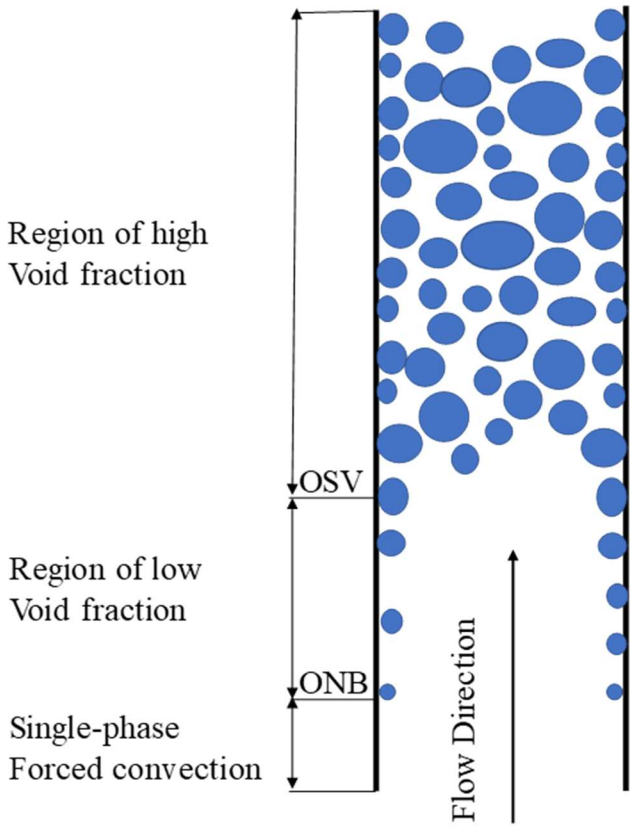

Figure 1.3. Two-phase subcooled flow boiling regime with a moderate and uniform wall heat flux.

[22] was the first to propose the criteria for boiling inception. According to their experimental results[23], the liquid layer surrounding the embryo must be equal or larger than the saturation

temperature at the corresponding pressure for bubble growth. The pressure difference between bubble interior and surrounding liquid can be expressed by Young-Laplace equation ($\Delta P = 2\sigma/r_b$). The Clausius-Clapeyron relationship, a bubble surrounded by a liquid with uniform temperature, was written in terms of temperature as,

$$T_l - T_{sat} \approx \frac{T_{sat}}{\rho_v h_{fg}}(P_b - P_l) = \frac{2T_{sat}\sigma}{\rho_v h_{fg} R_c} \quad (1\text{-}1)$$

where T_l is the temperature of the surrounding liquid, P_b is the pressure inside the bubble, P_l is the pressure in the surrounding liquid and R_c is the radius of the cavity mouth.

Assuming a linear temperature profile in the thermal boundary layer with thickness δ as,

$$\frac{T_l(y) - T_\infty}{T_w - T_\infty} = 1 - y/\delta \quad (1\text{-}2)$$

According to Hsu's criteria, the possible range of nucleating cavity size for a certain wall superheat is given,

$$\{R_{c,min}, R_{c,max}\} = \frac{\delta C_2}{2C_1}\frac{T_w - T_{sat}}{T_w - T_\infty} \times \left[1 \mp \sqrt{1 - \frac{8C_1\sigma T_{sat}(T_w - T_\infty)}{\rho_v h_{fg}\delta(T_w - T_{sat})^2}}\right] \quad (1\text{-}3)$$

where $C_1 = 1 + cos\theta_m$ and $C_2 = sin\theta_m$ when the cavity mouth has a slope of θ_m, T_w is the wall surface temperature and T_∞ is the liquid bulk temperature.

Several improvements have been introduced into Hsu's criterion [22]. Howell and Siegel [24] argued that Hsu's criterion is conservative. The temperature measured in their experiments turned out to be lower than the temperature requirements of Hsu's criterion. They proposed to use net heat exchange rate between the bubble and surrounding liquid for bubble growth. Wang and Dhir [25] provided a minimum superheat required to initiate nucleation based on the minimization of the Helmholtz free energy of a system containing a gas-liquid interphase for highly wetting liquids. They derived the inception criterion for a spherical cavity as following [26],

$$T_w - T_{sat} = \frac{2\sigma T_{sat}}{\rho_g h_{fg} R_c} K_{max} \quad (1\text{-}4)$$

where

$$K_{max} = \begin{cases} 1 & for\ \theta \le \frac{\pi}{2} \\ \sin\theta & for\ \theta > \frac{\pi}{2} \end{cases} \quad (1\text{-}5)$$

where θ is the interface contact angle measured in the liquid side.

Basu et al. [27] expanded the minimum superheat criterion by accounting for the wettability of commercial surface whose cavity shape and size distribution are hard to determine. They concluded that the minimum wall superheat required diminishes as the wettability increases (the contact angle decreases). Most recently, the BETA experimental results by Theofanous et al.[28] indicated that the micron-scale and macroscopic roughness may not be necessary for heterogeneous nucleation and parameters such as cavity size, or contact angle are of derivative significance in heterogeneous boiling. The discussion on the heterogeneous nucleation is on-going in the research community and the principal cause/mechanism still remains to be found.

The nucleation sites density describes the number of bubbles that are found (at any time) per unit area of the heater surface, which is another important integral characteristic of heterogeneous nucleation boiling. Mikic and Rohsenow [29] assumed that the number of sites per unit area with radii larger than $D_c/2$ can be approximated with the power law:

$$N_a = \left(\frac{D_s}{D_c}\right)^{m_1} \quad (1\text{-}6)$$

where D_s is the diameter of the largest cavities present on the surface and m_1 is an empirical constant. The nucleating cavity diameter R_c (The same R_c in Eq.(1-1)) can be related to fluid properties and wall superheat ΔT_w as:

$$R_c = \frac{4\sigma T_{sat}}{\rho_v h_{fg} \Delta T_w} \quad (1\text{-}7)$$

where σ is the liquid surface tension, ρ_v is the vapor density and h_{fg} is the latent heat of evaporation.

Kocamustafaogullari and Ishii [30] proposed another nucleation site density model which was correlated to the dimensionless minimum cavity size and the fluid density ratio. The boiling heat transfer data used in their model covered a wide range of pressure variation. The bubble dynamics and heat transfer in the region between nucleation sites were also considered in the nucleate boiling heat transfer calculation. Therefore, their model has a fairly good representation of the existing experimental water data.

$$N_a^* = [D_c^{*-4.4} F(\rho *)]^{1/4.4} \quad (1\text{-}8)$$

where

$$N_a^* = N_a D_d^2; D_c = D_c / D_d \,; \;\; \rho^* = (\rho_l - \rho_v)/\rho_v \quad (1\text{-}9)$$

and

$$F(\rho^*) = 2.157 \times 10^{-7} \rho^{*-3.2} (1 + 0.0049\rho^*)^{4.13} \quad (1\text{-}10)$$

In Eq.(1-9), the bubble diameter at departure D_d is obtained by Fritz's correlation [31], and the nucleating cavity diameter D_c is obtained using Eq. (1-7) at low to moderate pressures.

Basu et al. [32] proposed a model that correlated nucleation site density to contact angle values. According to their results, the correlations for the nucleation site density were independent of flow rate and liquid subcooling but dependent on the contact angle and wall superheat.

$$\begin{aligned} N_a &= 3.4[1 - \cos\Phi]\Delta T_w^2 \quad \Delta T_{w,ONB} \le \Delta T_w < 15℃ \\ N_a &= 3.4 \times 10^{-5}[1 - \cos\Phi]\Delta T_w^{5.3} \quad \Delta T_w > 15℃ \end{aligned} \quad (1\text{-}11)$$

1.4. Bubble Growth Model

Researchers have attempted to model bubble growth in nucleate boiling since the 1950's. In the early growth models, the bubble is assumed to be surrounded by superheated liquid and the bubble growth is driven by the evaporation at the interface. Plesset and Zwick [33] and Forster and Zuber [34] derived analytical bubble growth models for bubbles surrounded by uniformly superheated liquid. Researcher like Birkhoff et al.[35] and Scriven [36] improved this analytical model and Mikic et al.[37] extended the analytical growth model to non-spherical bubble.

However, this type of bubble growth model does not account for the wall effect on the bubble growth. When a bubble grows from the nucleation site, it is believed that there is a thin liquid layer (the microlayer) underneath the bubble. As the microlayer evaporates, an initial sharp drop in temperature occurs and a recovery in the temperature happens after formation of a dry spot. After this a small drop in temperature and subsequent recovery appears when liquid rewets the surface during the bubble departure. The existence of micro-layer underneath the growing bubble has been confirmed via local temperature distribution measurements. Moore and Mesler [38] observed the significant local temperature fluctuations on the wall under the bubbles during the nucleate boiling and suggested that microlayer evaporation could be the reason of the fluctuations. Hendricks and Sharp [39] correlated the wall temperature fluctuations with high-speed videos of individual bubbles and showed that the rapid temperature decrease in the wall temperature was associated with bubble growth. Cooper and Lloyd [40] measured the temperature field evolutions during boiling of toluene and isopropyl alcohol on the glass and ceramic substrates whose backsides were radiantly heated. They proposed the average thickness of the microlayer can be,

$$\delta_m = C\left(\nu t_{gr}\right)^{1/2} \qquad (1\text{-}12)$$

where $C \approx 0.3 - 1.3$, t_{gr} is the bubble growth time and ν is the kinematic viscosity of liquid.

1.5. Bubble Departure Diameter

There is a large volume of published studies describing the diameter to which a bubble grows before departure. Fritz [31] proposed a correlation based on the force balance between buoyancy force, which acted to lift the bubble from the surface, and the surface tension force, which tended to hold the bubble to the wall in pool boiling condition. The resulting bubble departure diameter is given as

$$D_d = 0.0208\Phi\sqrt{\frac{\sigma}{g(\rho_l - \rho_v)}} \qquad (1\text{-}13)$$

where Φ is the static contact angle measured in degrees. Han and Griffith [41] found that the Fritz formula worked as long as the true (no-equilibrium) bubble contact angles were used. In general, these values should be known for various fluids at different pressure. However, these data of bubble contact angles reported in literature are very limited and inconsistent. For example, Griffith and Wallis [42] found that the average value of Φ(contact angle) did not depend on water saturation pressure while Labuntsov et al.[43] showed that there was a weak effect of the saturation pressure on Φ for water boiling on a silver surface at $p_s = 0.1 - 15MPa$. Pioro et al.[44] suggested that the task of obtaining accurate values of the true contact angle during boiling was unrealistic. Therefore, the Fritz formula can only be considered as a theoretical approach. In general, part of the formula $\left(\sqrt{\frac{\sigma}{g(\rho_l-\rho_v)}}\right)$ is used in many practical non-dimensional correlations for nucleate pool boiling heat transfer calculation. Some of the wide-used correlations are shown below.

Cole and Rohsenow [45] correlated bubble departure diameter at low pressures as

$$D_d = 1.5\times10^{-4}\sqrt{\frac{\sigma}{g(\rho_l - \rho_v)}}Ja^{*5/4} \text{ for water} \qquad (1\text{-}14)$$

and

$$D_d = 4.65 \times 10^{-4} \sqrt{\frac{\sigma}{g(\rho_l - \rho_v)}} Ja^{*5/4} \text{ for other liquids} \quad (1\text{-}15)$$

where $Ja^* = \rho_l c_{pl} T_{sat} / \rho_v h_{fg}$ is the normalized Jakob number. Kocamustafaogullari [46] proposed a correlation for bubble departure diameter including high-pressure conditions as below:

$$D_d = 2.64 \times 10^{-5} \sqrt{\frac{\sigma}{g(\rho_l - \rho_v)}} \left(\frac{\rho_l - \rho_v}{\rho_v}\right)^{0.9} \quad (1\text{-}16)$$

It is widely agreed that $\sqrt{\frac{\sigma}{g(\rho_l - \rho_v)}}$ is proportional to the bubble departure diameter, but a generalized correlation (a correlation could be used for both low pressure and high pressure) or comprehensive model for bubble departure diameter has not been proposed yet. The key impediments have been the lack of knowledge of instantaneous local velocity and temperature field. The velocity and temperature field vary both temporally and spatially because of bubble deformation and bubble movement. This, in turn, affects the bubble growth rate and forces that act on the bubble through temperature and velocity fields. Additionally, surface wettability, contribution of microlayer, and merger of vapor bubbles have an influence of bubble departure diameter.

1.6. Bubble Release Frequency

The time period before bubble released is categorized into growth time and waiting time for modeling purpose [47]. The growth period is defined as the time from the nucleation occurs to the bubble lifts off, which are mainly affected by the bubble evaporation rate and bubble departure diameter. The waiting time describes the time needed for the new bubble appears at the same nucleation site after the previous one departs. Once the bubble lifts off from the wall, the cooler liquid in the vicinity rushes in to fill the space previously occupied by the vapor. Most waiting time models assumed that the nucleation site would be activated once the liquid superheat condition was established. Hsu and Graham modeled the liquid thermal field as one-dimensional transient conduction in a slab and proposed a waiting time model t_{wt} as follows [23, 48],

$$t_{wt} = \frac{9}{4\pi}\left[\frac{(T_w - T_\infty)R_c}{T_w - T_{sat}\left(1 - \frac{2\sigma}{R_c\rho_g h_{fg}}\right)}\right]^2 \quad (1\text{-}17)$$

where $\alpha_L = k/\rho c_p$ is the thermal diffusivity of liquid and R_c is the cavity size. However, the local cooling of the solid is ignored in this model. The thermal response of the solid surface was taken account later by Hatton and Hall [49].

Bubble release frequency reflects the number of bubbles released from the same nucleation site per unit time. It is defined as the inverse of the summation of the growth and waiting time. One of the commonly used correlations was proposed by Zuber [50] as,

$$fD_d = 0.59\left[\frac{\sigma g(\rho_l - \rho_v)}{\rho_l^2}\right]^{1/4} \quad (1\text{-}18)$$

Jakob and Fritz [51] proposed that the product of bubble release frequency (f) and bubble departure diameter (fD_d) should be a constant,

$$fD_d = 0.078 \quad (1\text{-}19)$$

Cole's correlation of bubble release frequency is also well known for pool nucleate boiling,

$$f = \sqrt{\frac{4g(\rho_l - \rho_g)}{3D_d\rho_l}} \qquad (1\text{-}20)$$

Here D_d in the correlations above denotes the bubble departure diameter (discussed in Section 1.5) There are other correlations proposed for bubble release frequency. Mikic and Rohsenow [29] developed a model for heat-transfer-controlled growth of a bubble in a non-uniform temperature field near a heated surface. The bubble release frequency is derived using the waiting and growth times,

$$f^{1/2}D_d = \left(\frac{4}{\pi}\right)Ja\sqrt{3\pi\alpha_l}\left[\left(\frac{t_{gr}}{t_w + t_{gr}}\right)^{1/2} + \left(1 + \frac{t_{gr}}{t_w + t_{gr}}\right)^{1/2} - 1\right] \qquad (1\text{-}21)$$

where D_d is the departure diameter, α_l is the thermal diffusivity $(= k/\rho c_p)$, Ja is the Jakob number defined as,

$$Ja = \frac{\rho_l c_{pl}[T_\infty - T_{sat}(p_\infty)]}{\rho_v h_{fg}} \qquad (1\text{-}22)$$

However, predictions from these correlations are valid only for the limited data range over which supporting data have been obtained. It is hard to model bubble release frequency because all the parameters in nucleate boiling like bubble growth rate, temperature and velocity field in the vicinity of the bubble, heater response, etc. are interrelated. Innovative approaches in experiments and simulations are needed to help the mechanistic model development for this complex phenomenon.

1.7. Bubble Contact Angle

During the nucleate boiling process, a vapor bubble nucleates from a micro-cavity in the wall surface, grows due to the wall at superheat temperature, and departs when it reaches a critical size determined by a local force balance. Previous research has shown that contact angle plays an essential role in determining boiling parameters like nucleation site density [52], bubble departure diameter [31], and bubble release frequency [50]. Therefore, it is important to maintain correct contact angle in boiling simulations. The contact angle used in boiling models is defined as the angle between the vapor-liquid interface at the interface contact line and the wall surface in liquid side as shown in Figure 1.4. The advancing contact angle (θ_{adv}) is the maximum value of the contact angle at the interface contact line while the receding contact angle (θ_{rec}) is the minimum value. If the wall surface is ideal (smooth, flat, and homogenous) and the interface is not moving, the contact angle only depends on the vapor and liquid properties and the solid surface material. In this situation the contact angle is defined as the static contact angle. As the bubble grows or slides along the wall, the bubble movement will have an impact on the value of contact angle besides physical properties and surface material. This type of scenarios is described using dynamic

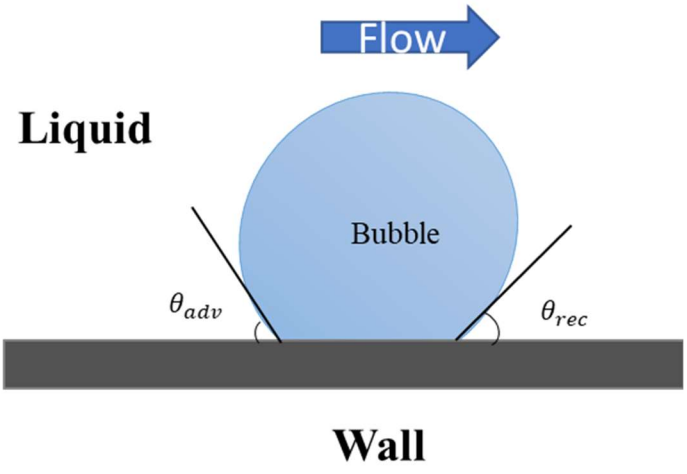

Figure 1.4. The schematic of apparent contact angle.

contact angle, and typically requires specification of advancing and receding contact angles. One must note, that the static contact angle usually does not have a well-defined value for realistic surfaces, because most surfaces are not ideal. Typically, a measured dynamic contact angle value would fall into the interval between the advancing contact angle and receding contact angle.

The contact angle hysteresis has been studied for various solid-liquid combinations and surface conditions. Young [53] was one of the first researchers to recognize the relationship between surface tension and contact angle. By analyzing the contact angle of a gas bubble on a solid surface in the water, he suggested that the contact angle was determined through the balance of the surface tension forces between the three material phases: gas, liquid and solid. However, it is noted that the validity of Young's model requires the solid surface to be ideal, which is almost impossible to achieve in practice. Wenzel [54] investigated the effect of the roughness of the surface on the static contact angle. His research demonstrated that surface roughness enhanced the hydrophobic effect — if the fluid was hydrophobic: it would behave more hydrophobic on the rough surface than it on the smooth surface. Similar effect was observed for hydrophilic fluids: this property was also enhanced on rough surfaces. Cassie [55] proposed a model describing the changes of the contact angle on a heterogeneous surface. Lam et al. [56] measured the dynamic one-cycle and cyclic contact angle for various liquid/solid combinations. They recognized four different patterns of receding contact angle behavior in their experiments.

Besides the surface conditions of liquid-solid combination and physical properties of each phase, the contact angle is also influenced by the vapor-liquid interface velocity. Ramanujapu and Dhir [57] experimentally investigated nucleate pool boiling phenomenon and focused their efforts on the dynamic contact angle measurements at the base of vapor bubbles. Their results showed that the dynamic contact angle mainly depended on the direction of the interface velocity and had

a weak dependency on the interface velocity in the performed range of experiments. Sobolev et al. [58] conducted measurements of the dynamic contact angle of water in the thin quartz capillaries with various radii in the range of 40 to 200 nm. They found that the dynamic contact angle is linearly dependent on the velocity when velocities were less than $5\ \mu m/s$ while it is independent at higher velocities. Kandlikar et al. [59] experimentally investigated an evaporating meniscus on a smooth moving heated surface. They concluded that the contact angle was almost independent of the wall superheat for the stationary meniscus and as the surface velocity increased the receding contact angle would vary at relatively low wall superheat. The advancing and receding motion of the meniscus increased the local heat transfer rate, which is observed in the experiment.

Several different models of dynamics contact angle have been proposed for numerical simulations. Fukai et al. [60] experimentally and theoretically investigated the deformation of a liquid droplet impacting against a flat surface. In their presented model of the wetting effect, the dependency of contact line velocity and the distinct value of advancing and receding contact angle were considered. The contact angle values were determined experimentally and used as input to the model. The numerical prediction of droplet shape evolution showed qualitative agreement with the measured data. Bussman et al. [61] proposed a 3D model to describe the impact of a droplet on asymmetric surface geometries using volume tracking algorithm. Contact angle model was applied as a boundary condition at the contact line. In their method, the advancing and receding contact angles obtained from the experiments were applied to the contact angle model if the simulated contact line velocity was greater than specified velocity criteria $(0.1\ m/s)$. At the locations where the contact line velocity was less than velocity criteria $(0.1\ m/s)$, the contact angle was linearly interpolated between the nearest known values. The minimum values of contact angle

in the range where the contact line velocity value is less than velocity criteria were also specified as a constant equilibrium contact angle.

Abarajith and Dhir [62] numerically investigated the effect of contact angle on the single bubble during nucleate pool boiling using *Level-Set method* (LS). The contact angle was maintained at a constant value during the bubble growth and departure process. As the contact angle increased, the bubble departure diameter and time to departure both increased. The simulations were carried out on the two-dimensional and axisymmetric domain in their study. Son and Hur [63] proposed a contact angle model on non-orthogonal grids for LS. The 2D and 3D simulations of free-surface motions were conducted, but only 2D simulations were performed for the motion of the droplet on an inclined wall. Mukherjee and Kandlikar [64] studied single bubbles with dynamic contact angle during nucleate pool boiling using LS. They proposed a dynamic contact angle model which linked the dynamic contact angle to the contact line velocity. A similar approach is adopted in the contact angle algorithm for the presented high-resolution boiling simulations research, where the contact angle is expressed as a function of contact line velocity. According to their results, the decrease in surface wettability played a key role in departing a bubble with a larger diameter. The simulations were performed using three-dimensional structured meshes. Sato and Niceno [65] came up with a contact line treatment for a Conservative Level-Set (CLS) method. The contact angle model was implemented as a special type of boundary condition. The 3D simulations including droplet on a wall without gravity and bubble detached from the wall were conducted on the structured mesh.

1.8. Interface Tracking Boiling Simulations

In recent years, there has been an increasing interest in applying DNS to boiling simulations. The DNS approach has already shown to be a reliable data source for model development and validation of single-phase flow [10]. After an *Interface Tracking Methods* (ITM) are introduced to a DNS-capable solver, the conservation equations of mass, momentum, and energy for liquid and vapor phases are solved simultaneously using one-fluid approach as the interface is continuously evolving at/near the heated surface. The instantaneous velocity and temperature field at, and around, the interface, which may not be straightforward to obtain by any of the methods discussed above, can be calculated in two-phase flow simulations. There are different types of ITM including *Marker and Cell* (MAC) method [66], *Front Tracking* (FT) Method, *Level-Set* (LS) method, *Volume-Of-Fluid* (VOF), and several others. MAC method uses massless particles to track interface movement and reconstruct the interface in the structured mesh. One of the earliest boiling simulation based on the MAC method was done by Madhaven et al. [67]. Similar to the MAC method, FT method also utilized massless particles to follow the interface movement, but the interface is tracked using Lagrangian method and the particles are always connected through a separate computational grid [68]. Tryggvason et al. [68] developed and improved this method, especially the curvature calculation. His research group conducted a series of boiling-related simulation using FT method [69-71]. The LS method introduces a distance field (level-set field) that contains the information about the distance to the interface which is set to be zero level set [72-74]. Dhir and his group [18, 75, 76] have conducted various boiling simulations using LS method. The detailed simulations will be discussed later in this section. The level-set method is also utilized in Bolotnov's research group [77-80] for bubble dynamics and heat transfer problems. VOF method represents the fraction of liquid or gas phase in the computational cell and

reconstructs the interface based on the volume fraction information [81]. Kunugi et al. applied this method to subcooled pool and flow boiling simulations [82, 83].

The Level-Set simulation on boiling phenomenon has started at the end of 1990's. Most of the boiling simulations at that time were done in a 2D domain with structured mesh. One of the early research efforts on 2D numerical boiling simulation was conducted by G. Son et al. [16] simulating a growing and departing bubble on a horizontal surface. The local wall heat flux and the effect of microlayer evaporation are considered in their simulation. The bubble merger process was studied by Son et al. [18] on a single nucleation site during pool nucleate boiling. The level set method was used to handle breaking and merging of the interface and modified to include the effects of phase change at the interface and contact angle at the wall. As the capabilities of HPC grow, the 3D boiling simulation with interface tracking methods became feasible. A. Mukherjee and V.K. Dhir [17] conducted 3D simulations of the lateral merger of vapor bubbles during nucleate pool boiling. Calculations were carried out for multiple bubble mergers in a line and in a plane using uniformed structured mesh. Their results showed that the merger of multiple bubbles significantly increased the overall wall heat transfer. Gihun Son and V.K. Dhir [15] investigated nucleate boiling on a horizontal surface at high heat flux including the effect of wall superheat, the number density of active nucleation sites and waiting period on the bubble dynamics and heat transfer. Sato and Niceno [14] performed a nucleate pool boiling simulation on the boiling regime from discrete bubble to vapor mushroom regime. Both the conjugate heat transfer phenomenon and the vaporization of the micro-layer were considered in their simulations. Compared with *pool* boiling, only a few simulations focus on *flow* boiling phenomenon. Li and Dhir [84] performed a flow boiling simulation with a single bubble in the rectangular shape domain in 2007, but the capability was still limited by utilization of the spatially uniform grid. In their simulation, only

one-half of the domain was simulated, and the three-dimensional domain was obtained by the planar symmetry of the geometry. Dahiri and Tryggvason [12] simulated the heat transfer in turbulent bubbly flow in vertical channels, but bubble evaporation and condensation were not considered in their simulation. Almost all these simulations are conducted in cuboid or tube-like domain with structured mesh. Despite the reduced cost of computational resources, 3D boiling simulation with interface tracking method, especially for engineering applications, remains relatively expensive. The need of increasing the affordability of simulations by improving numerical methods and models will grow for the next decades.

1.9. Research Objectives

The development and validation of 3D *Multiphase Computational Fluid Dynamics* (M-CFD) model and physics-informed data-driven modeling require data of high-quality and high-resolution. Considering the difficulties in acquiring the corresponding experimental data in prototypic conditions, two-phase simulations by ITM-based models can be used for generating high-resolution numerical data in a consistent, best-estimate, and relatively economical manner. The development, verification and validation of a boiling model in one of the ITM-based multiphase-flow solvers, named PHASTA, is presented in this dissertation: (a) The evaporation and condensation model is designed for multiphase simulations in full 3D representation with the unstructured grid. This model is capable to investigate the boiling phenomenon under various conditions with lower cost (by utilizing local mesh refinement for bubble growth region); (b) The contact angle control model is implemented to maintain correct contact angle while the bubble is attached to the wall; (c) The bubble dynamics information including bubble trajectory, growth rate, etc. is collected individually for each bubble using the modified and improved bubble tracking algorithm [19]. This unique capability can help improve multiphase computational fluid dynamics models and perform virtual experiments on the much larger scale (billions of mesh cells on tens of thousands of computing cores) like subchannel geometry under PWR temperature / pressure normal operating conditions.

To better present the model development approach, verification, validation and application examples, this dissertation is structured as follows: CHAPTER 2 describes the numerical method utilized in the simulations including the information of the ITM flow solver (PHASTA), the interface tracking method (level-set method), the evaporation and condensation model, the contact angle force model and the bubble tracking algorithm. These components provide the basis for the presented research. CHAPTER 3 focuses on the development and verification of the evaporation

and condensation model. The single bubble growth simulations have been performed in comparison with analytical solution [36] as well as mesh resolution sensitivity study and superheat rate parametric study. The multiple bubble growth simulation is also presented and verified. The energy conservation during unresolved phase of bubble condensation process is discussed as well. CHAPTER 4 introduces the contact angle control model implementation in PHASTA. The model verification of single bubble departure has been performed according to analytic force balance analysis. The mesh sensitivity study and the parametric study results on target contact angle and critical contact angle are presented in this Chapter. CHAPTER 5 provides several boiling simulations to demonstrate and validate the model capabilities under various scenarios. The single bubble growth with non-uniform temperature distribution demonstrates the model performance with a sharp temperature gradient condition. The single bubble pool boiling simulation shows the model potential in investigating boiling mechanism in pool boiling, for example, bubble departure diameter, bubble release frequency, etc. The single-bubble flow boiling simulation examines the model performance under a constantly changing velocity and temperature field. The multiple bubble flow boiling simulation provides the possibility to use this model in complex geometry like subchannel with spacer grid in the future. CHAPTER 6 is the conclusion of current research progress. The recommendations for future work are discussed in CHAPTER 7.

CHAPTER 2. NUMERICAL METHOD

This chapter describes the numerical method utilized in the high-resolution boiling simulations including the multiphase flow solver (PHASTA), the interface tracking method (level-set method), the evaporation and condensation model, the contact angle control algorithm and the bubble tracking algorithm. These components provide the basis for the presented research.

2.1. PHASTA Overview

The finite-element based code, PHASTA is utilized for the presented model development research. PHASTA is an advanced flow solver, and the abbreviation stands for Parallel, Hierarchic, higher-order accurate, Adaptive, Stabilized, Transient Analysis. It has been proved to be an effective and powerful tool for a broad spectrum of single and two-phase flow applications [85]. This numerical tool has been demonstrated to be useful for a wide range of modeling approaches for turbulent flow simulations [85], including Reynolds-averaged Navier-Stokes (RANS) models, large-eddy simulation (LES), detached eddy simulation (DES) and direct numerical simulation (DNS). PHASTA is the first unstructured grid LES code [86]. The anisotropic adaptive algorithms [87] and LES/DES models[88] have been implemented and used in the PHASTA workflow [89]. It has been shown to reliably predict the details of adiabatic phenomenon in single-phase flows. Those powerful capabilities have been expanded to two-phase flow modeling through implementation of an interface tracking method [90]. The interaction between bubble and flow [91], bubbly turbulence [92] and basic two-phase heat transfer problems [80, 93] have been studied recently. Moreover, it has been shown to be highly scalable on top supercomputers (nearly perfect scaling on up to 3 million mesh partitions using a 92 billion element mesh [94]).

2.2. Governing Equations

Whiting and Jansen [85] presented the temporal and spatial discretization of the *Incompressible Navier-Stokes* (INS) equations using finite element method in PHASTA code. The basic theory of this method has been presented in several prior publications [92, 95]. However, since the boiling model in this thesis is implemented through the modification of the flow solver, it is important to review the governing equations and level-set equations. This is necessary to provide a clear understanding of how the presented boiling model is designed. The strong form of the INS equations (including continuity, momentum and energy equations) is [88]:

$$u_{i,i} = 0 \tag{2-1}$$

$$\rho u_{i,t} + \rho u_j u_{i,j} = -p_{,i} + \tau_{ij,j} + f_i \tag{2-2}$$

$$\rho c_p \left(\frac{\partial T}{\partial t} + (\vec{u} \cdot \nabla)T\right) = \nabla \cdot (k\nabla T) + \vec{q} \tag{2-3}$$

where u is the fluid velocity, ρ is the density of the fluid, p is the static pressure, τ_{ij} is the viscous stress tensor and f_i represents the component of the body force. T is the absolute temperature of the fluid. c_p denotes the specific heat at the constant pressure($c_p \approx c_v$ for incompressible flow) and k is the thermal conductivity. $\vec{q}$ is the dissipation function respresnting the work done against viscous forces, which is irreversibly converted into internal energy.

The viscous stress tensor can be expressed using the liquid's viscosity and strain rate tensor for the incompressible flow of a Newtonian fluid as:

$$\tau_{ij} = 2\mu S_{ij} = \mu\left(u_{i,j} + u_{j,i}\right) \tag{2-4}$$

The surface tension effect is implemented as a local interfacial force density (f_i) by utilizing the Continuum Surface Force (CSF) model of Brackbill et al. [96]. It is noted that energy equation is decoulped from continuity and momentum equation for incompressible flow. The continuity and momentum equations are solved first to find the velocity and pressure distribution assuming

constant fluid properties for each phase. Then the energy equation are solved by itself when the velocity field is obtained.

2.3. Level-set Method

Sussman [73, 97-99] and Sethian [100] proposed an interface tracking method – the level set method, which modeled the interface as the zero level-set of a smooth function, φ. The scalar variable φ represents the distance from the interface as different level-set value. The sign of the level-set field indicates distinct phases and the zero level-set ($\varphi = 0$) determines the current interface location. The level-set field φ is advected through the computational domain with local fluid velocity according to the following equation:

$$\frac{D\varphi}{Dt} = \frac{\partial \varphi}{\partial t} + \boldsymbol{u} \cdot \boldsymbol{\nabla} \varphi = 0 \qquad (2\text{-}5)$$

where $\boldsymbol{u}$ is the local velocity vector. Typically, the positive value of level-set, $\varphi > 0$, indicates the liquid phase while the negative value, $\varphi < 0$, indicates the gas phase.

The 'one-fluid' formulation is utilized to describe the two-phase flow system in level-set method: the same set of conservation equations are used for the entire computational domian, but the fluid properties vary sharply across the interface from one phase to the other. The two-phase system is treated as a continous fluid whose properties vary from liquid phase to gas phase over a narrow range of values defined by the level-set field [101]. The properties near the interface are defined using a smoothed Heaviside kernel function, H_ε, in Eq. (2-6) to avoid the computational instability caused by the discontinuity in physical properties [98]:

$$H_\varepsilon(\varphi) = \begin{cases} 0 & , \varphi < -\varepsilon \\ \frac{1}{2}\left[1 + \frac{\varphi}{\varepsilon} + \frac{1}{\pi} sin\left(\frac{\pi\varphi}{\varepsilon}\right)\right] & , |\varphi| < \varepsilon \\ 1 & , \varphi > \varepsilon \end{cases} \qquad (2\text{-}6)$$

Density and viscosity values in the domain are defined using the Heaviside kernel function (H_ε)and the level-set value as:

$$\rho(\varphi) = \rho_l H_\varepsilon(\varphi) + \rho_g\big(1 - H_\varepsilon(\varphi)\big) \quad (2\text{-}7)$$

$$\mu(\varphi) = \mu_l H_\varepsilon(\varphi) + \mu_g\big(1 - H_\varepsilon(\varphi)\big) \quad (2\text{-}8)$$

A re-distancing operation is introduced to make the distance field accurate throughout the domain as this distance field is being stretched by local velocity evolution [98]:

$$\frac{\partial d}{\partial \tau} = S(\varphi)[1 - |\boldsymbol{\nabla} d|] \quad (2\text{-}9)$$

Here d is a scalar representing the updated distance field, and τ is the pseudo-time variable over which this re-distancing equation is solved to achieve steady-state condition. The equation can be re-written as a transport equation for more straight-forward implementation in a typical advection equation scalar solver [102]:

$$\frac{\partial d}{\partial \tau} + \boldsymbol{w} \cdot \boldsymbol{\nabla} d = S(\varphi) \quad (2\text{-}10)$$

$$\boldsymbol{w} = S(\varphi)\frac{\boldsymbol{\nabla} d}{|\boldsymbol{\nabla} d|} \quad (2\text{-}11)$$

where d is initialized as the level set field and then advected with a pseudo velocity $\boldsymbol{w}$. The velocity vector $\boldsymbol{w}$ is defined to be directed away from the interface using a smoothed function $S(\varphi)$ as:

$$S(\varphi) = \begin{cases} -1 & ,\varphi < -\varepsilon_d \\ \left[\dfrac{\varphi}{\varepsilon_d} + \dfrac{1}{\pi}\sin\left(\dfrac{\pi\varphi}{\varepsilon_d}\right)\right] & ,|\varphi| < \varepsilon_d \\ 1 & ,\varphi > \varepsilon_d \end{cases} \quad (2\text{-}12)$$

where ε_d is the distance field interface half-thickness which, in general, may be different from ε used in Eq. (2-6).

2.4. The Evaporation and Condensation Model

The evaporation and condensation model in the presented research is designed to resolve 3D interface in complex geometries represented with unstructured meshes. This unique capability allows us to investigate the boiling phenomenon under various conditions with lower cost (by utilizing localized mesh refinement for bubble growth region) compared to uniformly refined structured meshes. The objectives of this research effort are two-fold. One of them is the verification and validation of the evaporation and condensation model. The other objective is to demonstrate the potential of this approach in large-scale multiple bubble simulations. The verification is done by comparing single bubble growth rate with the analytical solution [36] and performing mesh sensitivity study and superheat rate parametric study. Validation of the model is carried out by the comparison between the simulation of pool and flow boiling phenomenon and reference datasets. In the pool boiling simulation, the numerical bubble release frequency is validated against the commonly-used experimentally-based correlations. In the flow boiling simulation, bubble evolution and growth rate are compared with the experiment done by Maity [103] for validation purpose.

There are also several demonstration cases considered in the presented research. In the single bubble growth simulation, a linear temperature profile with sharp gradient is applied to examine the evaporation and condensation model under non-uniform temperature distribution. The single bubble growth and departure simulation shows the model potential in investigating boiling mechanism in pool boiling, for example, bubble departure diameter, bubble release frequency, etc.

The single-bubble flow boiling simulation examines the model performance under a constantly changing velocity and temperature field. Both constant temperature and constant heat flux boundary conditions have been applied to the flow boiling simulations and the temperature distributions are compared. The overall behavior is close to the experimental observations.

The multiple bubble flow boiling simulation provides the possibility to use this model in complex geometry like subchannel with spacer grid in the future. The flow is heated by the heater in the wall with the constant heat flux. The multi-bubble simulation aims to demonstrate the potential of the code in studying local bubble behavior, and possible bubble-bubble interactions in flow boiling scenarios. The bubble dynamics information including bubble trajectory, growth rate, etc. is collected individually from each bubble. This unique capability could be applied to large scale high-resolution boiling simulation to help improve multiphase computational fluid dynamics models and perform high-resolution virtual experiments.

2.5. The Contact Angle Control Algorithm

The contact angle control algorithm implemented in PHASTA is designed for full 3D resolution, including complex nuclear reactor subchannel geometries which can be explicitly represented by unstructured computational grids. The motivation of this work to obtain the evolution of contact angle during the bubble departure. The development of the contact angle control algorithm started with Wonnell and Bolotnov [104], who conducted the parametric studies on the effects of various initial contact angle and initial bubble diameters on bubble departure. To continue this work, Zeng and Bolotnov [105] verified the contact angle control algorithm using theoretical force-balance analysis and investigated the capillary effect. It is noted that the version of PHASTA which they utilized to develop the contact angle control algorithm is quite different from the current version of PHASTA used in the research group. Therefore, the task of the author is to bring this capability to the latest version of PHASTA, improve and couple it with other existing capabilities like the evaporation and condensation model.

The basic idea of this contact angle control algorithm is to use a subgrid force model to control the evolving contact angle. This control force is applied when the current contact angle

deviates from the desired value (or range of values) and decrease to zero when the current contact angle reaches the desired value. The advancing and receding contact angles are treated separately in consideration of the lateral movement of the bubble. This model is verified by force balance analysis and coupled with evaporation and condensation model in PHASTA. The detailed description and results will be shown in CHAPTER 4.

2.6. The Bubble Tracking Algorithm

The recent progress in ITM simulation capabilities provide resolved bubble behavior and heat transfer process during boiling, but also produce large amount of numerical data containing hydrodynamic and thermodynamic information. This brings up the issue of efficiently extracting useful numerical information from thousands of bubbles in the domain over simulation time. The idea on collecting the detailed information regarding the individual bubble behavior in level-set method is developed and implemented by Fang et al. [19]. The *Bubble Tracking Algorithm* (BTA) introduced a marker/ID field in PHASTA to identify and track each individual bubble in the domain as shown in Figure 2.1. The nodes inside the region of interest are colored by the corresponding bubble ID while the rest of the domain is marked by zero ID value. The region of interest consists of two parts: the bubble region (to collect the bubble-related information) and a near interface liquid shell (to collect local liquid information). The position of the liquid shell is described using BTA epsilon (ε_{BT}) which is a user-defined value (around the local element size value). The typical thickness of BTA liquid shell is about $1\varepsilon_{BT}$ to $3\varepsilon_{BT}$ outside the bubble. The BTA can collect bubble information like bubble velocity, volume, deformation level, and even the local liquid velocity and shear rate. In the presented research this capability is coupled with the evaporation and condensation model as the tool to collect liquid temperature and temperature gradient near the individual bubble interface. The combination of bubble tracking algorithm and

evaporation/condensation model will help take the best advantage of computationally expensive large-scale simulations and allow for in-depth multiple-bubble simulation analysis.

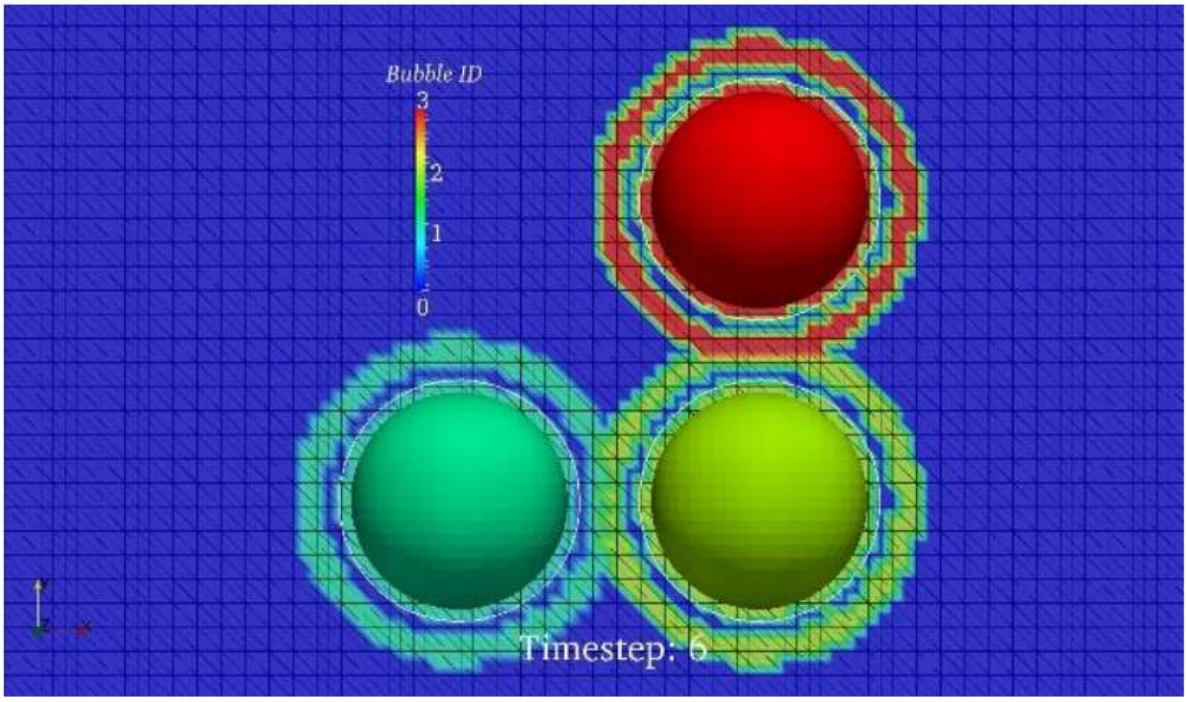

Figure 2.1. A slice of the domain in the three-bubble simulation colored by bubble tracking marker field (zero value indicates liquid field) [19].

CHAPTER 3. EVAPORATION AND CONDENSATION MODEL

This Chapter focuses on the development and verification of the evaporation and condensation. The three-step approach utilized in the model developing process and the results of model verification are presented. The mesh resolution sensitivity study and parametric study of superheat rate are conducted. The multi-bubble growth is presented and verified as well. The energy conservation problem during bubble condensation is discussed in the end of the chapter.

3.1. Model Assumptions

Several assumptions have been made to develop this evaporation and condensation model. First, the fluid properties of the two phases (liquid and vapor) including density, viscosity, thermal conductivity, etc. are assumed to be constant in the boiling simulation. This assumption is valid for low superheat scenarios (within 15 degrees of superheat), where the liquid viscosity changes by about 9% and other thermos-physical properties change by less than 3% when the temperature increases from 100℃ to 110℃. Second, the temperature of the vapor phase is constant and equal to the saturation temperature, T_{sat}. We assume that the vapor temperature is related to the bubble growth rate through the energy balance requirement, which related the rate of vapor generation to the heat flux at the vapor-liquid interface (and the temperature distribution in the liquid) [37]. The similar approach is used in other boiling models [14, 16].The direct energy transfer from the heated wall to the vapor when the bubble is sitting on the wall is discussed in Appendix.G. Third, the volumetric source term estimated from the averaged heat flux across the interface can be uniformly added into the bubble. This approach ignores the effect of local temperature variance on the bubble growth, for example, in subcooled boiling the bubble may condense on the top and evaporate in the bottom region. In exchange, the averaging makes the simulations more stable and allows for smooth bubble growth and condensation even during possible localized temperature fluctuations.

The micro-layer evaporation is not considered in the current model at this point. The model form error introduced by this assumption is acceptable under the current simulation scenarios according to the presented verification and validation results. The improvement approach is discussed in CHAPTER 7.

3.2. Phase-Change Modeling

A single vapor bubble growth in superheated water is simulated for the verification of the model implementation. In this scenario, the liquid is assumed incompressible, and no gravity force is applied to keep the bubble motionless relative to the liquid as in the corresponding analytical solution. The verification procedure consists of three major steps: (a) an analytical model is used to estimate the interface mass transfer due to evaporation. This analytical growth rate determined by the Scriven's solution [36] is utilized by the mass conservation equation as a volumetric source term to represent the added volume to the vapor bubble during the modeled evaporation process; (b) the energy equation is added in the liquid solution and the local temperature gradient is estimated to obtain the averaged heat flux through the interface according to the temperature distribution around each individual bubble (vapor temperature is forced to be at saturation); (c) the volume increase based on average heat flux rather than analytical growth rate is fed into the mass conservation equation as a volumetric source term controlling the growth rate. For each step the solution is verified against corresponding analytical result.

The step-by-step approach is essential to examine the correctness of the model implementation and to estimate the numerical error at each implementation step. The first step examines the capability of the incompressible flow solver by adding volume to the portion of the domain which represents steam produced by phase-change process. The second step ensures the coupled capability of solving interface tracking equations along with the energy equation (The

level set scalar and temperature are solved using the same scalar equation solver in PHASTA using different coefficients in advection and diffusion terms). The third step couples the scalar equation which calculates the volume increase/decrease of phase-change with continuity and momentum equation.

The geometry setting of this case is as follows: the single bubble is placed in the center of the cubic domain ($1.2mm \times 1.2mm \times 1.2mm$) shown in Figure 3.1. The initial radius of the bubble is $0.02\ mm$. The simulations were carried out on the computational mesh with 729,000

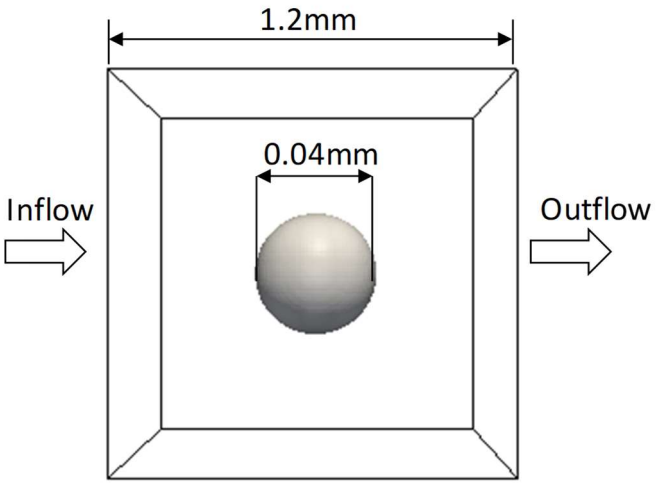

Figure 3.1. The simulation domain with initial bubble size for single bubble growth simulation.

tetrahedral elements and utilized 64 processing cores on our local cluster. The heat transfer process is considered in the second and third step. The inflow/outflow boundary conditions are applied to two side walls shown in Figure 3.1 while the no-slip boundary condition (representing solid walls) is applied to the rest of the domain faces. The liquid phase in the domain is initially superheated water (105℃, 1.0atm) and the gas phase is saturated vapor (100℃, 1.0atm) under atmosphere pressure. The inlet temperature is superheated at 5 ℃ (105℃). The adiabatic condition is applied to all the walls of the domain in the first and the second steps. In the third step, the top and bottom wall are assigned with the constant wall temperature boundary condition. It is noted that the net volume increase due to the difference between vapor and water density is significant. Therefore,

the inflow/outflow boundary condition is necessary to compensate the volume change in the domain for phase-change simulations using incompressible flow solver.

3.3. Semi-analytical Growth Model

In the inertia-controlled growth phase, the analytical growth of the bubble is described by the following equation:

$$R = 2\beta\sqrt{a_l t} \qquad (3\text{-}1)$$

The detailed derivation of the analytical solution can be found in Scriven's paper [36]. The bubble growth rate constant β could be solved using the equation below with successive approximation, given the degree of superheat and the requisite physical properties,

$$\frac{\tau}{\xi + \omega\upsilon\tau} = 2\beta^3 exp((\beta^2 + 2\epsilon\beta^2)\int_{\beta}^{\infty} x^{-2} exp(-x^2 - 2\epsilon\beta^3 x^{-1})dx) \qquad (3\text{-}2)$$

The form of the solution for different superheats is given by Scriven as shown in Figure 3.2 [36]. The value of the bubble growth rate constant β used in model verification is obtained from Figure 3.2 and listed in Table 3-1.

The volumetric source term is added to the right-hand side of mass conservation equation (Eq.(2-1)) to model the bubble growth process. The analytical growth rate in regard of bubble radius is given as:

$$dR = \beta \cdot \frac{1}{\sqrt{a_l t}} \qquad (3\text{-}3)$$

The steam volume gain in the bubble is:

$$dV = \frac{4}{3}\pi \cdot 3R^2 dR = 4\pi R^2 dR = 8\pi\beta^2 R \qquad (3\text{-}4)$$

This volumetric source term is uniformly added into the elements within 1ε to 2ε region from the interface inside the bubble (The associated PHASTA source code is presented in Appendix H.11).

The thickness of this volumetric adding region is determined as the product of the epsilon value and the local element size. The use of relative thickness definition makes it convenience for the

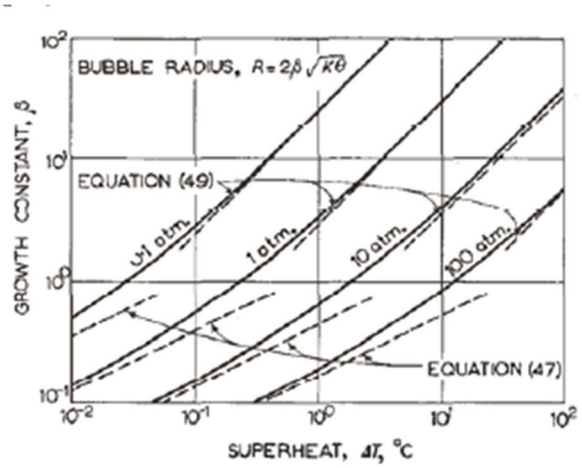

Figure 3.2. The solution to the vapor bubble growth rate constant (Eq. 3-2) [36].

applications in non-uniformly refined domain. The source code associated with semi-analytical growth model in PHASTA is presented in Appendix H.1.

Table 3-1: The bubble growth rate constant used in analytical solution [36].

The superheat rate	2.5	5.0	7.5
The growth rate constant β	11	17	22

3.4. Average Temperature Gradient Estimation

PHASTA have not been traditionally used to solve multi-phase heat transfer problems, but the heat transfer process must be considered for boiling simulation. Therefore, some modifications have been made for two-phase heat transfer simulations: (a) the energy equation needs to be included in the liquid phase solution (The associated PHASTA source code is presented in Appendix H.3 and H.4); (b) the local temperature gradient needs to be estimated according to the temperature distribution around every bubble for heat flux calculation (The associated PHASTA source code is presented in Appendix H.7). The previous energy equation in PHASTA is designed

for single-phase flow so it is coded in non-dimensionless form. However, for two-phase heat transfer problem the thermal properties cannot be simplified with non-dimensionless number like Reynolds number and Prandtl number. In LS method, level set value is utilized to distinguish different phases and the thermal properties are applied accordingly(The associated PHASTA source code is presented in Appendix H.2).

At the interface, the smoothed Heaviside function is used to transition the fluid properties as shown in Eqs. (3-5) and (3-6).

$$c_p(\varphi) = c_{p_l} H_\varepsilon(\varphi) + c_{p_g}(1 - H_\varepsilon(\varphi)) \quad (3\text{-}5)$$

$$k(\varphi) = k_l H_\varepsilon(\varphi) + k_g(1 - H_\varepsilon(\varphi)) \quad (3\text{-}6)$$

The temperature inside the bubble is fixed to be saturation temperature to maintain the energy balance due to phase-change heat transfer (The associated PHASTA source code is presented in Appendix H.6). The local temperature gradient is estimated for each element within the temperature gradient collection shell shown in Figure 3.3 (the yellow region). The temperature gradient changes sharply near the interface, therefore the collection shell should be as close as possible to the interface to reduce the estimation error. Meanwhile, the property discontinuity at the interface results in the mix property region (including conductivities/heat capacities) in the

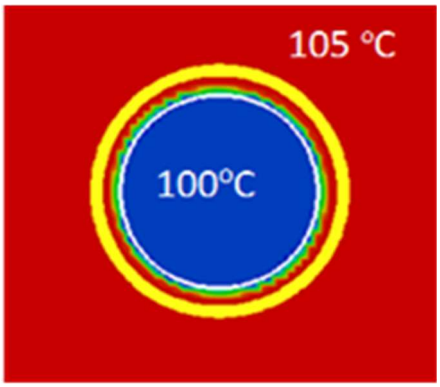

Figure 3.3. The schematic of average temperature gradient collection region in the evaporation and condensation algorithm (The yellow region indicates the shell where the local temperature gradient is collected.).

fluid fields, which also introduces error in the temperature gradient calculation. Considering these two factors above, the region between 1ε and 2ε from the interface are selected as the temperature collection shell in the simulations. The epsilon value used in the temperature collection shell is consistent with the one for bubble tracking algorithm (Section 2.6). The BTA liquid shell is utilized to collect the temperature gradient information for each individual bubble according to its own local temperature field. During bubble growth time, the relative velocity between the bubble and surrounding liquid is quite small in pool boiling and low-velocity flow boiling, so the heat convection in the liquid vicinity of bubble interface is neglected. The heat conduction mechanism is assumed to dominant the heat transfer process. The local heat flux through the collection shell is expressed as follows,

$$q'' = -k_l \frac{\partial T}{\partial r} \qquad (3\text{-}7)$$

where k_l is the thermal conductivity of the liquid phase.

Assuming the average radius of the collection shell is R_1, the bubble radius is R_0 and the total energy is conserved through the all concentric spheres of the bubble (e.g. the collection shell), the heat flux at the interface (q'') can be extrapolated using the following equation,

$$q'' = \left(\frac{R_0}{R_1}\right)^2 q_1'' \qquad (3\text{-}8)$$

3.5. Temperature Gradient Drive Growth

In the third step, the scalar equation is coupled with the continuity and momentum equations to achieve bubble growth. Considering the non-identical element size in unstructured mesh, the local heat flux estimated in the second step is averaged according to the element volume weight,

$$\bar{q} = \left(\sum_{i=1}^{N} q_i'' \cdot V_i \right) / V_{shell} \qquad (3\text{-}9)$$

Then the average heat flux around the bubble is converted into volume change of evaporation/condensation and applied to the continuity equation as a volumetric source term,

$$dV = \frac{4\pi R_0 \bar{q}}{h_{fg}(\rho_l - \rho_g)} \qquad (3\text{-}10)$$

where h_{fg} is the latent heat of evaporation, ρ_l is the density of the liquid phase and ρ_g is the density of the gas phase.

This volumetric source term is uniformly added into the elements within 1ε to 2ε region from the interface inside the bubble (the yellow region indicated in Figure 3.4). As the bubble grows, the interface moves outward the bubble center and pushes away the liquid around the interface to make room for the phase-change volume. The 1ε to 2ε region inside the bubble

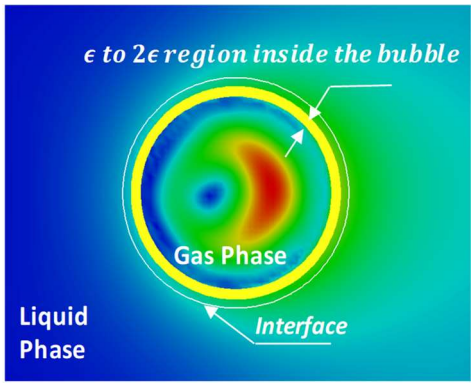

Figure 3.4. The schematic of volumetric source term adding region in the evaporation and condensation algorithm (The yellow region indicates the shell where the volumetric source term is added.).

interface is selected for two reasons. First, as mentioned above the property discontinuity at the interface results in the mix property region (including conductivities/heat capacities) in the fluid fields. The volumetric source term due to phase-change is deliberately avoided in this smoothed buffer region. Second, the velocity field of gas phase is also disturbed when the extra volume is added into the bubble. For incompressible flow solver, the pressure is instantaneously determined

by the velocity field, typically solved by the Poisson equation for pressure. The volumetric source term adding into this region may cause instabilities in the velocity and pressure fields and lead to unphysical behavior at the interface. The volumetric source term region along with the temperature gradient collection region mentioned above is selected as a result of balancing the accurate physics representation with numerical stability. It has shown to be effective approach when applied to various boiling scenario simulations and validated against known analytical solutions (The associated PHASTA source code is presented in Appendix H.10).

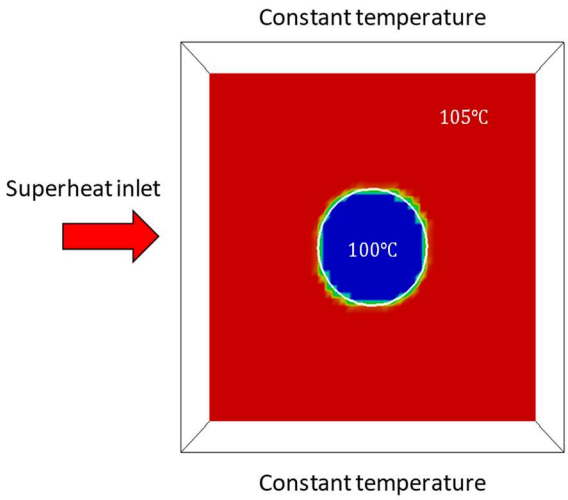

Figure 3.5. The initial temperature distribution of bubble verification case.

3.6. Model Verification

The geometry setting of the verification case is shown in Figure 3.1. The initial radius of the bubble is 0.2 mm.The initial temperature of the domain is 105℃ and the temperature inside the bubble is fixed at 100℃. The inflow/outflow boundary condition is applied to two side walls as shown in Figure 3.1 while the no-slip boundary condition is applied to the rest of the domain faces. The superheated wall temperature boundary condition is applied to the top and bottom of the domain as shown in Figure 3.5. The adiabatic condition is applied to the rest of the faces in the domain. The thermodynamic properties used for the simulations are listed in Table 3-2. The screenshots of bubble growth in the uniformly heated water are presented in Figure 3.6. A small inlet velocity is applied on the left side of the domain to avoid undesirable solution backflow at the oulet face. The liquid is pushed through the right outflow boundary as the bubble grows. The verification is performed by comparing single bubble growth rate with the analytical solution [36]. The sensitivity study of mesh and superheat rate on bubble growth rate is discussed as well.

Table 3-2: Thermodynamic properties used in the simulation.

	Water	**Vapor**
Density kg/m^3	958.0	0.579
Thermal conductivity $W/(m \cdot ℃)$	0.679	0.025
Specific heat $kJ/(kg \cdot ℃)$	2.80	2.034
Superheated temperature ℃	105	
Saturation temperature ℃	100	
Latent heat kJ/kg	2260.0	

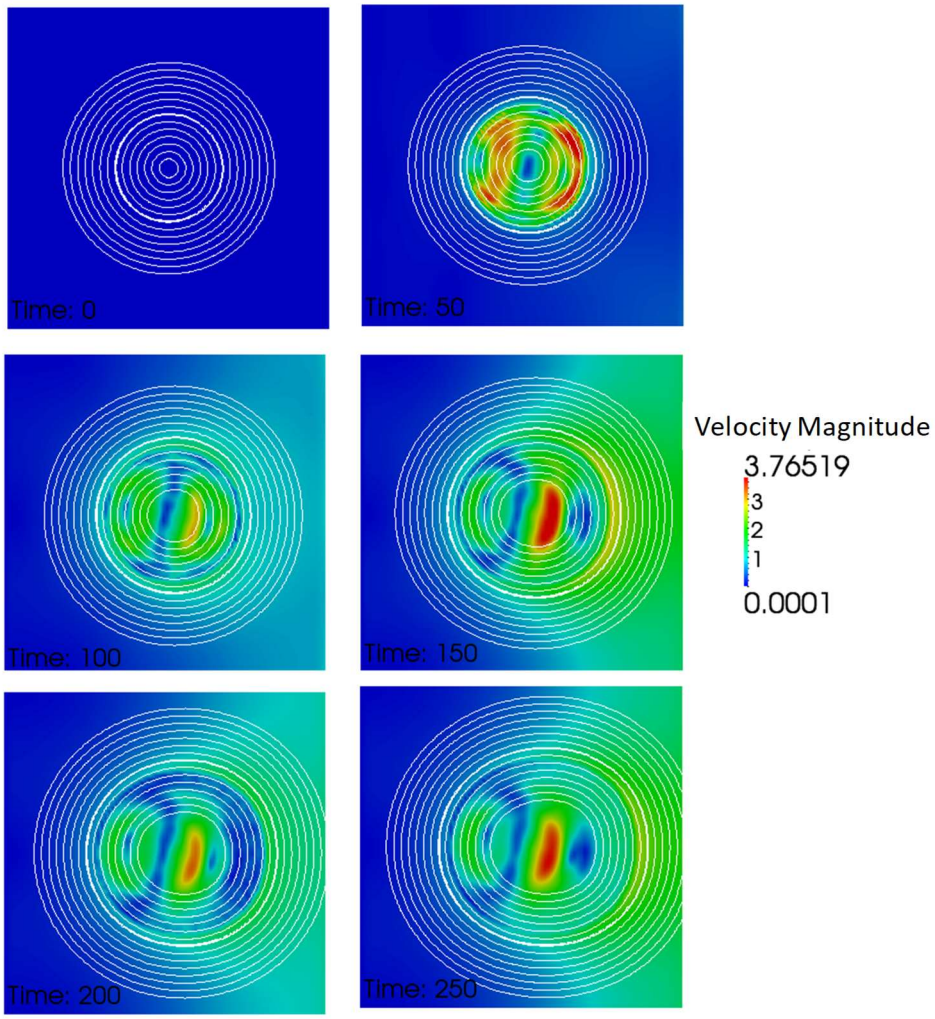

Figure 3.6. The growth of a saturated bubble (colored by the velocity field).

3.6.1. Mesh Sensitivity Study

Mesh sensitivity study is performed for the bubble growth case where the liquid superheat is equal to 5℃ to examine the code performance with different element sizes. The total mesh in the domain starts with 0.16 million finite elements (0.16M) and increases to 0.37M and 0.73M. The thermodynamics properties remain the same for all three simulations (Table 3-2). The initial bubble size is 0.2 mm. The numerical results is compared with the prediction of analytical solution (3-1) for 500 time steps (this corresponds to simulated time of 0.25 ms). The evolution of the bubble radius is shown in Figure 3.7. The numerical bubble growth rate is very close to the analytical results for all three mesh (within 0.0015 mm radius difference during the simulation time). As the simulation time increases, the difference between meshes becomes visible. The

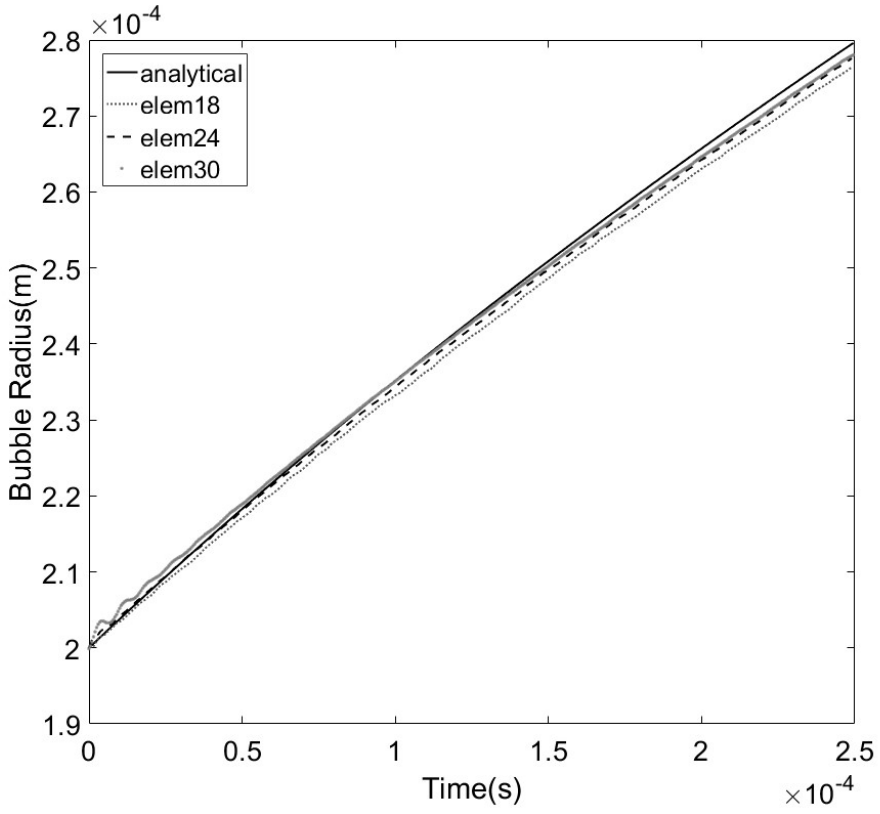

Figure 3.7. The numerical results (The legend indicates 18, 24 and 30 elements across starting diameter) of bubble growth compared with the analytical results (solid line).

bubble radius in the coarse mesh (0.16M) is smaller than those in the finer meshes (0.37M&0.73M)

at same time step. For the simulation with mesh size of 0.37M, the difference between the analytical and numerical results decreases significantly (to less than 0.0031 mm radius difference over the simulation time). The difference of bubble radius is visibly small (less than 0.0016 mm radius difference) when the mesh increases from 0.37M to 0.73M, and the relative error in numerical growth rate decrease from 3.79% to 1.85% in 500 time steps. The relative error (ε) is estimated using the numerical bubble radius increase over 500 time steps versus the increase in the analytical results as shown below,

$$\varepsilon = \left(1 - \frac{\Delta R_{numerical}}{\Delta R_{analytical}}\right)\% \qquad (3\text{-}11)$$

The quantitive comparision between numerical results and analytical solution is summarized in Table 3-3.. The L_2 norm, as a common used norm for evaluating the discretization error, is calculated to show the similarity between the numerical and analytical results.

Table 3-3: The mesh analysis of numerical bubble growth.

Elements across the diameter	Total Number of Elements	Initial Radius(m)	Relative Error	L_2 norm
18	157,464	0.0002	3.79%	2.1041×10^{-6}
24	373,248	0.0002	2.59%	1.1231×10^{-6}
30	729,000	0.0002	1.85%	8.8188×10^{-7}
$\varepsilon = \left(1 - \frac{\Delta R_{numerical}}{\Delta R_{analytical}}\right)\%$; $L_2 = \left(\frac{1}{n}\sum_{1}^{n}(r_{num} - r_{ana})^2\right)^{1/2}$				

3.6.2. Liquid Superheat Study

The superheat of the surrounding liquid is a key parameter which controls the bubble growth rate. This study aims to examine the model performance with different liquid superheat values ($\Delta T = 2.5℃, 5.0℃, 7.5℃$) under atmospheric pressure. The domain design (Figure 3.1) and the initial condition (Figure 3.5) remains the same as the one used for the mesh sensitivity study

except for the liquid superheat. Considering the computational cost and simulation accuracy, the total mesh of the domain is set to be 0.37M. According to the mesh sensitivity study, the expected discretization error (Eq.(3-11)) is around 2.59% for the bubble growth simulation. The relative error is estimated using the numerical bubble radius increase over 300 time steps versus the increase in the analytical results under the same condition. The comparison between numerical growth rate and the analytical solution is summarized in Table 3-4. The diagonal plot for different liquid superheat values is shown in Figure 3.8. The slope of the plot shows the consistency between analytical results and numerical results. The slope of the data points parallel to the diagonal line indicates that the numerical radius is equal to the analytical prediction. If the slope is larger than the diagonal, the bubble radius is overpredicted in the simulation. If the slope is smaller, the numerical bubble radius is underpredicted. It is observed that the relative error varies for different liquid superheat values. For the liquid superheat equal to 2.5℃, the numerical bubble growth rate is the closest to the analytical prediction. As a result, the relative error over 300 time steps is the smallest among three cases. When the liquid superheat is 5.0℃, the numerical bubble radius increases slightly quicker than the analytical one. For the liquid superheat equal to 7.5℃, the error of numerical prediction fluctuates during the bubble growth. The variance of numerical error for different liquid superheat simulations can be improved by increasing the domain size. It is noticed in Figure 3.6 that the bubble growth is affected by the inflow/outflow condition when the interface is close to the boundary. The shape of the bubble is not perfectly spherical as the assumption of analytical solution. The thermal boundary layer developed around the interface is slightly different from the analytical condition where the bubble grows in infinite superheat liquid. If the superheat of surrounding liquid is 2.5℃, the bubble radius after 300 time steps is still far from the boundary condition affected region while the bubble grows much faster when the liquid superheat is 7.5℃ ,

therefore the relative error could also be further eliminated by reducing the boundary condition effect (e.g. increasing the domain size) in the future.

Table 3-4: Numerical growth with different superheat values.

Superheat ΔT(℃)	**Analytical Radius (mm)**	**Numerical Radius (mm)**	**Relative Error**
2.5	0.2276	0.2282	2.36%
5.0	0.2508	0.2495	2.47%
7.5	0.2952	0.2921	3.26%
$\text{relative error} = \left(1 - \frac{\Delta R_{\text{numerical}}}{\Delta R_{\text{analytical}}}\right)\%$			

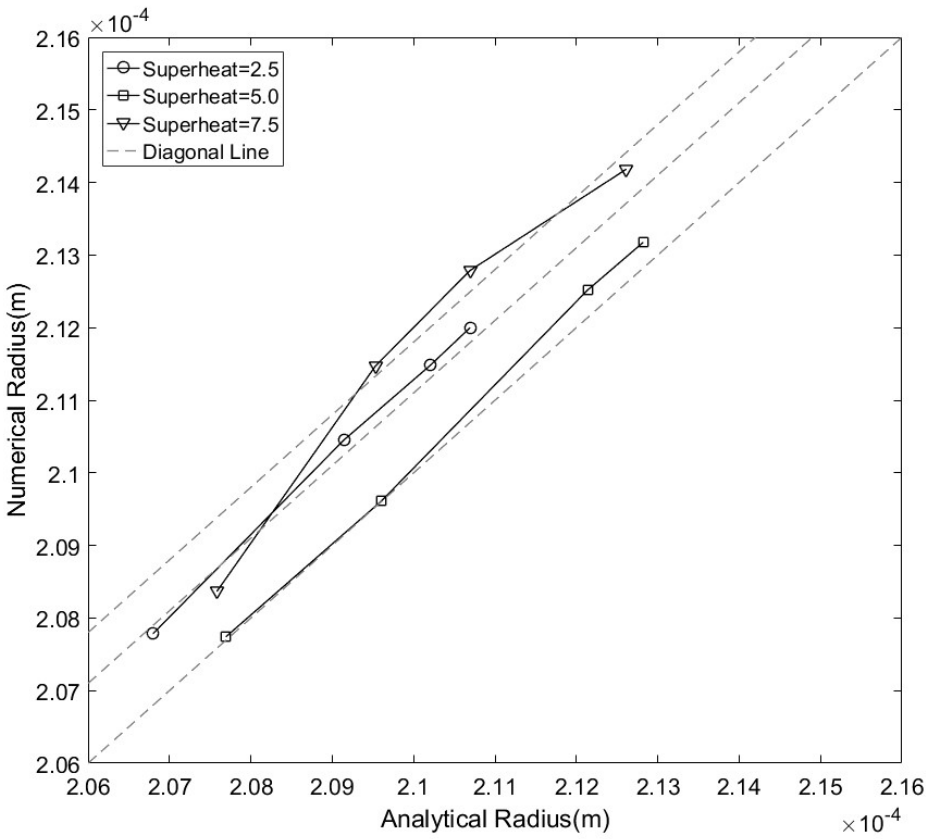

Figure 3.8. The numerical results (superheat rate 2.5, 5.0, 7.5) compared with analytical results at certain bubble radius.

3.7. Multiple bubble Growth Capability

The evaporation and condensation model is coupled with BTA in PHASTA to achieve multiple bubble growth capability. This capability is essential for studying the characteristics of boiling phenomenon like bubble release frequency, bubble departure diameter, nucleation site density and for applying the boiling model to engineering applications. The traditional level-set method cannot distinguish individual bubbles, which makes it challenging to simulate multiple bubble evaporation and condensation with complex fluid conditions. The local information in the vicinity of every bubble is necessary for the estimation of corresponding phase-change rates. BTA discussed in Section 2.6 introduced a marker/ID field in PHASTA to identify and track each bubble. The liquid shell colored by bubble ID is used to collect the temperature and temperature gradient for each bubble (The associated PHASTA source code is presented in Appendix H.8).

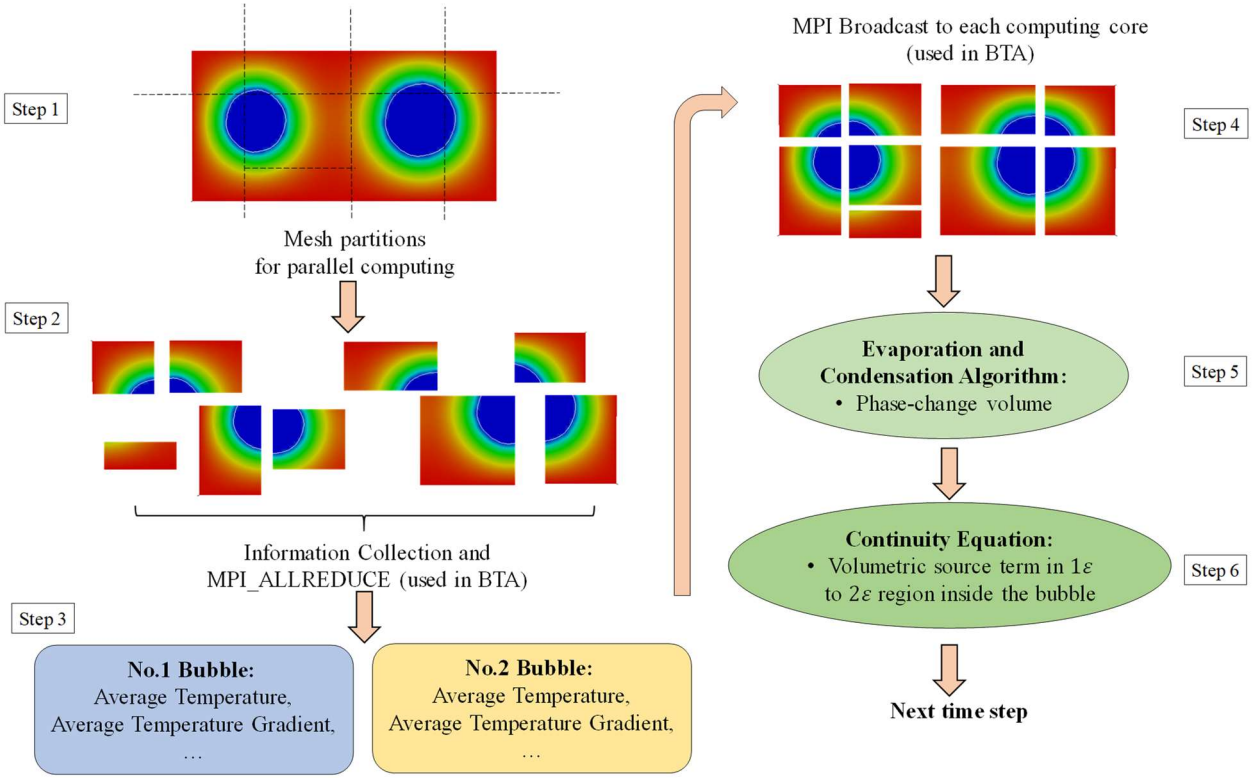

Figure 3.9. The schematic of multi-bubble boiling simulation in PHASTA.

The postprocessing tools are extended to include the heat transfer information and calculate the average temperature and temperature gradient for each bubble.

In parallel simulations commonly performed by PHASTA (the schematic of the process shown in Figure 3.9), the whole computational domain is divided into certain number of mesh partitions (3,000 to 100,000 elements per partition). Each computing core is only responsible for calculations of one mesh partition. Each mesh partition is built of smaller mesh units—mesh blocks (typically 64 elements) to facilitate efficiency in code performance through utilizing processing cores memory cache. In other words, even the information of same bubble can be distributed in different mesh blocks and processed simultaneously. Therefore, the full utilization of the Message Passing Interface (MPI) is needed to implement the evaporation and condensation model in

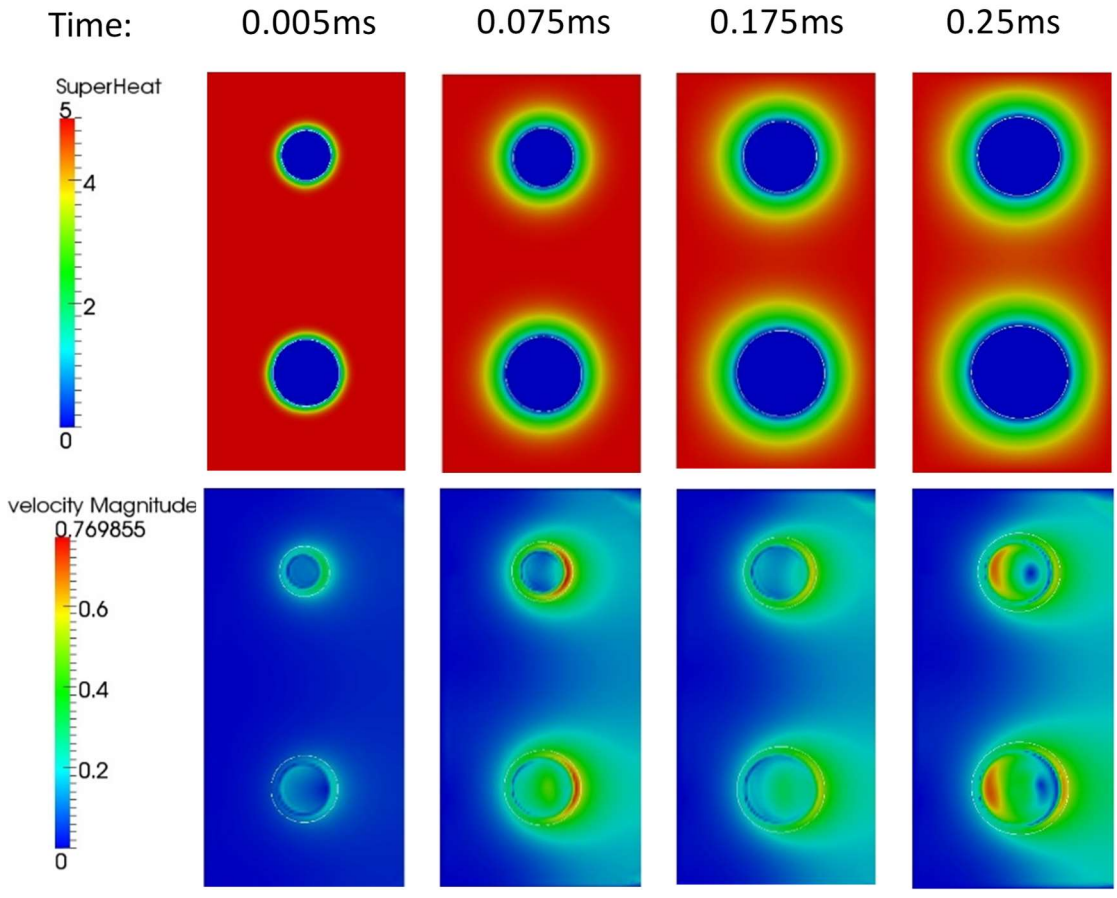

Figure 3.10. The screenshots of the velocity and temperature field when bubbles grow.

PHASTA. The MPI functions can collect the bubble information from all compute cores and broadcast the average temperature and temperature gradient data back to the cores. Then the evaporation and condensation algorithm builds an array which contains the phase-change volume information based on the average temperature gradient of every bubble in this block. After that, this array is passed to the continuity equation and used as the volumetric source term within the volumetric source adding region inside the bubble (The associated PHASTA source code is presented in Appendix H.9).

A two-bubble growth simulation is conducted to examine the performance of multiple bubble growth algorithm. The numerical bubble growth rate is compared with analytical results

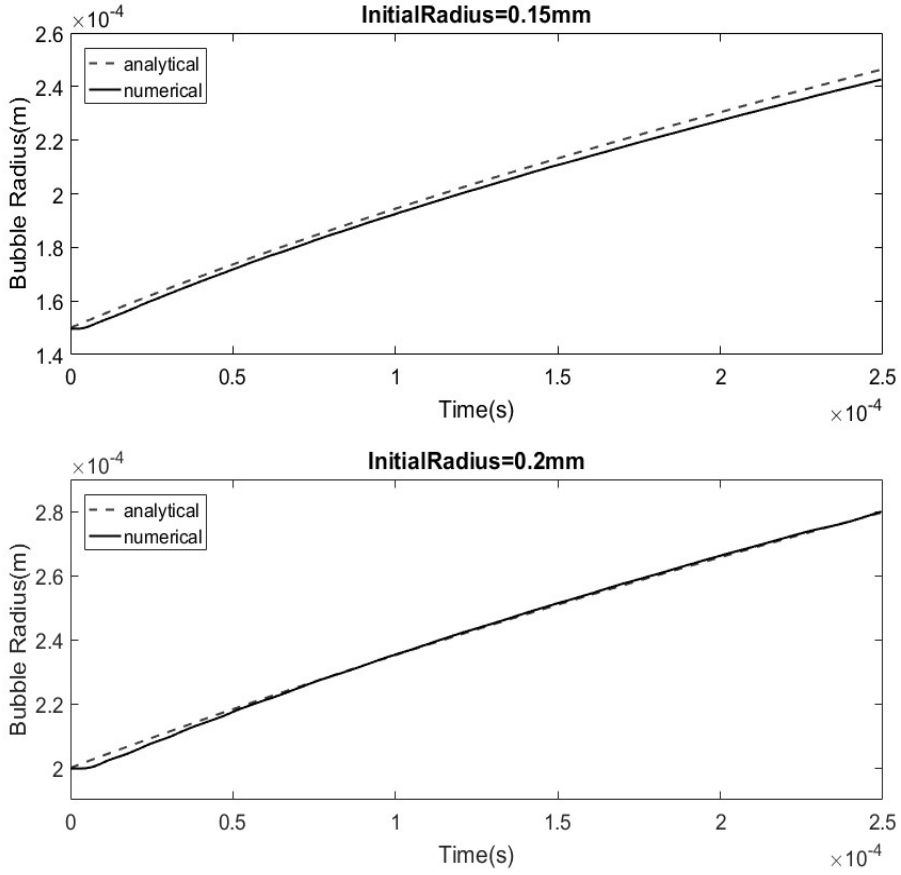

Figure 3.11. The comparison of bubble radii between numerical simulation and analytical solution.

for verification purpose. The initial bubble size is intentionally set different to test the coupling between the evaporation and condensation model and BTA. In this simulation, the liquid is incompressible and superheated. Two bubbles of different initial radii ($r_1 = 0.2\ \text{mm}, r_2 = 0.15\ \text{mm}$) are placed in the domain with the same distance to the walls from the bubble center. The liquid is superheated by 5℃ under atmospheric pressure. The constant temperature boundary conditions are applied to top and bottom wall with 5℃ superheat. The inlet/outlet boundary condition is applied to the left and right sides of the domain. As the solution progresses, a thermal boundary is developed around the bubble and velocity in the vicinity increases due to the interface movement as the bubbles are growing as shown in Figure 3.10. The comparison between numerical bubble radii and analytical prediction is presented in Figure 3.11, which shows good agreement (the relative error for r_1 is 2.5% and for r_2 is 1.92%).

3.8. Energy Balance during Bubble Condensation

In the evaporation simulations, the mesh resolution of the bubble (the number of elements across the bubble diameter) can always be sufficient to resolve the bubble shape and the interface accurately with proper local refinement. However, the mesh resolution of the bubble, unlike in the evaporation process, becomes coarser as the bubble condenses. Even with multiple refinement regions, it will come to a point when the bubble size is comparable to the element size so that bubble shape and interface may not be accurately resolved. The poor resolution of the bubble increases the discretization error and also results in unphysical mass loss (due to LS method) in the bubble simulation. In boiling phenomenon, the energy balance is important for overall heat transfer characteristics of the two-phase flow. Therefore, the simulations in this section aims to evaluate the energy conservation during bubble condensation especially when the bubble is eventually becomes under-resolved for any practical mesh resolution.

The same domain which was utilized in the verification simulation (Section 3.6) is selected for the condensation simulation (Figure 3.1). The initial bubble radius is $0.3\ \mathrm{mm}$, which is comparable to the largest radius after 500 time steps in the single bubble evaporation simulations (Section 3.6). The initial temperature of the domain is subcooled at 5 degrees ($95℃$) and the temperature inside the bubble is fixed at $100℃$. The inflow/outflow boundary condition is applied to two side walls as shown in Figure 3.1, while the no-slip boundary condition is applied to the rest of the domain faces. The subcooled wall temperature boundary condition is applied to the top and bottom of the domain at $95℃$. The adiabatic condition is applied to the rest of the faces in the domain. The thermodynamic properties used for the simulations are the same as used in the evaporation simulation (Table 3-2). The total mesh in the domain is 0.37 million finite elements

(initially 36 elements across the bubble diameter). The snap shots of velocity and temperature distribution during bubble condensation are presented in Appendix.D.

The evaporation and condensation is deactivated if the number of elements across the bubble diameter is less than 15 to avoid numerical instability, because the resolution at this point is so poor that there is not enough elements in the temperature collection shell and the volumetric source term adding shell. The analytical solution (Eq. (3-1)) based on conservation equations is used to estimate the theoretical condensation rate. Assuming the condensation is a reversible process of evaporation, so the growth constant β is same for $\Delta T = \pm 5℃$. Then the growth time required for the bubble radius increases from 0 to 0.3mm can be estimated as,

$$t = \left(\frac{R}{(2\beta\sqrt{a_l})}\right)^2 \qquad (3\text{-}12)$$

Here the initial radius R_0 is 0.3mm, so the corresponding growth time t_0 is 0.726ms. This growth time is used as a reference time in the bubble condensation radius calculation as,

$$r_{ana} = 2\beta\sqrt{\alpha_l(t_0 - t)} \qquad (3\text{-}13)$$

where t_0 is the reference time (0.726ms), t is the simulation time. The analytical solution is compared with the numerical results in Figure 3.12. In the beginning of the simulation, the numerical results are consistent with the analytical solution. As the bubble resolution (total number of elements across the bubble diameter) decreases, the numerical condensation rate becomes less than the analytical solution. The sharp gradient change in Figure 3.12 is due to the deactivation of the evaporation and condensation algorithm. It is noted that even though the evaporation and condensation model is deactivated, heat conduction still exists between the vapor bubble and subcooled liquid due to the saturated vapor temperature inside the bubble.

Figure 3.13 presents the evolution of energy transfer from the bubble to the surrounding liquid. Compared to the evolution of bubble radius, the energy conservation during bubble condensation is more essential in boiling simulation. The theoretical total energy from the bubble to the liquid is estimated,

$$Q = \frac{4}{3}\pi r_0^3 \cdot \rho_v / h_{fg} \qquad (3\text{-}14)$$

where r_0 is the initial radius of the bubble, ρ_v is the vapor density and h_{fg} is the latent heat of phase-change. The numerical energy transfer is estimated in two parts: 1. the volume change due to condensation is estimated using the numerical bubble radius; 2. the heat conduction is estimated using the temperature gradient data collected from the simulation. Even though the energy transfer rate in the simulation slows down at around $0.5ms$, the total energy transfer from the vapor to the surrounding liquid is very close to the analytical solution, which means that most energy transfer occurs in the early stage of bubble condensation. The energy inside the bubble can be completely

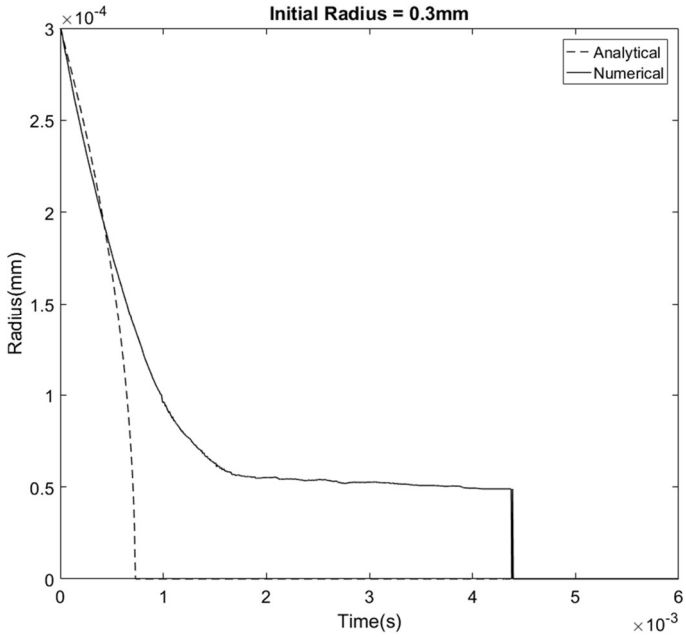

Figure 3.12. The comparison of bubble radius evolution in condensation simulation between analytical solution and numerical simulation.

transferred to the surrounding liquid during the condensation process if enough time is given. The

relative error between the theoretical energy transfer and numerical ones is 0.3307%. Therefore, we can conclude that the energy is conserved in the condensation simulation with the current boiling model.

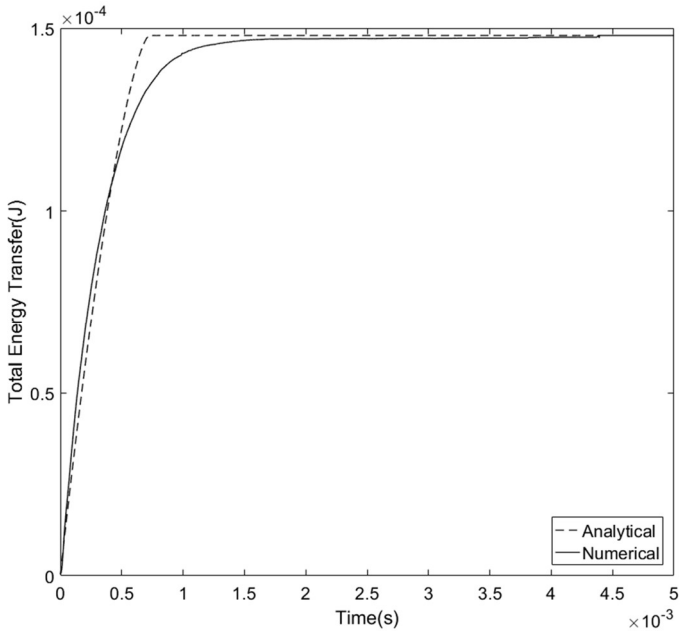

Figure 3.13. The evolution of energy transfer from the bubble to the surrounding liquid.

CHAPTER 4. CONTACT ANGLE CONTROL ALGORITHM[106]

The subgrid force model implemented in PHASTA to control the evolving contact angle is presented in this Chapter. The contact angle force is applied when the currently observed contact angle deviates from the desired value (or range of values) and decreases to zero when it reaches the desired value. The single bubble departure simulation is performed for verification purpose. The numerical results are compared with the analytical solution with good agreement. The mesh resolution sensitivity analysis and parametric study are conducted for the bubble departure simulations.

The development and implementation of the contact angle control algorithm for PHASTA code started by Wonnell and Bolotnov [104], who conducted the parametric studies on the effects of various initial contact angles and initial bubble diameters on the bubble departure events. Zeng and Bolotnov [105] continued this work and investigated the capillary effect using this contact angle control algorithm. It is noted that the version of PHASTA which they utilized for the development of the contact angle control algorithm is quite different from the current version of PHASTA used for large-scale bubbly flow simulations and two-phase phase-change simulations. Therefore, part of the author's Ph.D. work is to bring this capability to the latest version of PHASTA, to improve and to couple it with the other existing capabilities like the evaporation and condensation model. Most of the results presented in this Chapter has already been published in the Journal of Fluids Engineering.

4.1. Model Assumptions

There are several assumptions made in the presented implementation of the contact angle control algorithm. First, the solid surface is assumed to be ideal surface (smooth, flat and homogenous), which is consistent with the assumption of the analytical solution used for the model

verification purpose. The influence of the wall surface properties (e.g., surface roughness) can be considered in the selection of prescribed target contact angle value. Second, this contact angle algorithm is designed to be used within the length scale of interface tracking method (millimeter-scale). The micrometer-scale and nanometer-scale effects are represented by the value of prescribed target contact angle in the algorithm. As any other computational fluid dynamics flow modeling approaches, we do not directly simulate various surface materials. Instead, we use the target contact angle measured for certain material and conditions as our model input to show the influence of the surface material on the apparent contact angle. The contact angle model implemented in the solver mainly focuses on how we achieve this prescribed contact angle value and maintain this correct apparent contact angle in the simulations. Third, the dynamic contact angle could be estimated using the local interface normal vector and the wall normal vector in the wall-adjacent cell (boundary layer mesh is applied in this region). This is a common approach to contact angle calculation when the curvature and normal of the interface can be accurately and easily obtained through interface tracking methods such as Level-Set (LS) Method [64] and Conservative Level-Set (CLS) Method [65]. Fourth, the dynamic contact angle is bounded by the advancing contact angle and receding contact angle, which is expressed as a function of contact line speed. This method is first proposed by Bussman et al. [61] in their three-dimensional model of droplet impact onto asymmetric surface geometries. The similar approach is utilized by Mukherjee and Kandlikar [64] as well. They constructed a function of the dynamic contact angle with contact line speed in their pool boiling simulations.

4.2. Calculation of Local Interface Contact Angle

The current local contact angle is estimated using the local interface normal vector and the wall normal vector in the wall-adjacent computational cells. The level-set method models the

interface as zero level set and utilizes a smooth function of the level set, φ, where φ represents the signed distance from the interface. One of the major advantages of the level-set method is the straightforward approach to obtain the interface normal vector by taking the gradient of the level set field: $\nabla\phi$. The structured boundary layer mesh is utilized to obtain the accurate representation of the wall normal vector through a pre-computed distance to the wall scalar field. Using $|\nabla\phi| = 1$, the current contact angle could be estimated as

$$n_w \cdot \nabla\phi = cos(180° - \theta) = -cos\theta \qquad (4\text{-}1)$$

where n_w is the unit normal vector to the wall, θ is the contact angle at a certain location. The schematic plot is shown in Figure 4.1.

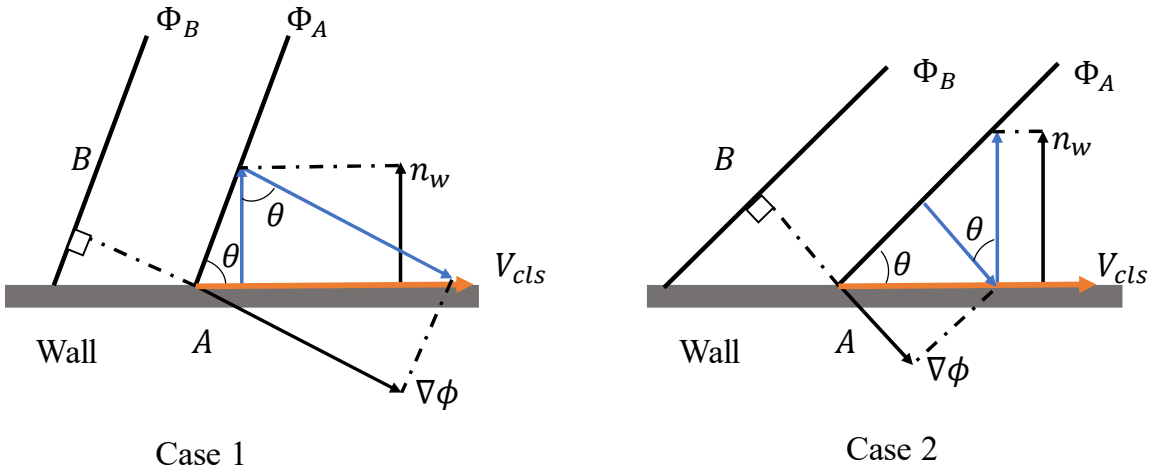

Figure 4.1. The schematic plot of contact angle calculation.

The target dynamic contact angle is calculated using the local contact line speed. When the bubble grows or slides along the wall, the local contact angles would vary due to the bubble movement. The value of the local contact angles is bounded by the advancing contact angle and receding contact angle. The function of the contact line speed is introduced to obtain the target contact angle at a given moment. The contact line speed (V_{cls}) is defined as positive when the contact line moves towards the gas side. The value of contact line speed is calculated using the tangent value of level set gradient and the wall normal vector as:

$$V_{cls} = u \cdot (\nabla\phi - (n_w \cdot \nabla\phi) n_w) \quad (4\text{-}2)$$

where u is the velocity vector at location A, n_w is the unit normal vector of the wall and $\nabla\phi$ is the gradient of the level set field.

When V_{cls} is greater than the maximum contact line velocity, the target contact angle is set to be the advancing contact angle obtained from experimental data. When the V_{cls} is less than the minimum contact line velocity, the target contact angle equals to the receding contact angle from the experimental database. For the locations on the perimeter which do not advance or recede quickly ($V_{clsmin} < V_{cls} < V_{clsmax}$), the target contact angles are interpolated via a sine function in Eq. (14)[107](The associated PHASTA source code is presented in Appendix I.1 and I.2).

$$\theta_{target} = \begin{cases} \theta_{adv} & if\ \ Ca_{cls} > Ca_{cls_{max}} \\ \frac{1}{2}\left[sin\left(\frac{\pi \cdot Ca_{cls}}{2 \cdot Ca_{cls_{max}}}\right)(\theta_{adv} - \theta_{rec}) + (\theta_{adv} + \theta_{rec})\right] & if\ Ca_{cls_{min}} < Ca_{cls} < Ca_{cls_{max}} \\ \theta_{rec} & if\ \ Ca_{cls} < Ca_{cls_{min}} \end{cases} \quad (4\text{-}3)$$

where the capillary number ($Ca = \mu V_{cls}/\sigma$) is introduced to ensure consistency when applying to various fluids/conditions. In this research the properties of water are utilized for model verification. However, the formulation of this target contact angle model does not depend on the characteristics of water, so the author anticipates that this target contact angle model can be applied to other fluids, as well.

The similar criterion of contact line velocities is proposed by Bussmann et al. [61] as part of their contact angle model. The reason to describe the contact angle as a function of contact line velocity or capillary number is related to the residual fluid motion even at equilibrium. When the contact line velocity is zero, there is still a range of possible contact angle values, which is described as contact angle hysteresis. The incorporation of the relationship between the contact angle and the capillary number reduces the influence of these fluctuations on the value of contact

angle and ensures a smooth evolution of contact angle along the contact line. Since the main purpose of the capillary number limitation is to obtain certain tolerance of contact angle at equilibrium, it does not have a specific value but needs to be large enough to allow for some simulation uncertainty in the predicted movement of the contact line.

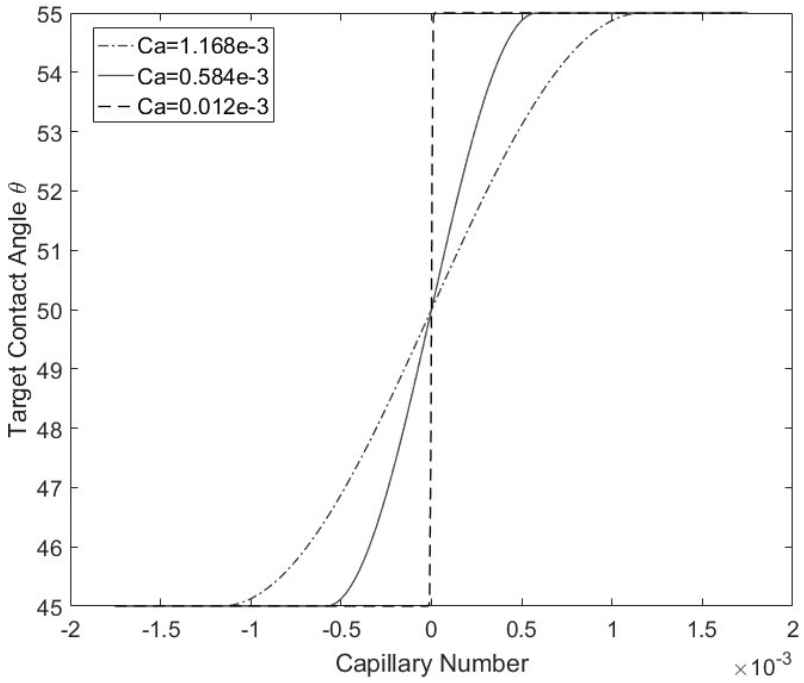

Figure 4.2. The schematic plot of target contact angle function.

The sine function maintains a smooth transient between different capillary number regions, which is important for numerical stability. Assuming $\theta_{adv} = 55°, \theta_{rec} = 45°$, the capillary number varies between -1.752×10^{-3} to 1.752×10^{-3}. For different capillary number limitations (1.168×10^{-3}, 5.84×10^{-4}, 1.168×10^{-5}), the trends of target contact angle are shown in Figure 4.2. In practice, the value of capillary number limitations is adjusted according to the simulated phenomenon, for example, the limitation should be very small (e.g. $\mathrm{Ca} = 1.168 \times 10^{-5}$) for bubble departure in the water pool where the contact line movement is not significant while it should be larger (depends on the movement of the bubble) for bubble sliding

along the wall. The decision-making procedure for contact angle control modeling is illustrated in Figure 4.3 and can be generalized as follows:

1) Calculate the current contact angle and contact line speed for each location on the perimeter;
2) Estimate the target contact angle value using the contact line speed model;
3) Examine if the difference between current contact angle and target contact angle is within the tolerance. When the value is in the tolerance range, the contact angle control force model will not be activated. Otherwise, the contact angle control model will apply the control force on the bubble to adjust the interface;
4) Update the current contact angle and repeat step 3.

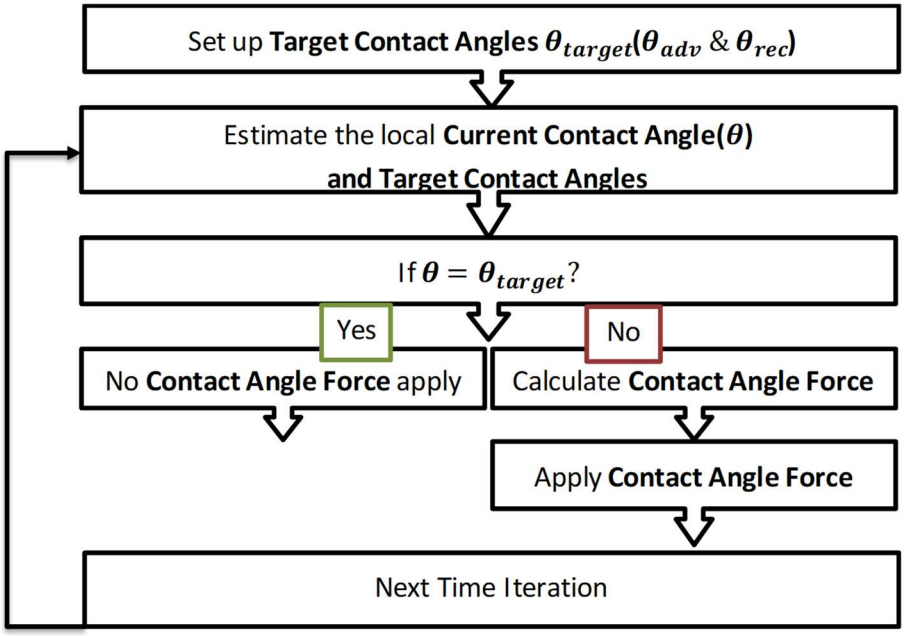

Figure 4.3. The decision-making procedure for contact angle control modeling.

4.3. Contact Angle Control Force Model

Most of the methods to control the contact angle require the modification of the boundary conditions on the wall where the contact line is present. However, this approach is not suitable for LS method, especially on a three-dimensional unstructured grid. To overcome the challenge of

controlling the contact angle only on the contact line in three-dimensional domain, a control force is applied to a certain region defined in the presented model. This control force is only applied when the current contact angle deviates from the desired value (or range of values) and decreases

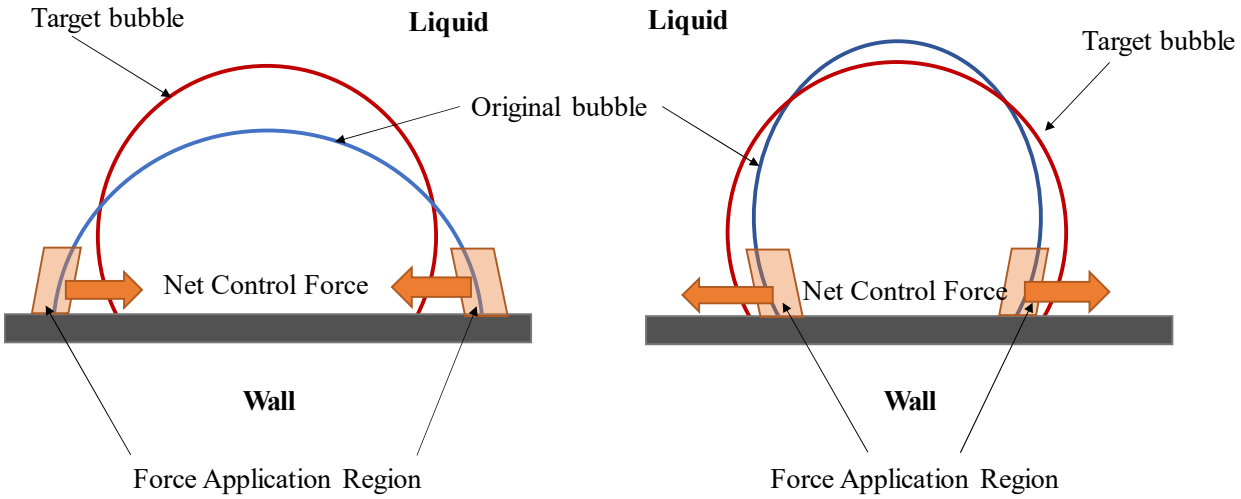

Figure 4.4. The schematic of contact angle control force application.

to zero when the current contact angle reaches the desired value. A spatially varying force is applied to the bubble in the wall-adjacent element shown in Figure 4.4. The expression of the contact angle force is shown below:

$$F_c = F_1 \cos\left(\frac{\Phi}{T} * \frac{\pi}{2}\right) \rho (H - d_{wall})^2 \qquad (4\text{-}4)$$

where Φ is the distance from the interface, d_{wall} is the distance from the wall, H is the height of the contact angle force application region, T is the thickness of the contact angle force application region. There are three components in the contact angle force: the cosine function shows the influence of the distance from the interface; the $(H - d_{wall})^2$ term takes into consideration of the distance from the wall; and F_1 is the parameter which describes the dependence of the contact angle force on the currently observed contact angle. The formulation of F_1 is given as [107],

$$F_1 = \begin{cases} K\left(\frac{1}{2} + \frac{1}{\pi}\left(atan\left(\frac{\Delta\theta - M_{adv}}{S}\right) - Y_{adv}\right)\right) & if\ \Delta\theta \geq \Delta\Theta_{high} \\ K\left(-\frac{1}{2} + \frac{1}{\pi}\left(atan\left(\frac{\Delta\theta - M_{adv}}{S}\right) - Y_{adv}\right)\right) & if\ \Delta\theta \leq \Delta\Theta_{low} \end{cases} \quad (4\text{-}5)$$

where $\Delta\theta$ is the deviation of contact from the target value, $\Delta\Theta_{hig}$ and $\Delta\Theta_{low}$ are the upper and lower bounds of the tolerance, and the model constant $K = 2 \times 10^8, \mathrm{S} = 100$, M_{adv} is the offset of the arc-tangent function along the X axis and Y_{adv} is the offset of the arc-tangent function along the Y axis. The values used in the simulation are chosen to be $M_{adv} = 20, Y_{adv} = 4.449$. These values are selected empirically to ensure that expected contact angle is obtained in a range of verification simulations. The associated PHASTA source code is presented in Appendix I.3.

The shape of F_1 is a modified step function shown in Figure 4.5. When the difference between the current contact angle and target contact angle is within the tolerance, the output of F_1 function is zero. Otherwise, F_1 function produces a positive constant value if the contact angle is larger than the advancing contact angle, and a negative value if it is smaller than the receding contact angle.

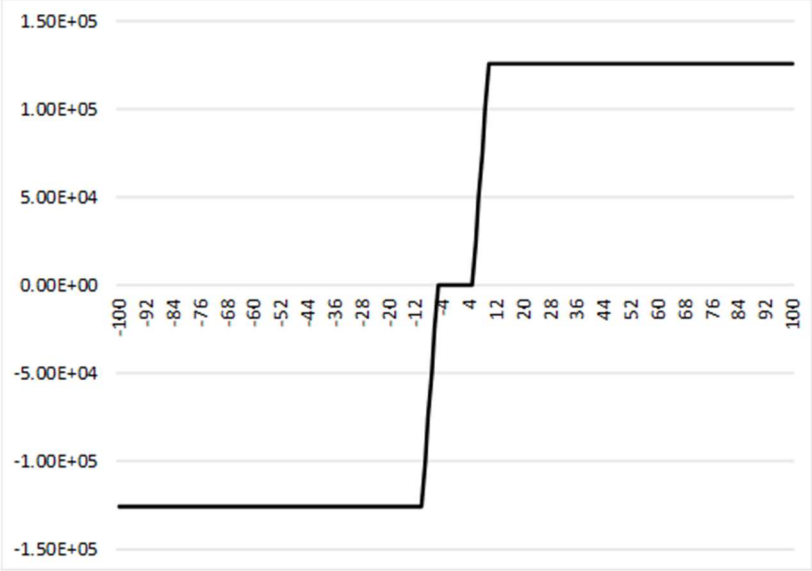

Figure 4.5. The schematic plot of F1 function.

4.4. Analytical Solution of Static Contact Angle

The case of single bubble lift-off from the wall is designed to simulate the evolution of contact angles during bubble departure and verify the value of the static contact angle obtained from the simulation. The force balance analysis of the bubble sitting on the wall is performed to obtain the analytical solution of the static contact angle. The mesh resolution sensitivity study and the parametric study for different target contact angles are performed in this section.

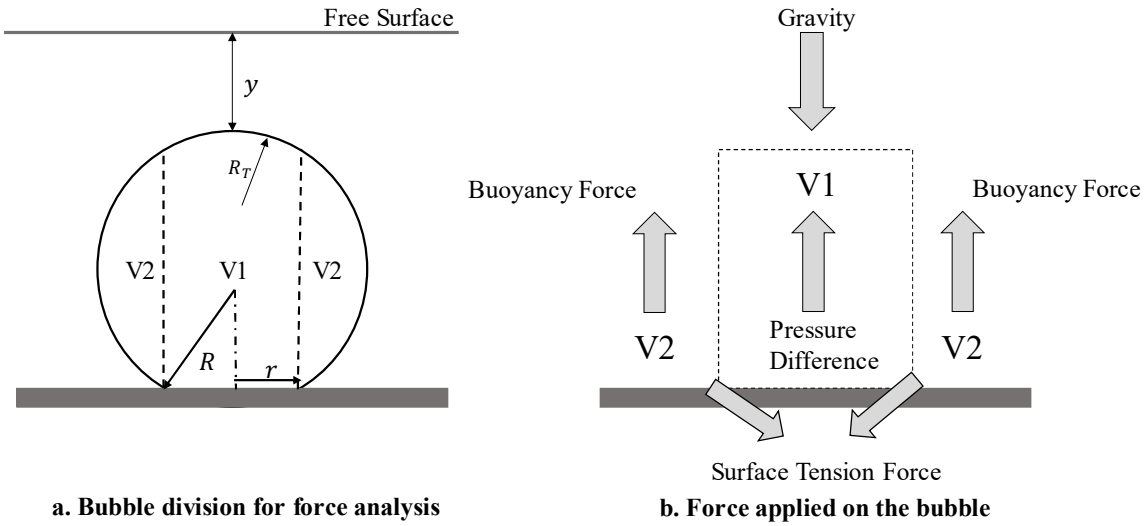

a. Bubble division for force analysis **b. Force applied on the bubble**

Figure 4.6. Force balance analysis for the single bubble on the wall.

Force balance analysis of a single bubble sitting on the wall is performed to calculate the analytical static contact angle. Assuming that the bubble has a spherical shape with a portion cutting off by the ideal wall surface. The bubble is split into two volumes, V1 and V2, as shown in Figure 4.6(a). Pressure difference and gravity are applied to volume V1 while the buoyancy force is applied to volume V2. The surface tension force is applied to the contact line of the bubble. R is the radius of the bubble and r is the radius of the contact line circle. The static contact angle is assumed to be θ. The schematic figure of forces applied on the bubble shown in Figure 4.6(b). The volumes V1 and V2 are calculated as follows:

$$V = V1 + V2 = \frac{4}{3}\pi R^3 - \pi(R - Rcos\theta)\frac{3r^2 + (R - Rcos\theta)^2}{6} \quad (4\text{-}6)$$

$$V1 = \pi(R - Rcos\theta)\frac{3r^2 + (R - Rcos\theta)^2}{6} + \pi r^2 \cdot 2Rcos\theta \quad (4\text{-}7)$$

In this simulation, the advancing contact angle and receding contact angle are the same and equals to static contact angle when the bubble is sitting on the wall because the velocity of bubble interface is zero. The contact line speed is zero at steady state. The buoyancy force balances with the surface tension attachment force in the vertical direction and the pressure acting on the projected area of the bubble apex. The force balance formulation is shown below:

$$-\gamma \cdot 2\pi r\, sin\,\theta + (\rho_l - \rho_g)gV2 + \Delta\pi r^2 = 0 \quad (4\text{-}8)$$

where γ is the surface tension of water, ρ_l is the density of water, ρ_g is the density of air, and g is the gravity. ΔP accounts for the pressure difference across the bubble interface as:

$$\Delta P = \frac{2\sigma}{R_T} - (\rho_l - \rho_g)gy \quad (4\text{-}9)$$

where R_T is the radius of curvature at the tip of the bubble, y is the vertical distance from the bubble apex to the free surface.

Given the radius of the bubble R is 2.0mm, the water and air properties under atmosphere pressure, the analytic contact angles are calculated using Eqs.(4-6), (4-7), (4-8) and (4-9) for various surface tensions. The fluid properties and analytical results are listed in Table 4-1.

Table 4-1: The characteristic of bubble departure case.

Properties	**Water**	**Air**
Density	$996.5\ kg/m^3$	$1.161 kg/m^3$
Dynamic Viscosity	$8.514 \times 10^{-4}\ kg/m \cdot s$	$1.858 \times 10^{-4}\ kg/m \cdot s$
Gravity	$9.8\ m/s^2$, y-direction	
Surface Tension	$0.0729\ N/m$	$0.143\ N/m$
Analytical Critical Contact Angle θ_a	40.06°	30.50°

4.5. Simulation Results of Target Contact Angle

The single bubble is placed on the wall surrounded with a stagnant water. The initial radius of the bubble is 2.0 mm, which is the same radius used in the force balance analysis. The physical properties used in the simulation are shown in Table 4-1. The viscosity of gas phase is higher than physical value of air to increase code robustness. Based on our experience and typical gas properties the increased viscosity is not expected to alter the bubble dynamics. The domain size is

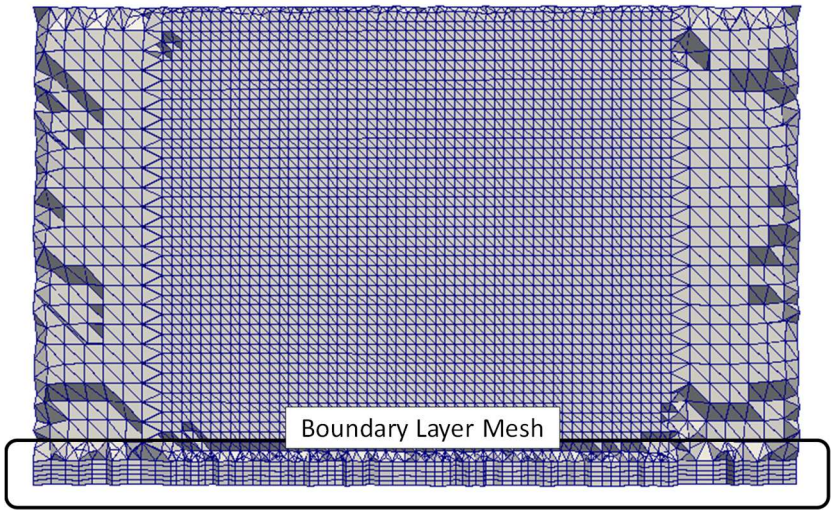

Figure 4.7. The mesh design of bubble departure case.

5mm × 5mm × 8mm represented with unstructured finite-element mesh. The boundary layer mesh is applied in the near wall region shown in Figure 4.7 (Detailed information on prism-shaped boundary layer mesh design is presented in Appendix.C). The periodic boundary condition is applied to the right and the left wall. No-slip boundary condition is applied to the rest walls. The mesh design and the prescribed target contact angle is shown in Table 4-2. Since the bubble in the simulation does not have lateral movement along the surface, the advancing contact angle equals to the receding contact angle as the prescribed target contact angle. The distance to the wall is calculated for the bottom wall in PHASTA, which is utilized in Eq. (4-2) and (4-4) of contact angle control algorithm. According to the force balance analysis presented in the previous section, the bubble departs at certain contact angle if the initial bubble position and surface tension are

given. Therefore, the goal of the simulation is to find out the critical target contact angle that keeps bubble attached to the wall while any other target contact angle that is smaller than this specific value leads to bubble lift off the wall. A series of simulations with different target contact angles are conducted to obtain the critical value for the bubble to lift off and compared with the analytical solution. The mesh resolution sensitivity study is performed for target contact angle and critical contact angle to examine the mesh convergence.

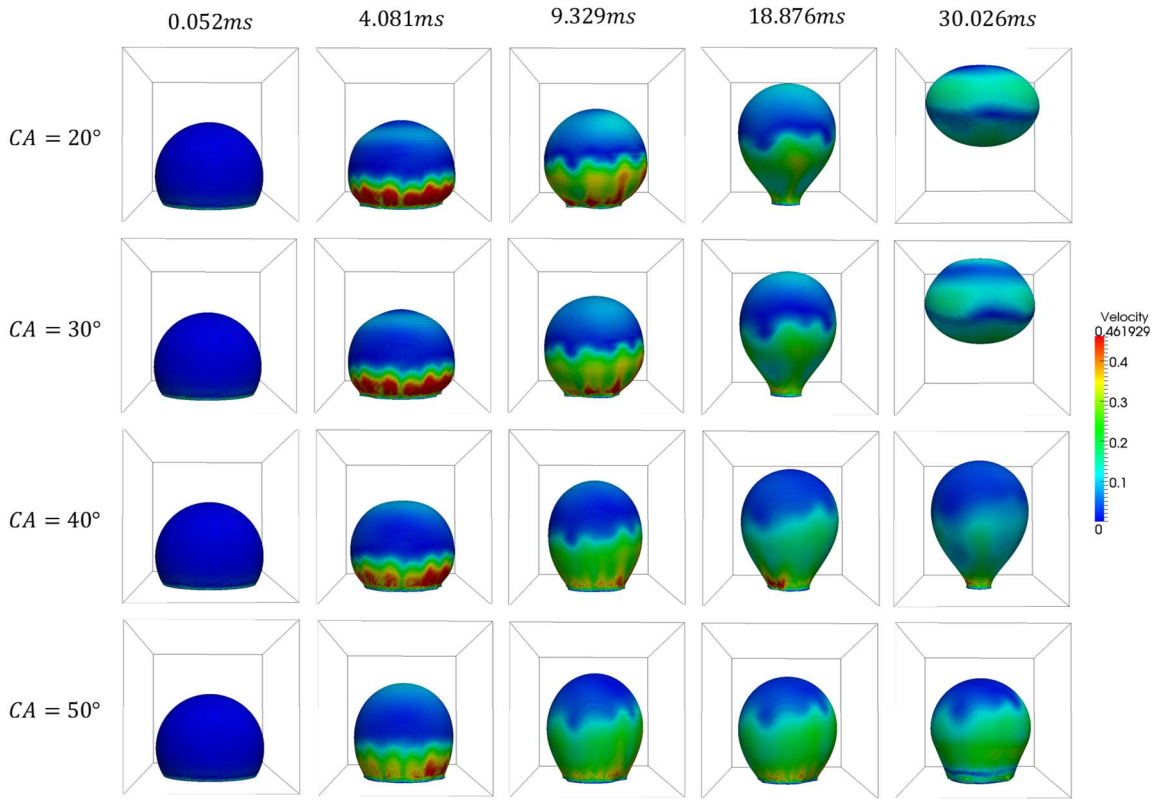

Figure 4.8. The bubble departure process for different target contact angle. The surface tension is equal to 0.0729N/m in the simulations. CA indicates the prescribed target contact angle. The color indicates the velocity magnitude field.

As an important parameter of contact angle control algorithm, the target contact angle is the key value to determine if the bubble is able to depart. In the parametric study of target contact angle, four different target contact angles ($\theta_{target} = 20°, 30°, 40°, \text{and } 50°$) are selected. The mesh size with a bulk resolution of $h = 10^{-4}\ m$ is selected for this parametric study. The initial contact angle maintains the same for all the four cases ($\theta_{\text{initial}} = 60°$). The screenshots

demonstrate the different stages of bubble departure are shown in Figure 4.8. For target contact angle equals to $20°$ and $30°$, the bubble is about to depart at time $= 0.03$s while the bubble remains attached to the wall when the target contact angle is $40°$ or $50°$, which is consistent with the force balance analysis contact angle result of $\theta_{critical} = 40.1°$ for surface tension equal to 0.0729N/m. The bubble contact angle evolution plot is shown in Figure 4.9.

Table 4-2: The case design of single bubble departure.

Domain size	$5\text{ mm} \times 5\text{ mm} \times 8\text{ mm}$
Bubble initial radius	2.00 mm
Initial contact angle	$60°$
Target Contact angles	$20°, 25°, 29°, 30°, 35°, 39°, 40°, 50°, 60°$
Contact line speed limitation	0.001m/s
The model constant K	2×10^8
The model constant S	100
$\mathbf{M_{adv}}$	20
$\mathbf{Y_{adv}}$	4.449
Height of the contact angle force application region	0.12mm
Thickness of the contact angle force application region	0.12mm

4.6. Simulation Results of Critical Contact Angle

From the previous results (Section 4.5), it is found that the bubble remains attached to the wall if $\theta_{target} \geq 40°$. To determine the numerical contact angle from the simulations, a narrow range of the prescribed target contact angle is selected to be $35°, 39°,$ and $40°$. Figure 4.10 shows the contact angle evolution history for different prescribed target contact angle values. The contact angle decreases very quickly in the beginning. When the contact angle is close to the target value, the observed contact angle rate of change slows. The contact angle stabilizes at the target contact angle within the prescribed tolerance range. If the target contact angle is below the critical contact angle according to the analytical solution, the bubble will eventually depart from the wall as observed in Figure 4.10(a) when target contact angle is $35°$ and $39°$. If the target contact angle is above the critical contact angle, the bubble will remain sitting on the wall because the force balance

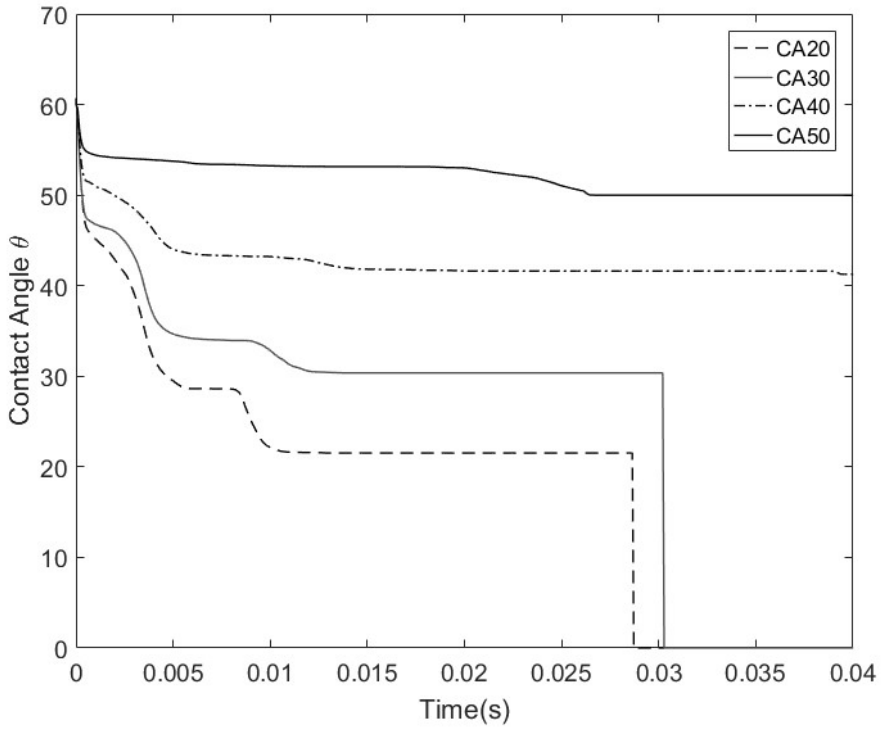

Figure 4.9. The contact angle evolution history for different target contact angles. CA indicates the prescribed target contact angle.

is established between surface tension force, buoyancy force and pressure difference.

To further verify the model, another set of simulations with higher surface tension ($\sigma = 0.143\text{N/m}$) are conducted. The critical contact angle for surface tension equal to 0.143N/m is $30.5°$. The prescribed target contact angle is set to be $25°, 29°,$ and $30°$ to determine the numerical critical contact angle. The similar trend of contact angle evolution is observed in Figure 4.10(b).

The described simulations demonstrate that the contact angle control algorithm is able to maintain correct contact angle when the bubble is sitting on the wall. The contact angle observed in the simulation is compared with the analytical contact angle from force balance analysis for various surface tension and shows good agreement with the reference data.

4.7. Mesh Sensitivity Study

The mesh sensitivity study is first performed with prescribed target contact angles of 39, 40° to examine the code performance with different mesh sizes for various surface tension values. The mesh size in the domain starts with 0.22 million finite elements (0.22M) and increases to 0.72M and 1.47M. The corresponding number of elements across the bubble diameter are 20, 40 and 60, respectively. The model parameters are maintained the same compared with previous simulations. The absolute height and width of control force application region stays the same for different meshes. For the given target contact angle 39°, the bubble is expected to depart into the bulk liquid according to the analytical solution. The surface tension utilized in the simulation is equal to 0.0729N/m (this corresponds to air/water surface tension value at atmosphere conditions). The simulation results shown in Figure 4.10 are consisted with the prediction of the analytical solution. The observed contact angle reduces to zero when the target contact angle is 39.0°, which indicates the moment of the bubble departure from the wall. The bubble lifts off at roughly the same time for fine mesh (0.72M) and finest mesh (1.47M) while the departure time is slightly longer for the coarse mesh (0.22M). It is because the stabilized numerical contact angle

using the coarse mesh has the largest error which makes it closer to the critical contact angle. When the target contact angle is set to be 40.0°, the prediction of the analytical solutions shows that the bubble will not lift off from the wall. The simulation results confirm this conclusion. The observed contact angle in Figure 4.11 are adjusted to the target contact angle values and stabilized at the target contact angle. Again, the error in the stabilized numerical contact angle increases when the mesh is coarser.

The numerical results with uncertainty are reported in Table 4-3 for all three meshes. The model uncertainty shown in the table is from the tolerance of contact angle control algorithm, which is set to be 0.1° in the simulations. The relative errors between the numerical contact angle and prescribed target contact angle listed in Table 4-3 decreases as the total mesh increases. The *Grid Convergence Index* (GCI) [108] is calculated for both target contact angle cases. There is no occurrence of oscillatory convergence observed for both target contact angle values. The apparent order p varies for different target contact angles. The numerical uncertainty in the fine-grid is 2.26% when the prescribed target contact angle is 40° and is 0.085% when the value is 39°.

The mesh sensitivity study is also performed for the critical contact angle in Table 4-4. The critical contact angle is estimated by averaging the contact angle before and after the critical point in the simulations. The model uncertainty of the critical contact angle is calculated using error propagation equation [109]. The GCI [108] is also reported for both critical contact angle cases. The apparent order p is 3.2967 when the critical contact angle $\theta_{critical}$ is 30.5° and is 1.1369 when the critical contact angle $\theta_{critical}$ is 40.1°. The numerical uncertainty is smaller for large surface tension case ($\theta_{critical} = 30.5°$) compared to the water surface tension under atmosphere $\theta_{critical} = 40.1°$.

Table 4-3: The mesh sensitivity study of the target contact angle.

The target contact angle $\theta_{target} = 39.0°$			
	Mesh 1	**Mesh 2**	**Mesh 3**
Total Elements	206,637	722,481	1,474,319
Numerical Contact Angle θ_{num}	$40.7 \pm 0.1°$	$40.6 \pm 0.1°$	$39.2 \pm 0.1°$
Relative error	4.36%	4.10%	0.51%
GCI_{fin}	$GCI_{fin}^{12} = 0.003\%$		$GCI_{fin}^{23} = 0.34\%$
p	3.70		
The target contact angle $\theta_{target} = 40.0°$			
	Mesh 1	**Mesh 2**	**Mesh 3**
Total Elements	206,637	722,481	1,474,319
Numerical Contact Angle θ_{num}	$41.7 \pm 0.1°$	$41.1 \pm 0.1°$	$40.7 \pm 0.1°$
Relative error	4.25%	2.75%	1.75%
GCI_{fin}	$GCI_{fin}^{12} = 1.76\%$		$GCI_{fin}^{23} = 2.46\%$
p	0.5685		
$*Relative\ error = (\theta_{num} - \theta_{target})/\theta_{target}$ *Superscript '12' indicates mesh 1 and mesh 2(similar with '23')			

Table 4-4: The mesh sensitivity study of the critical contact angle.

Surface Tension = 0.0729N/m, **The analytical contact angle** $\theta_a = 40.1°$			
	Mesh 1	**Mesh 2**	**Mesh 3**
Total Elements	206,637	722,481	1,474,319
Numerical Contact Angle θ_{num}	$41.2 \pm 0.07°$	$40.8 \pm 0.07°$	$39.9 \pm 0.07°$
Relative error	2.74%	1.75%	−0.50%
GCI_{fin}	$GCI_{fin}^{12} = 0.39\%$		$GCI_{fin}^{23} = 2.26\%$
p	1.1369		
Surface Tension = 0.143N/m, **The analytical contact angle** $\theta_a = 30.5°$			
	Mesh 1	**Mesh 2**	**Mesh 3**
Total Elements	206,637	722,481	1,474,319
Numerical Contact Angle θ_{num}	$32.9 \pm 0.07°$	$30.8 \pm 0.07°$	$30.6 \pm 0.07°$
Relative error	7.86%	0.98%	0.32%
GCI_{fin}	$GCI_{fin}^{12} = 0.14\%$		$GCI_{fin}^{23} = 0.085\%$
p	3.2967		
$*Relative\ error = (\theta_{num} - \theta_a)/\theta_a$ *Superscript '12' indicates mesh 1 and mesh 2(similar with '23')			

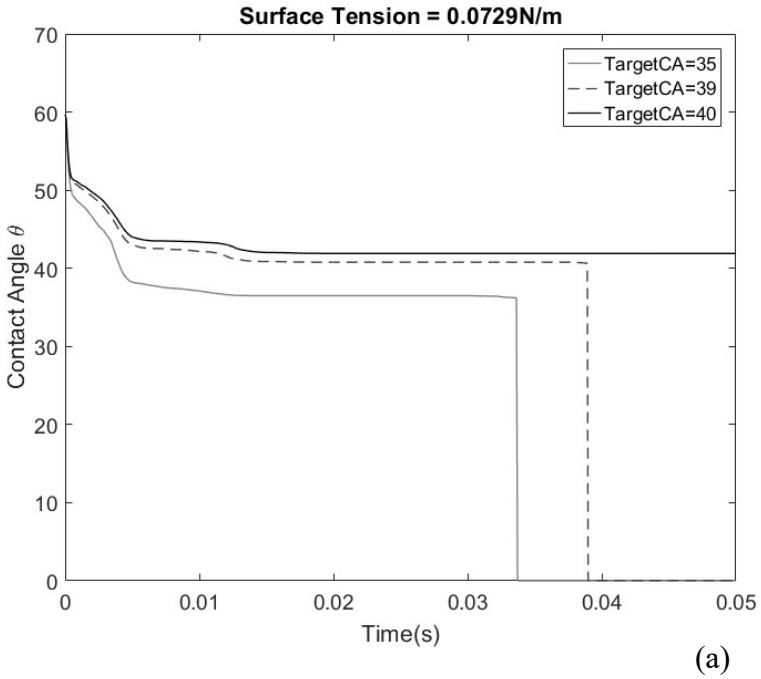

(a)

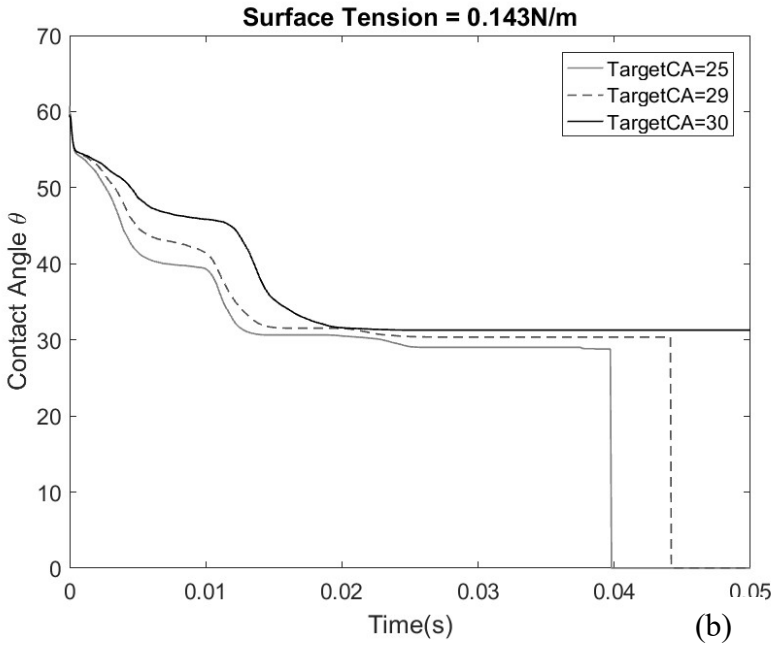

(b)

Figure 4.10. The contact angle evolution for critical contact angle simulation.

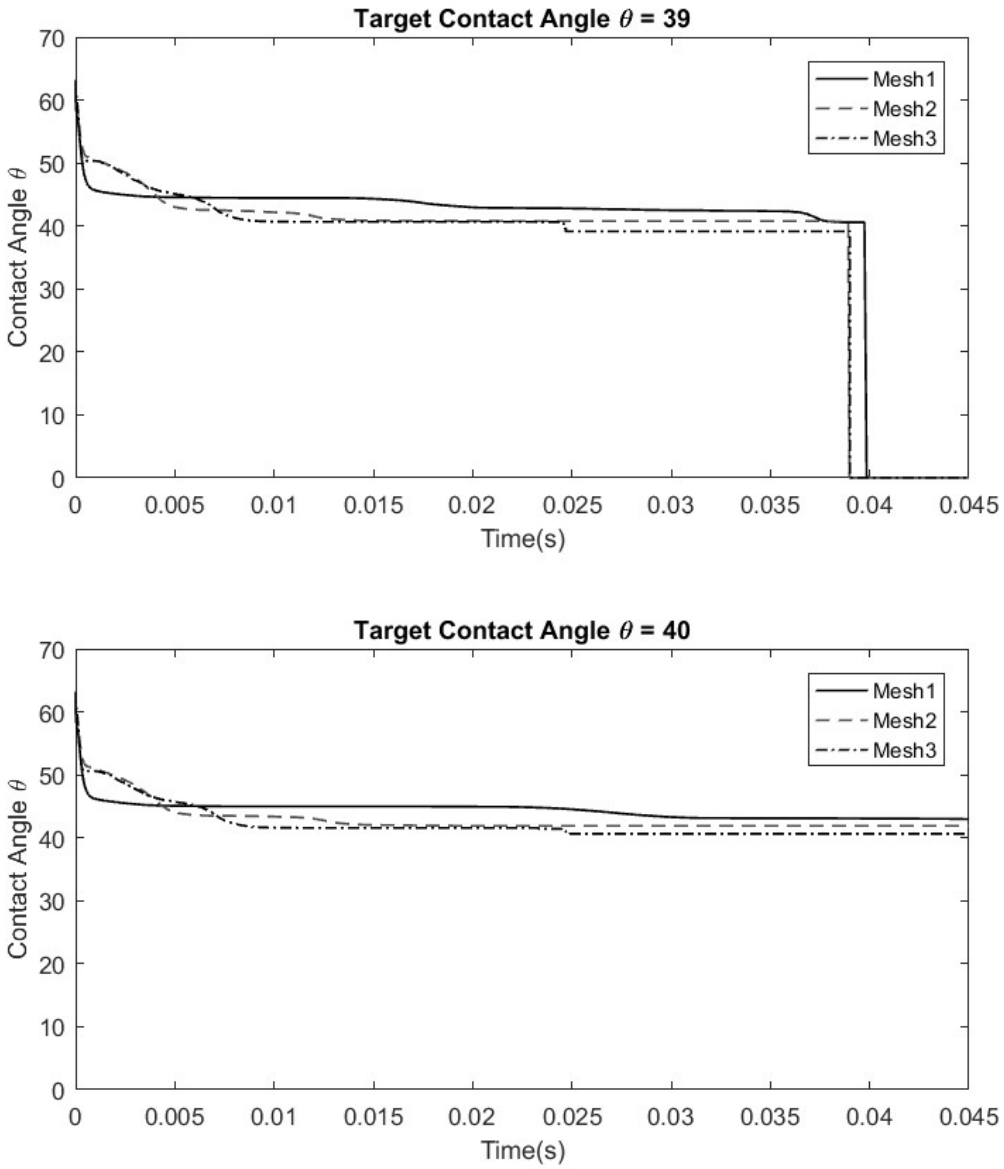

Figure 4.11. The contact angle evolution against time for different meshes.

CHAPTER 5. SIMULATION OF BOILING PHENOMENA

There are six boiling simulation cases under various flow conditions considered in this chapter: 5.1. The single bubble growth with non-uniform temperature distribution: a linear temperature profile with sharp gradient is applied to examine the evaporation and condensation model under gradual change temperature condition. 5.2. Single bubble growth and departure: the single bubble departure from the heated wall examines the coupling between the contact angle control algorithm and evaporation and condensation model. 5.3. Nucleate boiling from a single site: This simulation shows the model potential in investigating boiling mechanism in pool boiling. The bubble departure frequency is extracted from the simulation data and compared with commonly-used experimentally-based correlations. 5.4. The effect of thermal boundary condition in flow boiling simulation: This case is designed to evaluate model performance under various thermal boundary conditions. Both constant temperature and constant heat flux boundary conditions have been applied to the flow boiling simulations and the corresponding temperature distributions are compared. 5.5. The single bubble flow boiling validation: This simulation aims to evaluate the boiling model against experimental results. A side-by-side comparison is performed for the bubble behavior during flow boiling. The bubble departure diameter is selected to quantitatively measure the difference between numerical and experimental results. 5.6. The multi-bubble flow boiling simulation: the flow is heated by the wall with the constant heat flux. This simulation aims to demonstrate the potential of the boiling model in studying local bubble behavior, and possible bubble-bubble interactions in flow boiling scenarios. The bubble dynamics information including bubble trajectory, growth rate, etc. is collected individually for each bubble.

5.1. Single Bubble Growth with Non-uniform Temperature Distribution

In CHAPTER 3, the evaporation and condensation mechanisms have been tested separately in uniformly superheated and subcooled liquid domains, respectively. This demonstration simulation, as a step further, aims to examine the evaporation and condensation model in the same domain with non-uniform temperature distribution. The bubble is initially placed near the heated bottom wall (the bubble on the wall simulation will be discussed in section 5.2). The initial temperature profile is linear with a sharp vertical gradient. The bubble transitions from evaporation to condensation as it flows upward from the superheated bottom wall to the subcooled top wall region due to the buoyancy force effect.

5.1.1. The Case Setup

A small bubble is introduced near the heated wall at the bottom of the domain. The top wall is subcooled at 10℃ (temperature of 90℃) while the bottom wall is superheated at 10℃ (110℃). The initial temperature profile is linearly interpolated between the top wall temperature

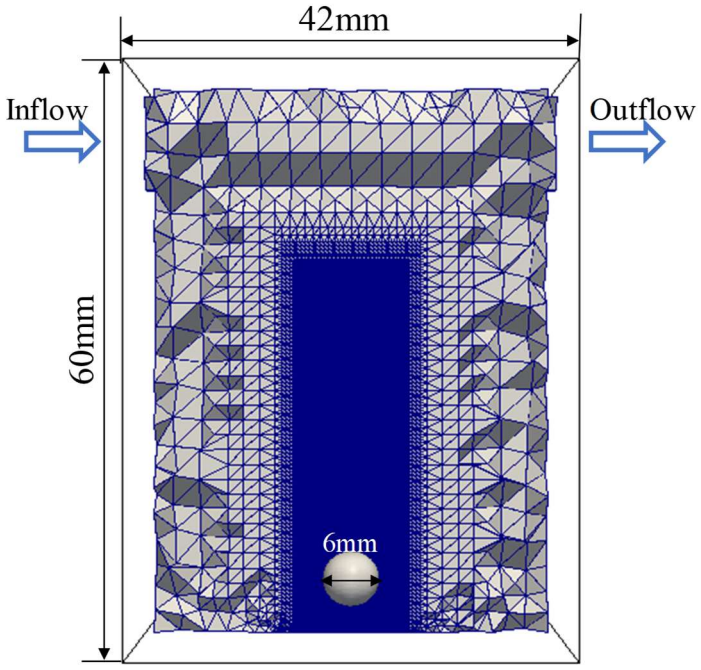

Figure 5.1. The 3D domain and mesh design of single bubble growth with non-uniform temperature distribution.

and bottom wall temperature. The gravity is in the vertical direction of the domain. The inflow/outflow boundary conditions are required to compensate for the volume change during the phase change process due to the significant density difference between vapor and water. A unique inlet/outlet design is created to apply the inflow/outflow boundary condition without backflow issue. The backflow is common issue of CFD solvers for outlet pressure boundaries caused by absence of information available to the solver beyond the boundary. In multi-phase flow simulations, the pressure outflow boundary condition cannot numerically handle two-phase mixture. When the bubble moves across the pressure outflow, the conflict between constant pressure outflow requirement and surface tension force resulting in different pressures inside the bubble causes the divergence of the simulation. So, two specially designed 'vents' are introduced to the top region of the domain in Figure 5.1 to avoid the possible occurrence of the backflow. The constant velocity inlet boundary condition is applied to the left vent while the natural pressure outlet boundary is applied to the right one. The simulations were carried out using 5 million tetrahedral elements and utilized 128 processing cores on local cluster (2 computing nodes with four 16-core Opteron processors each). The local refinement is applied to the region of anticipated bubble trajectory shown in Figure 5.1 (Detailed discussion of mesh adaptivity can be found in Appendix.A). The bubble transition from evaporation to condensation occurs as it flows upward to the subcooled region near the top wall.

5.1.2. Results and Analysis

A small bubble is introduced near the heated bottom wall. While flowing through the 3D domain, the bubble grows/shrinks due to the estimated average temperature gradient at the interface. The snapshots of the temperature and velocity distribution during evaporation and condensation process are shown in Figure 5.2. The vapor temperature inside the bubble is fixed at saturated temperature under atmospheric pressure conditions. The liquid superheat is the difference between the temperature profile at each time steps and the saturation temperature. The thermal boundary layer is developing around the interface. As the bubble moves through the domain, the cool liquid on top flows to fill up the space formerly occupied by the bubble and mixes with the hot liquid in the lower region. The evolution of the bubble volume is presented in Figure

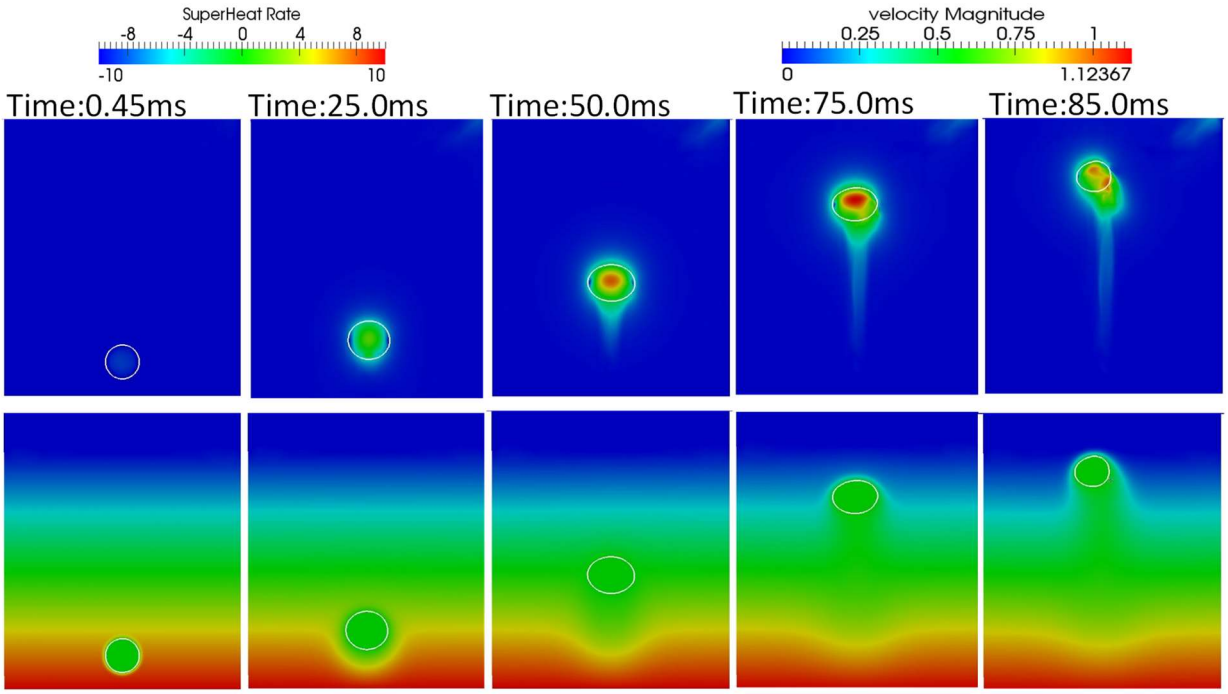

Figure 5.2. The evaporation and condensation snapshots (colored by the superheat field in first column while velocity in second one).

5.3. The numerical bubble size increases in the super heat region for the first 25ms, stablizes in the staturated region and decreases when it reaches the subcooled region on the top.

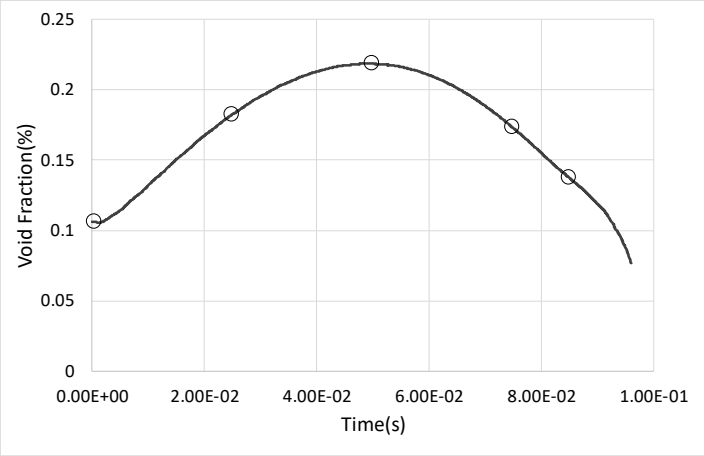

Figure 5.3. The void fraction plot based on time step during bubble growth with non-uniform temperature distribution (The circle indicates the data point of the snapshots in Figure 5.2).

5.2. Single Bubble Growth and Departure

The evaporation and condensation model (CHAPTER 3) and the contact angle control algorithm (CHAPTER 4) have both been implemented in PHASTA and verified against the corresponding analytical solutions. The transient process of bubble growth and departure is simulated in 3D domain using unstructured mesh to examine the coupling between the contact angle control algorithm and evaporation and condensation model. Different from the boiling simulation in Section 5.1, a small vapor bubble is initialized being attached to the heated bottom wall of the domain. The bubble is anticipated to grow according to the local temperature distribution and lift off due to the force balance among the surface tension force, buoyance force and the pressure acting on the projected area of the bubble apex. The mesh sensitivity verification study is performed to evaluate the model performance with different element sizes.

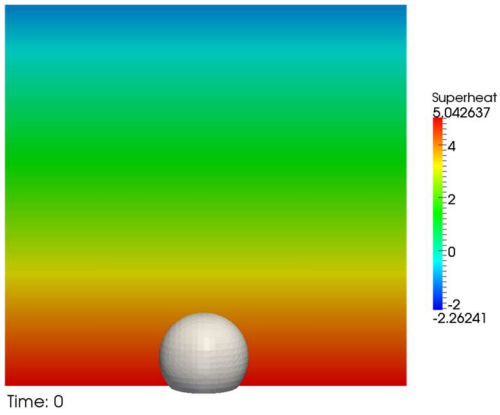

Figure 5.4. The initial temperature condition of single bubble growth and departure simulation.

5.2.1. The Case Setup

The initial diameter of the small vapor bubble on the bottom wall is 1 mm. The vapor temperature inside the bubble is fixed to be the saturated temperature (100℃ under atmospheric pressure), which is consistent with the assumption of evaporation and condensation model. The bottom wall is heated with constant heat flux ($1000\ W/m^2$) while the top wall is maintained at constant temperature of 97℃ (three degree subcooling). The initial temperature profile is linearly

interpolated using the top wall temperature and bottom wall temperature gradient. The conduction in the liquid relates the temperature gradient to the heat flux boundary condition at the bottom wall. The intercept of the linear function is calculated using the top wall temperature. The gravity is applied in the vertical direction of the 3D domain. The volume change due to the significant density difference between vapor and water is compensated using inflow boundary condition on the side walls (group A in Figure 5.5) and natural pressure boundary condition on the top wall. The periodic boundary condition is applied to the other side walls (group B in Figure 5.5). The prism-shaped boundary layer elements are applied to the near wall region for accurate estimation of local contact angle as shown in Figure 5.6 (Appendix.C). The region of interest is refined several times as shown in Figure 5.5. The bubble can always be resolved with high-resolution at relatively low computational cost for each stage of the simulation because of the local refinement capability (Appendix.A). The total mesh size is about 1.8 million tetrahedral elements (including three layers of prism-shaped boundary layer elements), which requires 128 processing cores on local

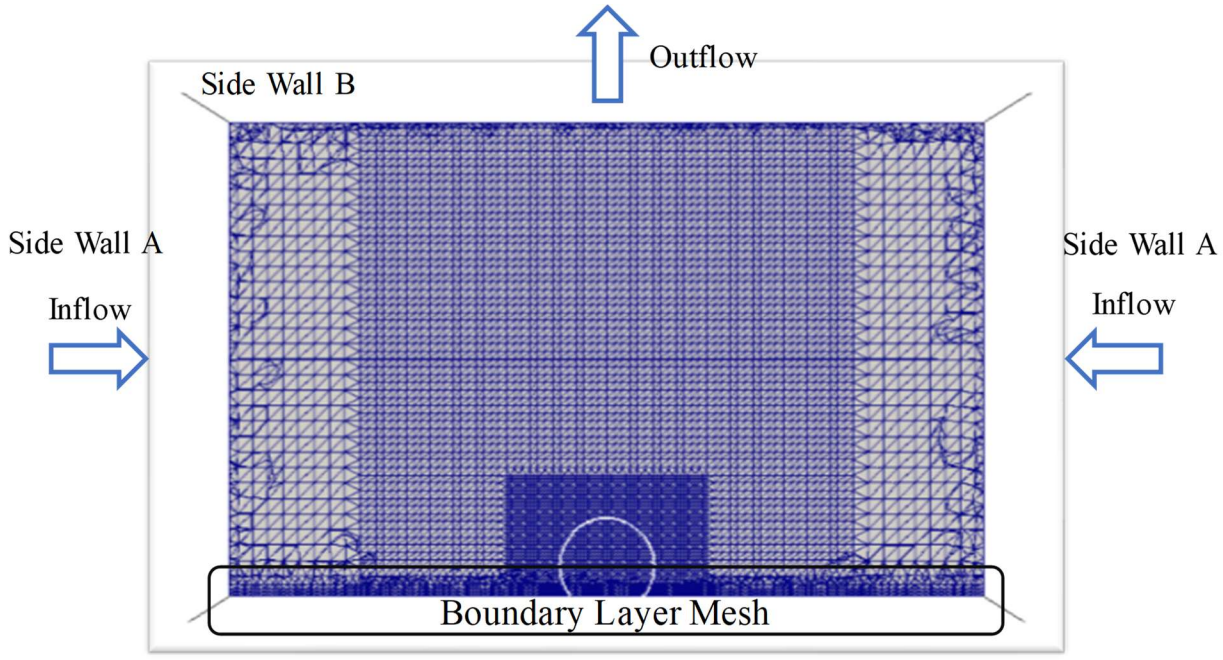

Figure 5.5. The mesh design and boundary condition of single bubble growth and departure simulation.

computing cluster. The case setup of single bubble growth and departure simulation is summarized in Table 5-1 below.

Table 5-1: The case design of the single bubble growth and departure simulation.

Geometry	
Domain size	$5 \times 5 \times 6$mm
Initial radius	0.5mm
Number of elements in the computational grid	1,788,120
Elements across diameter	25
Boundary conditions	
Bottom wall	Non-slip, 1000 W/m^2
Inside bubble	100℃
Top Wall	Natural Pressure, 97℃
Side Wall A	10^{-6} m/s , inflow direction
Side Wall B	Periodic
Initial conditions	
Temperature	Fully Developed Temperature Field
Model Parameters	
Target contact angle	30°
Contact angle force application region	Height: 0.07mm
	Thickness: 0.07mm

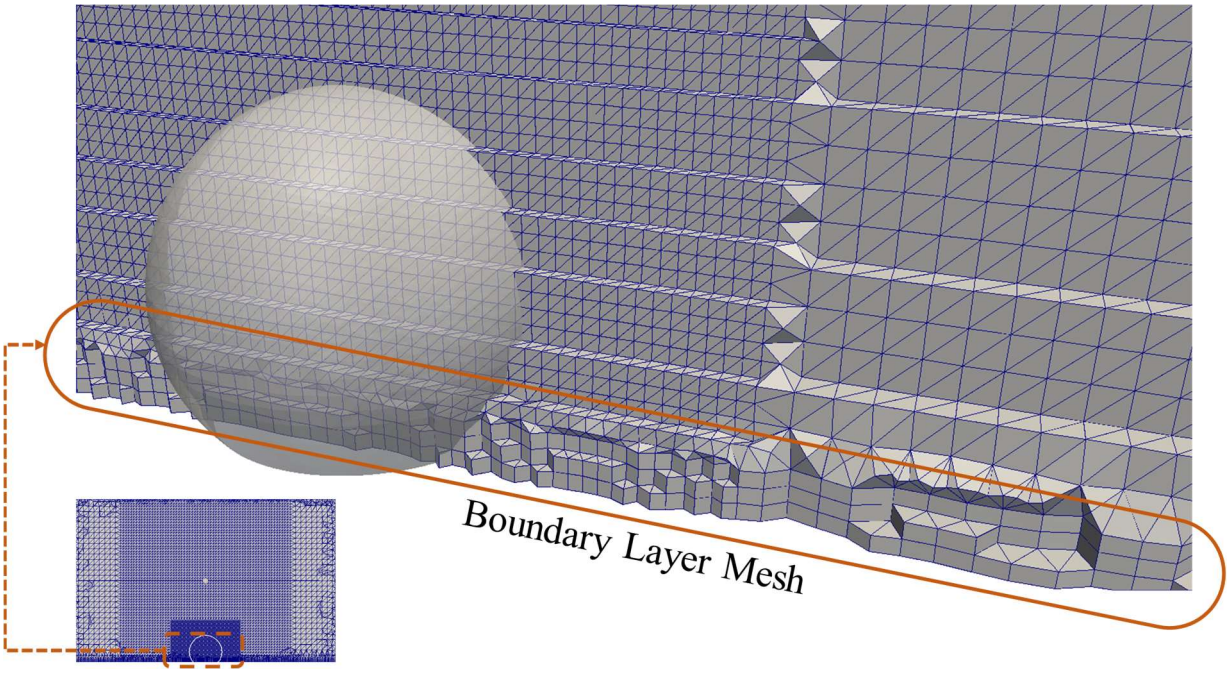

Figure 5.6. The 3D zoomed figure of the boundary layer mesh in the pool boiling simulation.

5.2.2. Results and Analysis

The transient simulation of a bubble growth and departure from the wall is conducted in the 3D domain with heated bottom wall. The liquid superheat is estimated using the temperature profile at each time steps minus the saturation temperature. The velocity and temperature distribution during bubble departure from the wall are shown in Figure 5.7. There is a region of higher local velocity near the local contact line (the triple contact line between solid, liquid and gas phase), which indicates the movement of the interface due to contact angle control force application. The local superheat results in the temperature gradient around the bubble. The evaporation and condensation model collects and averages the local temperature gradient data, and then computes the volume of generated vapor from the evaporation heat transfer. When the bubble is sitting on the wall, the force balance is mainly between the buoyancy force and the surface

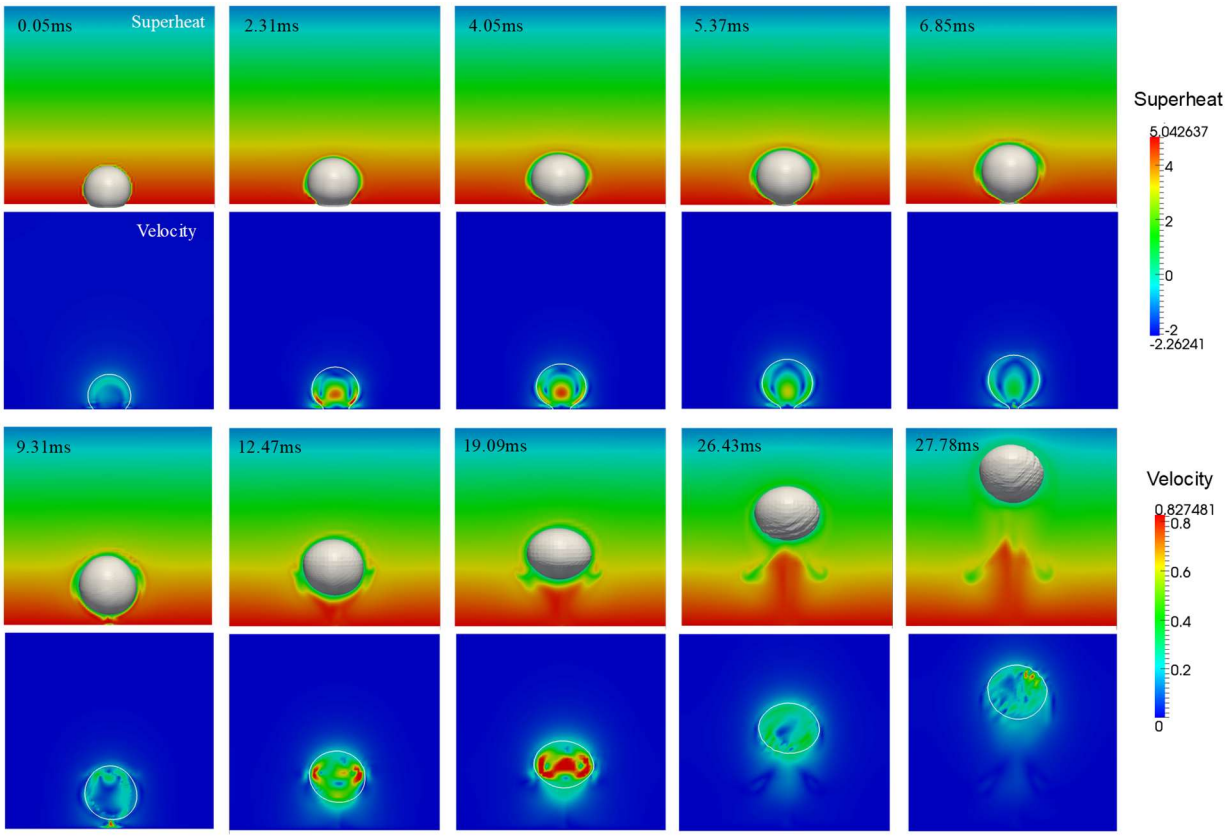

Figure 5.7. The simulated evolution of bubble growth and departure from the wall (The temperature distribution is shown in row one and row three while the velocity distribution is shown in row two and row four with interface contour).

tension force. As the bubble grows, the buoyancy force increases. The departure of the bubble occurs when the buoyancy force exceeds the surface tension force which attaches the bubble to the wall. As the bubble moves through the domain, the quenching effect is observed in the wake region of the bubble, where the cool liquid mixes with the superheat liquid in the lower region.

Mesh sensitivity study is performed to examine the model performance with different element sizes. For every refinement of the domain, the element size of the neighboring refinement region is increased by a factor of two, for example, the element size of the finest refinement region is 0.04mm (25 elements across the bubble diameter), so the element size of the refinement region surrounding the finest one should be 0.08mm . The total mesh in the domain starts with 0.58 million unstructured elements (0.58M) and increases to 0.94M and 1.79M. The bubble is resolved with 16, 20 and 25 elements across the diameter accordingly. The case setup is maintained the same as listed in Table 5-1 for all three simulations. The absolute height and width of the contact angle control force application region stays the same for different meshes as well as the target contact angle. The surface tension utilized in the simulation is equal to 0.0729 N/m (typical value for atmosphere conditions). The evolution of the bubble equivalent radius (computed from bubble volume and converted to radius assuming spherical shape) over time is presented in Figure 5.9 for different meshes. The numerical growth rate for all three meshes is consistent. The equivalent radius increases fast in the superheat region and stabilizes when the bubble reaches the saturated

Figure 5.8. The mesh design of single bubble growth and departure simulation for the mesh sensitivity study (The bubble is represented by the white contour.).

region. The gradient changes at around 14ms results from the quenching effect that the cooler liquid mixes with the superheat liquid as the bubble moves upward. The grid convergence index [108] is calculated using the bubble equivalent radius for quantitatively comparison (Table 5-2). The apparent order p for bubble growth and departure simulation is 6.88. The GCI value is much smaller than 1. The numerical results converges to a stable solution and stay independent of element size as the mesh becomes finer. The conclusion from this single bubble growth and departure provides guidance for the mesh design of future large scale boiling simulations.

Table 5-2: The GCI calculation of single bubble growth and departure simulation.

ϕ = the numerical bubble departure radius(m)		
ϕ_1	ϕ_2	ϕ_3
6.192×10^{-4}	6.189×10^{-4}	6.199×10^{-4}
Parameter	Mesh 1,2	Mesh 2,3
The refinement factor	r_{12}: 1.63	r_{23}: 1.9
The extrapolated value	6.189×10^{-4}	6.199×10^{-4}
Grid convergence index	GCI_{12}: 0.0021%	GCI_{23}: 0.0024%
The apparent order	p = 6.8824	

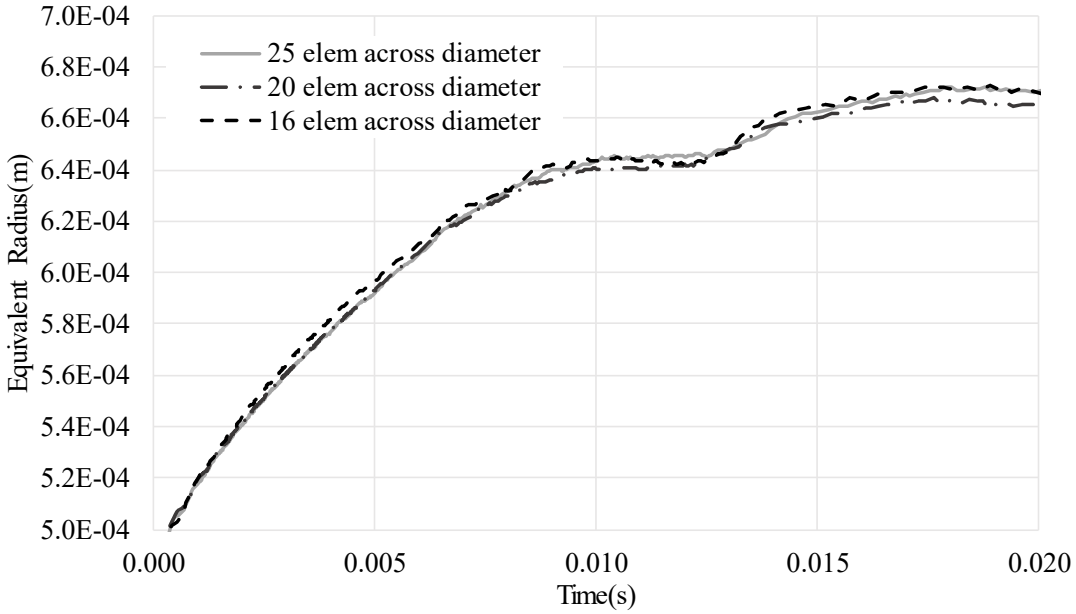

Figure 5.9. The evolution of bubble equivalent radius over time for different meshes.

5.3. Nucleate Boiling from Single Site

This simulation shows the model potential in investigating nucleate boiling mechanism in pool boiling. The evaporation and condensation model, contact control algorithm, bubble tracking algorithm and bubble break-up detection are activated in this nucleate boiling simulation. Successive bubbles grows from a single nucleation site and the bubble release frequency is estimated using the simulation data. The numerical bubble release frequency is compared with commonly-used experimentally-based correlations. The error analysis and possible approaches to improve the boiling model are also discussed in this section. The associated PHASTA source code is presented in Appendix.J.

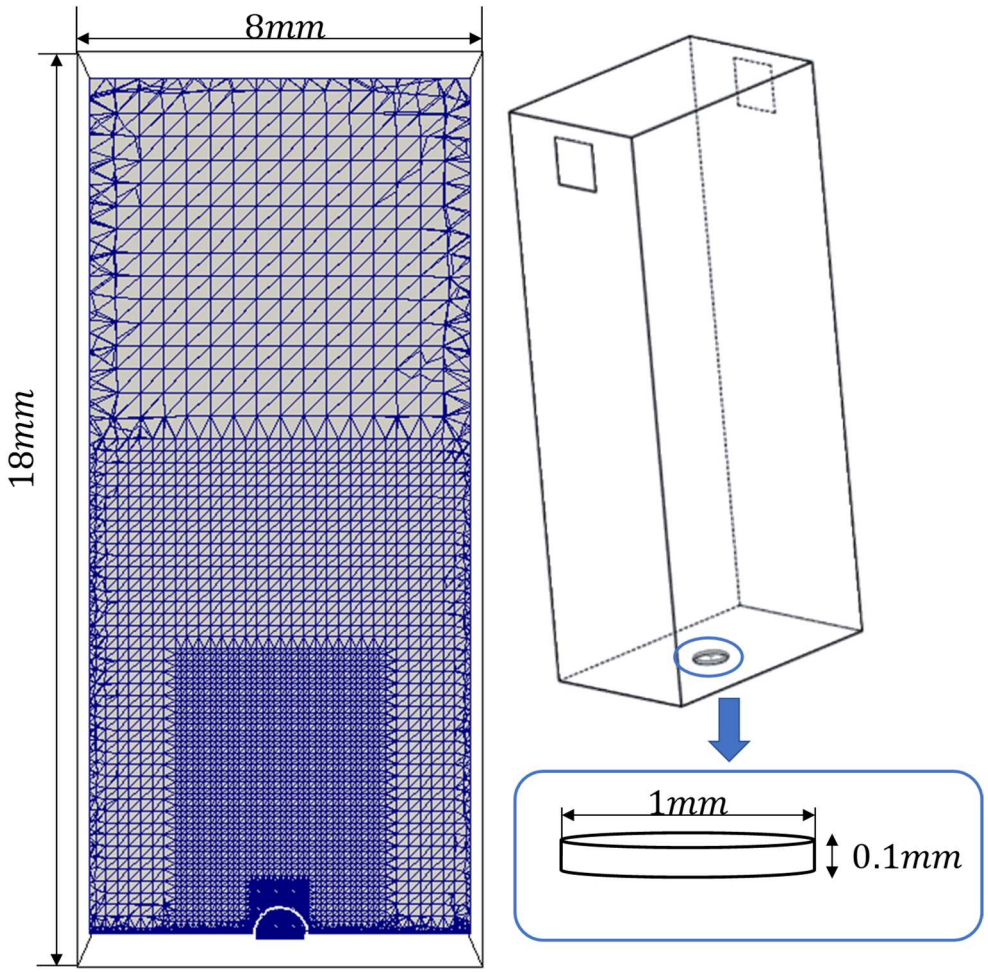

Figure 5.10. The mesh design of the domain and the schematic of the domain with the artificial nucleation site.

5.3.1. The Case Setup

In the nucleate boiling simulation, the domain design shown in Figure 5.10 is similar to the one used in single bubble growth with non-uniform temperature distribution simulation (Section 5.1). A small cavity is placed on the bottom wall of the domain as an initial nucleation site. A small vapor bubble ($r = 0.56$ mm) is introduced to the same location as the nucleation site ($D = 1.0$ mm). The simulations are carried out using 0.7 million unstructured elements and utilize 192 processing cores on the local cluster. The local refinement (Appendix.A) is applied to the region of interest shown in Figure 5.11. The finest mesh region (Region 1) around the bubble ensures sufficient mesh resolution to resolve the bubble shape and the interface accurately (25 elements across the bubble diameter). As the bubble grows and departs from the wall, it moves upward to the second refinement region (region 2). The bubble size is larger in region 2 than region 1 because of the evaporation. Therefore, the slightly coarser mesh is sufficient to maintain the number of elements across larger, departed bubble diameter. Moreover, the ratio of element size between the

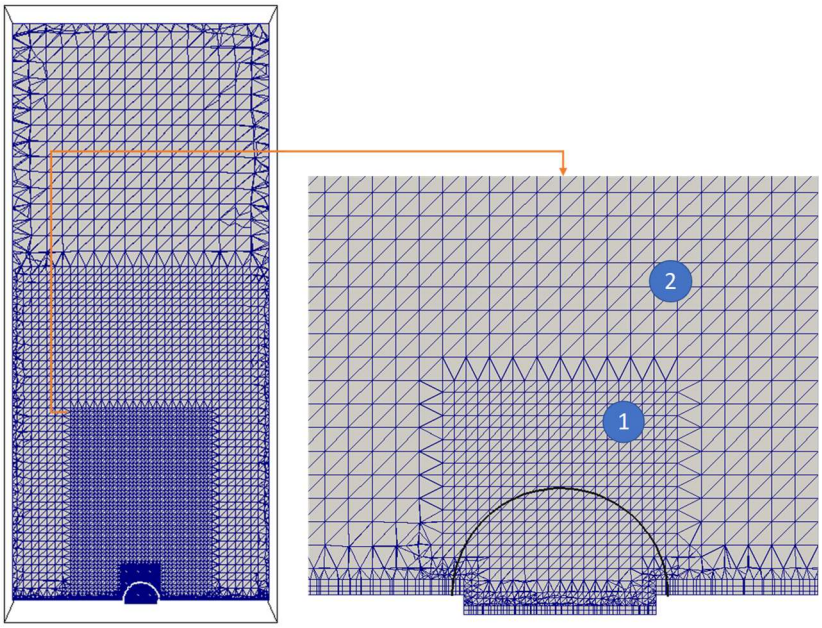

Figure 5.11. The local refinement applied in the vicinity of the bubble.

neighboring refinement regions is no larger than two to avoid numerical instability in the

simulation except for the coarsest region which is far away from the region of interest. The prism boundary layer mesh (Appendix.C) is applied in the near wall region to capture the sharp temperature gradient as well as to obtain accurate wall normal vector direction and magnitude for the contact angle sub-grid model. There are three layers in the boundary layer mesh. The top level element size of the boundary layer is equal to the element size of the adjacent bulk refinement mesh region. The boundary layer mesh is parallel to the wall. Therefore, the vertical height of the local element can represent the wall normal in the simulation. The contact angle of the bubble is estimated and controlled using the contact angle control algorithm (CHAPTER 4). A very small initial velocity is applied for numerical stability. The same initial velocity ($V_{inital} = 1.0 \times 10^{-4} m/s$) has been used in the single bubble verification study [110] which shows that a small enough initial velocity will not affect the bubble growth rate. The detailed information of simulation case setup is summarized in Table 5-3.

The unique 'vents' design are introduced to the top region of the domain to compensate the volume change due to significate density difference and avoid the possible occurrence of backflow. The constant velocity inlet boundary condition is applied to the left vent while the natural pressure outlet boundary is applied to the right one. The initial temperature of the domain is set to be saturated. The constant heat flux boundary condition is applied to the bottom wall. The gravity is applied in the vertical direction of the domain.

Table 5-3: The case design of pool boiling single bubble simulation.

Geometry	
Domain size	$18 \times 8 \times 5\text{mm}$
Initial radius	0.56mm
Number of elements in the computational grid	715,632
Elements across diameter	28
Boundary conditions	
Bottom wall	$50\ \text{W/m}^2$
Top wall	90℃
Inside bubble	100℃
Initial conditions	
Temperature	Fully developed linear profile
Velocity	$1.0 \times 10^{-4}\text{m/s}$

5.3.2. Results and Analysis

The simulation results of nucleate boiling from a single site are presented in this section. Two successive bubbles depart from the pre-defined nucleation site on the bottom wall (Another nucleate boiling simulation of three bubble departure in sequence is presented in Appendix.E). The series of snap shots show the bubble movement (Figure 5.12) and the bubble ID field (Figure 5.13). The thermal boundary layer can be seen developing around the bubble interface. The bubble growth is observed while it sits on the heated wall (up to 28 ms). As the bubble size increase, the departure occurs for the buoyancy force exceeds the surface tension force and the quenching effect is observed in the wake region of the bubble (at 30 ms). After the first bubble lifts off from the wall, a small portion of vapor is trapped in the nucleation site and serves as a nucleation seed for the second bubble. It is noted that the bubble growth time and waiting time is naturally determined by the force balance and heat transfer mechanisms explicitly resolved in the simulation. With the boiling model presented, no additional parameters are required for the nucleating process. As the first bubble departs from the wall, the new bubble is quickly identified by BTA (Section 2.6) shown in Figure 5.13. The bubble ID of the first bubble increases to 'ID 2' while the new bubble is applied with the 'ID 1'. The average local temperature gradient is collected for each bubble according to their bubble ID. As the second bubble departs, a seed bubble is left on the nucleation site and starts to nucleate. The second bubble has a small velocity lifting off from the wall. As the bubbles grow, the bubble-bubble interaction is observed in the simulation. Due to the large growth rate of the third bubble, these two bubbles eventually merge back to one bubble. The bubble behaviors in the nucleate boiling simulation are consistent with the observed nucleate boiling phenomenon.

The numerical bubble release frequency is estimated and compared with the commonly-used experimentally-based correlations for validation purpose. The average bubble departure time extracted from the simulation is utilized to compute the numerical bubble release frequency. The

theoretical models from Zuber (Eq.(1-18)), Jakob & Fritz (Eq. (1-19)), and Cole (Eq. (1-20)) are selected as the reference data shown in Figure 5.14. The simulation result is consistent with the prediction of the theoretical models. The relative errors between the numerical result and each correlation's prediction are listed in Table 5-4. For the same bubble departure diameter, the Cole's correlation has lower release frequency prediction value for small bubble and larger prediction value for the relatively large bubble compared to Zuber's and Jakob & Fritz's correlation. The simulation results have the least relative error compared to Zuber's correlation and the largest one when compared with Cole's correlation. As observed in Figure 5.14, the prediction difference on the bubble release frequency between various theoretical models is significant. Considering this variance in theoretical model predictions, we can conclude that the numerical bubble release frequency is comparable to the commonly-used experimentally-based correlations.

The nucleate boiling simulation demonstrates that the boiling model in PHASTA has the ability to predict bubble release frequency without introducing new sub-grid models. This is a novel approach that has never been applied in 3D high resolution boiling simulation with unstructured mesh. To fully validate the boiling model on nucleate boiling capability, simulation under various heating conditions could be conducted and compared with the commonly-used experimentally-based correlations. The comparison with available experimental data is also recommended as part of the model validation in the future work

Table 5-4: The relative error compared with the theoretical models.

Bubble frequency model	Theoretical frequency (1/s)	Numerical frequency (1/s)	Relative error
Zuber[111]	28.7166	40.443	0.2900
Jakob & Fritz[51]	24.1679		0.4024
Cole[45]	63.6096		0.5728
Relative error $\varepsilon = \frac{\lvert f_{num} - f_{ref} \rvert}{f_{ref}}$			

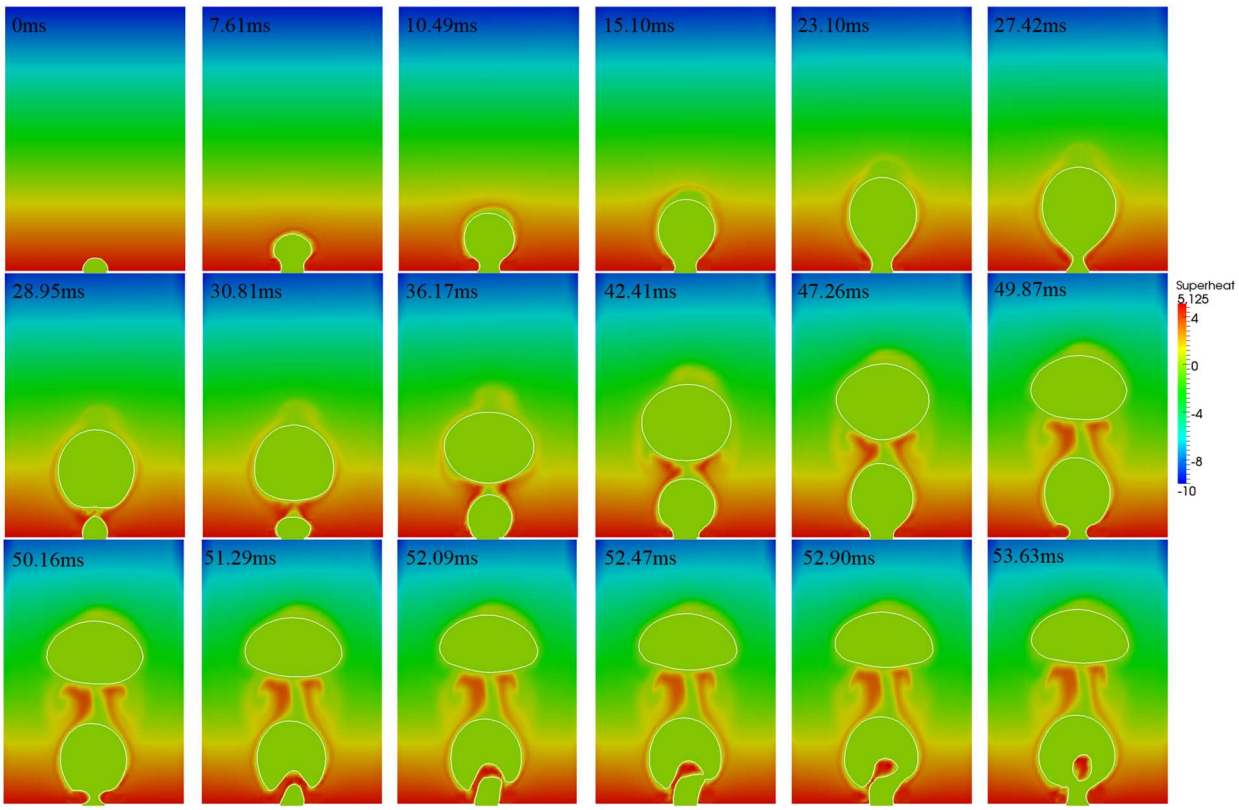

Figure 5.12. The snapshots of bubble nucleating process. The background color indicates the temperature distribution.

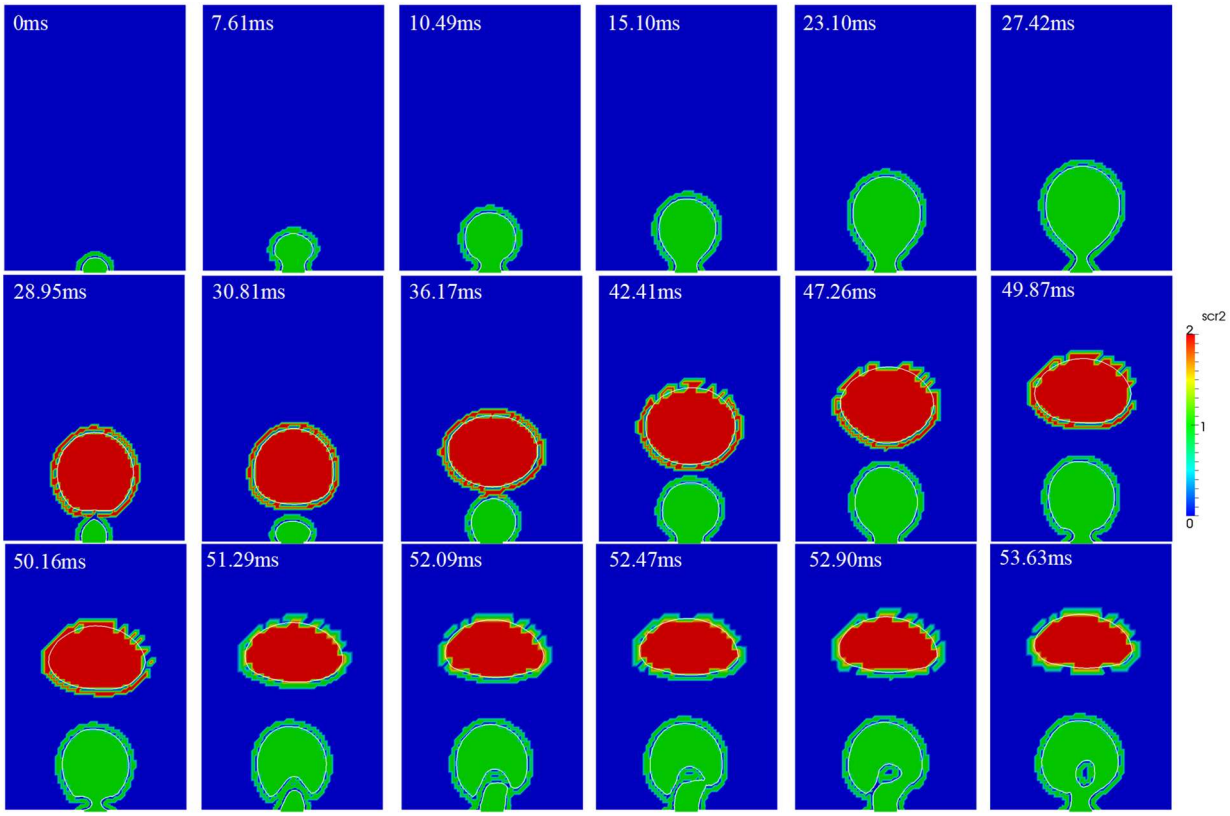

Figure 5.13. The evolution of bubbles nucleating from a single site. The background color indicates the bubble ID field in BTA.

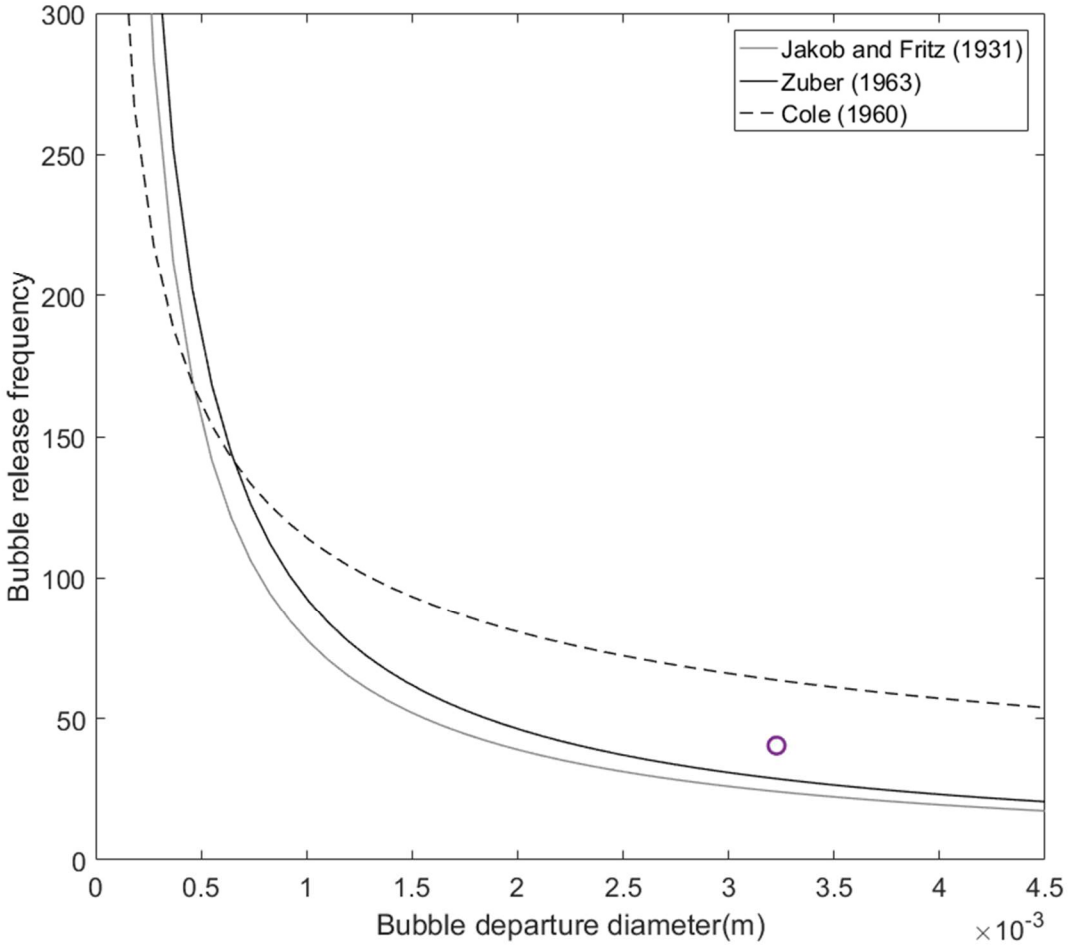

Figure 5.14. The comparison between the numerical result and the commonly-used experimentally-based correlations.

5.4. The effect of thermal boundary condition in flow boiling simulation

PHASTA have not been traditionally used to solve multi-phase heat transfer problems, so the thermal boundary conditions have not been tested in two-phase heat transfer simulations. This test case evaluates the model performance under various thermal boundary conditions (The associated PHASTA source code is presented in Appendix H.5). Both constant temperature and constant heat flux boundary conditions have been applied to the bottom wall of the domain. The effect of thermal boundary condition on the temperature distribution and bubble growth is discussed. The overall behavior is close to the observation of boiling phenomena. The single bubble flow boiling simulation demonstrates the boiling model is not only able to conduct pool boiling simulations, but also convective flow boiling simulations.

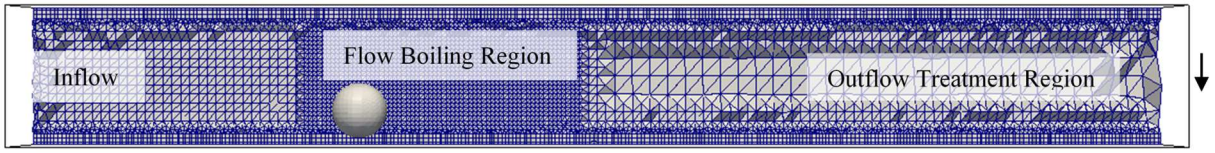

Figure 5.15. The mesh design for the flow boiling simulation.

5.4.1. The Case Setup

In the flow boiling simulations, the domain size is $4.14\text{mm} \times 0.5\text{mm} \times 0.5\text{mm}$. The simulation is carried out on 859,214 tetrahedralized elements and utilized 128 processing cores on local computing cluster. The local refinement is applied to fulfill the resolution requirement of the flow boiling simulation meanwhile reduce the computational cost as much as possible (Appendix.A). The domain is divided into three refinement regions shown in Figure 5.15. The finest region is designed to resolve the required temperature gradients around the bubble, the bubble shape and the interface accurately (25 elements across bubble diameter). The mesh resolution in the inflow region ensures that the laminar velocity profile is fully resolved. The coarse mesh in the outflow treatment region and a heat sink approach allow the under-resolved bubble to

condense before it reaches the outflow boundary for the pressure outflow boundary condition cannot numerically handle two-phase mixture. The prism boundary layer mesh (Appendix.C) is applied to accurately resolve the thermodynamics and hydrodynamics boundary layer profile. The flow channel is horizontal, and the gravity is in the vertical direction. The bottom wall is superheat with constant temperature or constant heat flux condition while the top wall is subcooled having temperature of 91℃. The vapor inside the bubble forced to be saturated during the simulation. The thermal boundary condition of the bottom wall is the only control variable while all the other settings stay the same. The temperature distribution around the bubble and the numerical growth rate are selected features to reveal the effect of various boundary condition in flow boiling simulations.

5.4.2. Results and Analysis

In the two flow boiling simulations presented here, different boundary conditions have been applied to the bottom wall: Constant temperature at 110℃ (10℃ superheat) and a constant heat flux of 446.16 W/m^2, which is estimated based on the mean temperature, laminar flow Nusselt number (Appendix.F) and thermal properties of water listed in Table 5-5. Note that the presented simulations are performed at realistic 1,655:1 density ratio.

The comparison of wall boundary condition's effect on bubble growth is shown in Figure 5.16. With constant wall temperature, the temperature gradient around the bubble decreases as the evaporation occurs. However, in the case using constant heat flux boundary condition, the near wall temperature gradient almost stays the same as bubble grows. The zoom-in view of temperature distribution on the bottom wall is shown in Figure 5.17. The saturated temperature contour and outline of bubble is observed close to each other for constant wall temperature

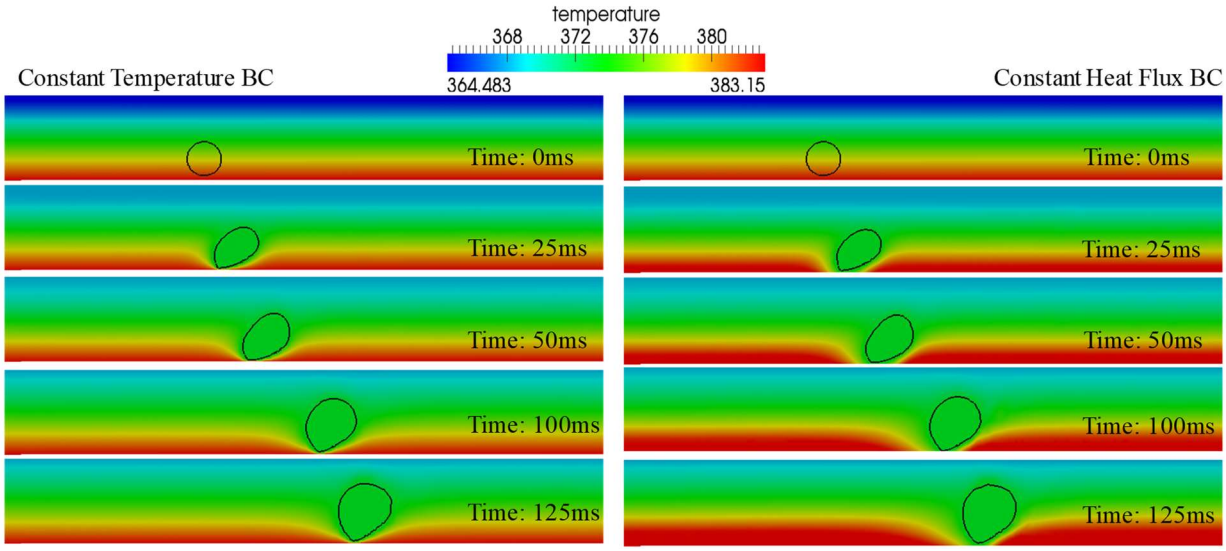

Figure 5.16. The temperature profile of flow boiling simulation that shows the bubble movement in the center slice of the domain. The black line shows the interface.

boundary condition while the saturated temperature contour is larger than bubble's outline for the constant heat flux boundary condition. The difference in the size of the saturated temperature contour indicates that the water around the bubble is cooled down quicker under the constant heat

flux boundary condition. The bubble volume evaluation over time is presented in Figure 5.18. The vapor generation rate of the bubble under different heating condition is consistent with each other

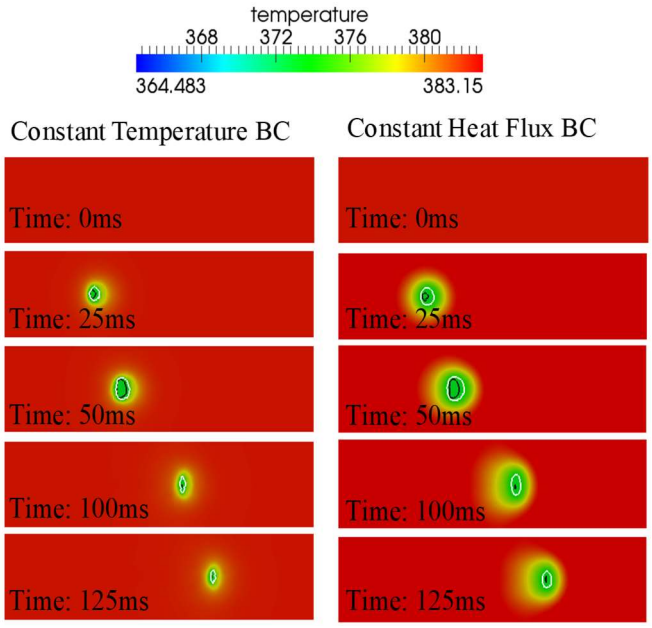

Figure 5.17. The temperature profile of flow boiling simulation that shows the bubble movement on bottom slice of the domain. Left side shows constant temperature boundary condition; right side shows constant heat flux boundary condition.

even though the heat flux through interface is different on the bubble base. It is because the area of bubble base is fairly small compared with the total bubble surface area in the flow. The contribution from the microlayer evaporation is not significant under this situation. The bubble growth rate is mainly determined by the heat flux through the liquid-vapor interface in the flow. The thermal boundary layer developed around interface (except the bubble base) is similar for the constant temperature and constant heat flux heating condition shown in Figure 5.16. The average temperature gradient values across the interface are close under these two thermal boundary conditions, which results in the consistent vapor volume increases shown in Figure 5.18.

As the first attempt of the flow boiling simulation, the results of this test case demonstrate that the boiling model in PHASTA is capable of simulating convective boiling phenomenon under various thermal boundary conditions without numerical problems, such as divergence. The overall

behavior is close to the observation of boiling phenomena. This is a **notable achievement** since many incompressible codes struggle with high density ratio two-phase flow simulations, let alone volume addition removal required for the boiling simulations presented in this research.

Table 5-5: The fluid properties in the effect of thermal boundary condition simulation.

Parameters	Water	Vapor
Density kg/m^3	958.0	0.579
Thermal conductivity W/(m · ℃)	0.679	0.025
Specific heat kJ/(kg · ℃)	2.80	2.034
Saturation temperature ℃	100	
Latent heat kJ/kg	2260.0	

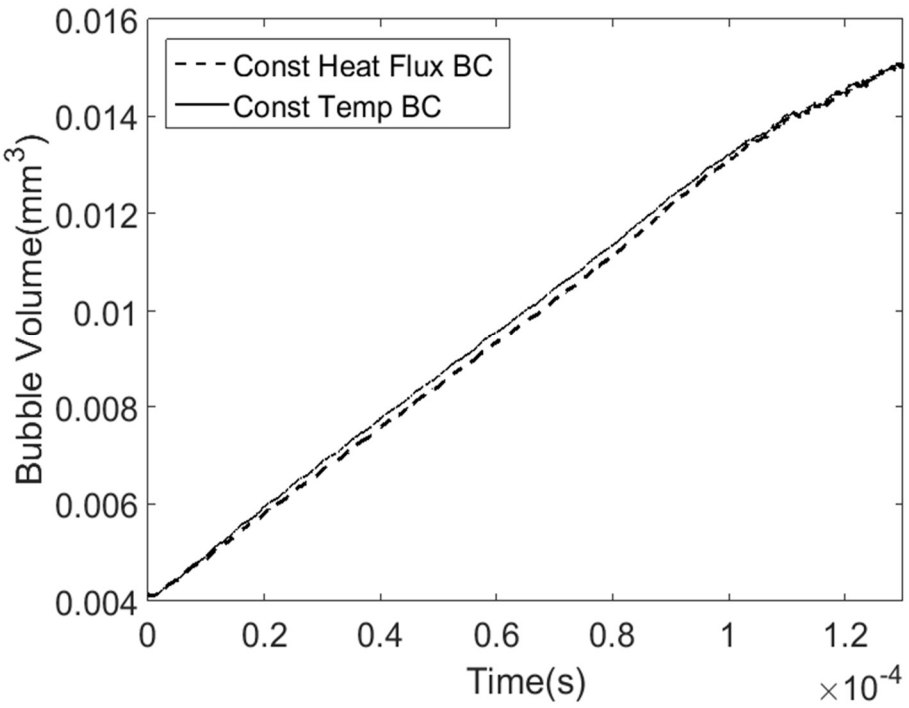

Figure 5.18. The change of bubble volume along with time for the constant temperature boundary condition and the constant heat flux boundary condition.

5.5. Single Boiling Flow Boiling Validation

The previous Section 5.4 demonstrates the performance of the boiling model in convective flow boiling scenarios, but the numerical results are not compared with any reference data. The single bubble flow boiling simulation in this section aims to validate the boiling model performance against available experimental data in the literature. A side-by-side comparison is performed for the bubble behavior during flow boiling. The bubble departure diameter and the bubble growth rate are selected to quantitatively measure the difference between numerical and experimental results.

5.5.1. The Case Setup

In the experiment of Maity [103], the test surface consisted of three rectangular ($19\text{mm} \times 99.9\text{mm}$) silicon wafers. The nucleation site is placed at the geometric center of middle wafer. For $\Delta T_{sub} = 0.2℃$, $\Delta T_w = 5.9℃$ and a liquid free stream velocity of 0.135m/s, the thermal profile near the superheated wall is measured at three different locations: $76mm$, $151mm$ and $226mm$. From the experimental setup, the thermal profile at $151mm$ is the nearest one to the nucleation point. Therefore, the thermal profile calculated at $151mm$ is used as reference data to provide the initial and boundary condition of flow boiling validation simulation.

The hydrodynamics boundary layer thickness δ for laminar flow, proposed by Kays and Crawford[112], is suggested by Maity[103] for the initial and inlet boundary conditions:

$$\delta = 4.64\sqrt{\frac{\nu x}{U}} \qquad (5\text{-}1)$$

where x is the distance from the inlet to the nucleation point ($x = 151\ mm$ in the flow boiling validation simulation), ν is the kinematic viscosity of water and U is the bulk liquid velocity. The thickness of hydrodynamic boundary layer for the flow boiling validation simulation is $2.7mm$.

The thermal boundary layer thickness δ_T is calculated based on the thickness of hydrodynamics boundary layer as [112]:

$$\frac{\delta}{\delta_T} = 1.026 Pr^{\frac{1}{3}} \qquad (5\text{-}2)$$

where Pr is the Prandtl number. The thermal boundary layer thickness for this case is $2.2mm$. The initial temperature (T_{in}) and velocity (u_{in}) profiles are written as [112],

$$\frac{u_{in}}{U} = \left(\frac{y}{\delta}\right)^{1/7}$$
$$\frac{T_{in} - T_{sat}}{T_w - T_{sat}} = 1 - \left(\frac{y}{\delta_T}\right)^{1/7} \qquad (5\text{-}3)$$

where y is the vertical distance from the bottom wall. According to the Eqs. (5-1), (5-2) and (5-3), the initial temperature profile is estimated as shown in Figure 5.19. The calculated temperature profile over-predicted the temperature in the near wall region ($y \leq 0.75mm$), but the overall behavior is quite close to the experimental data.

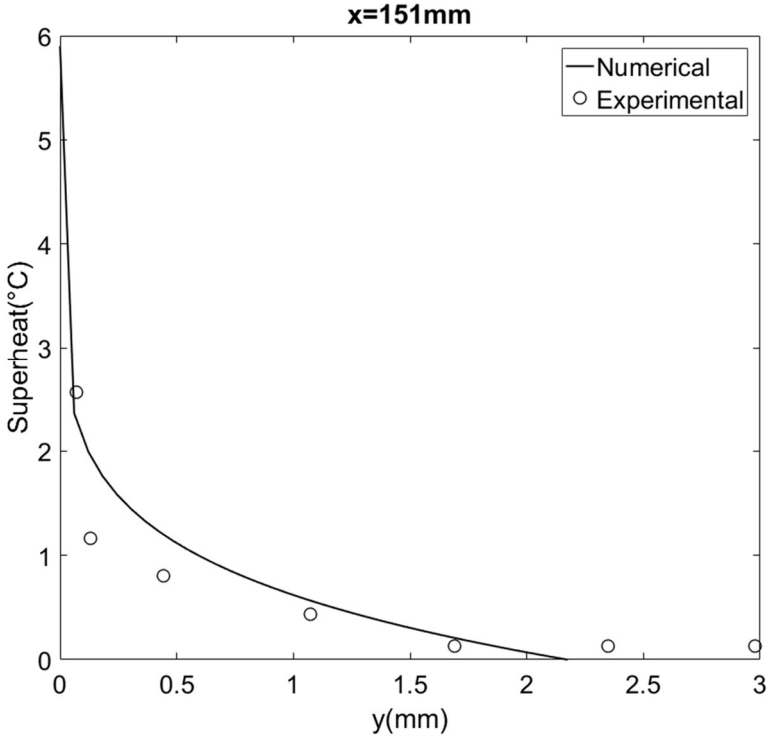

Figure 5.19. The estimated initial temperature profile compared with experimental measurements

The 3D computational domain shown in Figure 5.15 is a rectangle of dimensions $10 \times 10 \times 30\ mm^3$ in the lateral, vertical and flow directions, respectively. A small vapor bubble is initialized at $5.2\ mm$ downstream from the inlet boundary. The inflow/outflow boundary conditions are applied to compensate the volume change in the domain due to significant density ratio between the two phases. The periodic boundary condition is applied to the side walls in the lateral direction. The no-slip boundary condition is used for the top and bottom walls. The gravity is in the vertical direction. The bottom wall is uniformly heated at $105.9℃$ ($\Delta T_w = 5.9℃$). The liquid subcooling of the inlet is $0.2℃$ ($\Delta T_{sub} = 0.2℃$) and the liquid free stream velocity is $0.135\mathrm{m/s}$.

The total mesh is about 7.6 million tetrahedralized elements (except the boundary layer region), which requires 256 processing cores on the local computing cluster. The prism boundary layer elements (Appendix.C) are applied to the near wall region for accurate estimation of local contact angle and proper boundary layer development. The region of interest is refined three times as shown in Figure 5.15. The local refinement approach (Appendix.A) ensures that the bubble can always be resolved with high-resolution at relatively low computational cost for each stage of the simulation. The fluid properties used in the flow boiling simulation is listed in Table 5-6 and the simulation setup is summarized in Table 5-7.

Table 5-6: The fluid properties in the flow boiling validation simulation.

Parameters	Water	Vapor
Density $\mathrm{kg/m^3}$	958.0	0.579
Thermal conductivity $\mathrm{W/(m \cdot ℃)}$	0.679	0.025
Specific heat $\mathrm{kJ/(kg \cdot ℃)}$	2.80	2.034
Saturation temperature ℃	100	
Latent heat kJ/kg	2260.0	
The advancing contact angle (°)	50	
The receding contact angle (°)	40	

Table 5-7: The case design of flow boiling validation simulation.

Geometry	
Domain size	$10 \times 10 \times 30$mm
Initial radius	0.3mm
Mesh	7,627,228
Elements across diameter	30
Boundary conditions	
Bottom wall	105.9℃
Inflow temperature	99.8℃
Inside bubble	100℃
Bulk flow velocity	0.135m/s

5.5.2. Results and Analysis

A small bubble is initially placed on the bottom wall of the domain. The local superheat results in the thermal boundary layer developing around the interface. As the bubble grows, the vapor accumulates inside the bubble and pushes the interface. The cooler liquid on the top of the bubble mixes with the superheated liquid near the bottom wall. The advancing and receding contact angles are affected by the local liquid velocity around the bubble. The departure of the bubble occurs under the combined effect of buoyancy force, interfacial forces (including lift, drag, turbulence dispersion and wall effect forces) and surface tension force (which keeps the bubble attached to the wall until the other forces overcome this effect). A side-by-side comparison is presented between the numerical bubble growth and the experimental observations for the bubble behavior during flow boiling in Figure 5.20 [103]. The numerical bubble size is comparable to the experiment for each time step. The bubble departure time is very close to the one observed in the experiment. The bubble base diameter is larger in the simulation than the experimental one. This difference may result from the numerical approach to introduce the bubble: a small bubble is directly initialized on the wall instead of growing from a micro-scale nucleation site. Even though the micro-scale nucleation site cannot be resolved with DNS approach, this problem could be minimized by decreasing the initial bubble size and utilizing multi-refinement box around the initial bubble.

To quantitatively compare the numerical results to the experimental data, the evolution of the bubble diameter over time is plotted in Figure 5.21. Three sets of bubble diameter data are repeated measured in the experiments. The numerical bubble growth rate is within the region of the experimental data and has especially good agreement with the second data set. The ITM boiling model is validated via the comparison between this single bubble flow boiling simulation and Maity's experiment [103]. The single bubble flow boiling validation demonstrate the model

capability of simulating convective boiling scenarios with high accuracy, which enhance our confidence in applying this boiling model to future complex and large-scale boiling simulations.

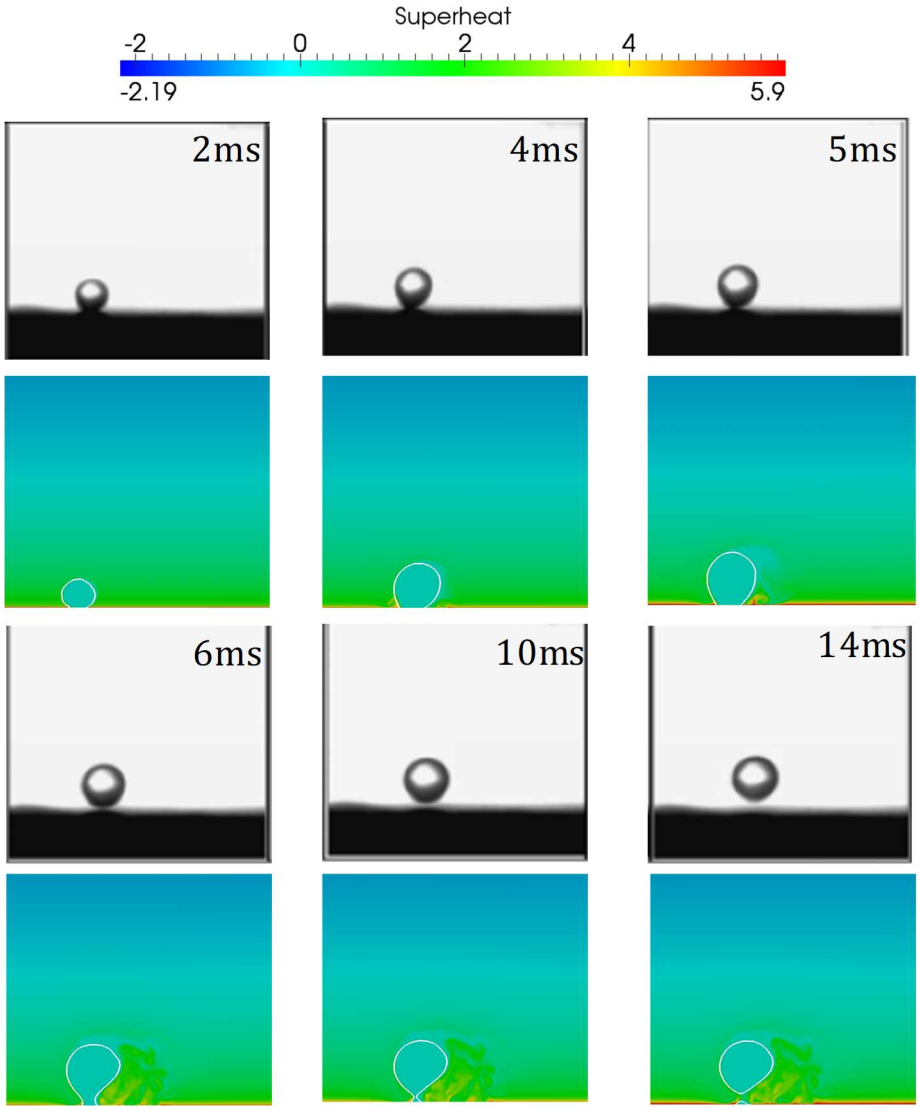

Figure 5.20. The comparison between numerical flow boiling simulation and experimental observation of bubble growth in flow boiling scenario (the time estimation refers to simulation results) [102].

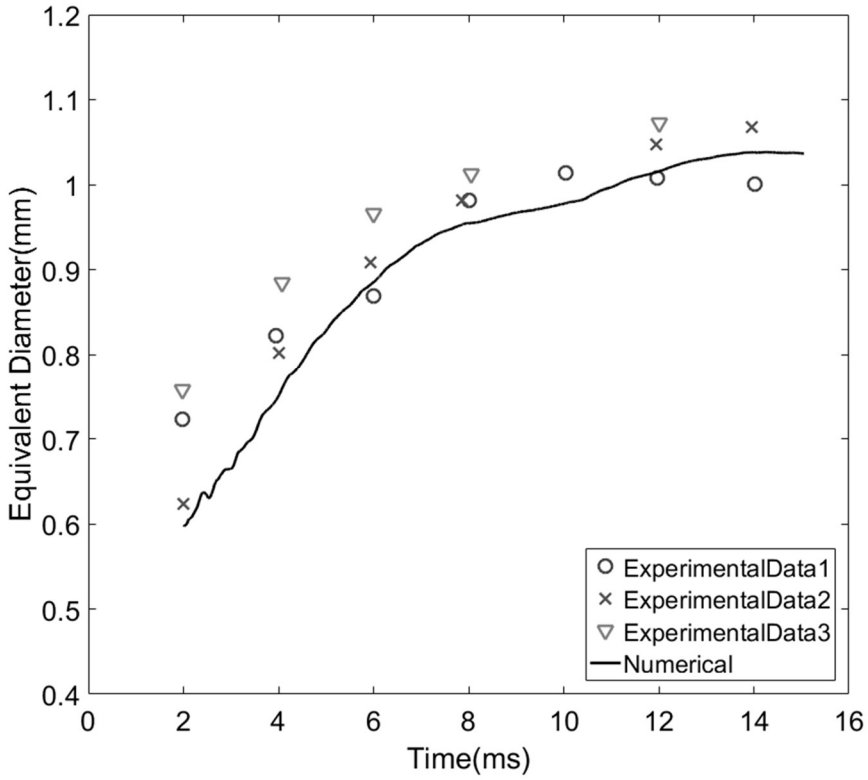

Figure 5.21. The comparison of the bubble growth rate in the flow boiling scenarios.

5.6. Multiple bubble Flow Boiling Simulation

The boiling simulations presented in the previous sections (Section 5.1-5.5) all focus on single bubble boiling phenomenon. The multiple bubble flow boiling scenario is considered in this section. Four bubbles are initialized on the heated wall with an inclined plate structure in the center of the domain resembling a very simplified spacer grid and mixing vane. Thus, the bubbles behavior under more complex temperature and velocity scenario is investigated. The bubble dynamics information (e.g. bubble diameter) is collected individually using BTA (Section 2.6). This multiple bubble flow boiling simulation demonstrates the potential of ITM boiling model in studying multiple bubble behavior under complex flow conditions. This capability can be a powerful tool for the closure development of multiphase computational fluid dynamics models and performing large scale virtual experiments on the LWR subchannel geometries and conditions in the future.

5.6.1. The Case Setup

There are four bubbles placed on the heated bottom wall of computational domain bounded by two parallel plates as shown in Figure 5.22. A spacer grid-like plate is placed in the center of the domain to invoke flow instabilities and provide variable conditions for the locations with sitting bubbles. The first part of this block is parallel to the walls and the second part is inclined to the bottom wall. The existence of the structure disturbs the main flow stream and induces turbulence in the wake region. The vortex enhances the temperature mixing and the heat transfer rate in the region downstream from the block. The typical phenomenon is similar to the scenario near the mixing vane in a reactor subchannel. The schematic of geometry setting is shown in Figure 5.22. A periodic boundary condition is applied to the side walls. A constant uniform velocity profile is applied to the inlet boundary while the natural pressure for the outlet boundary. A constant heat flux boundary condition $q'' = 180kW/m^2$ is applied to the heated patch on the bottom wall. The

inlet flow is subcooled, with temperature of 92℃. The thermal properties used in the simulation are listed in Table 5-8.

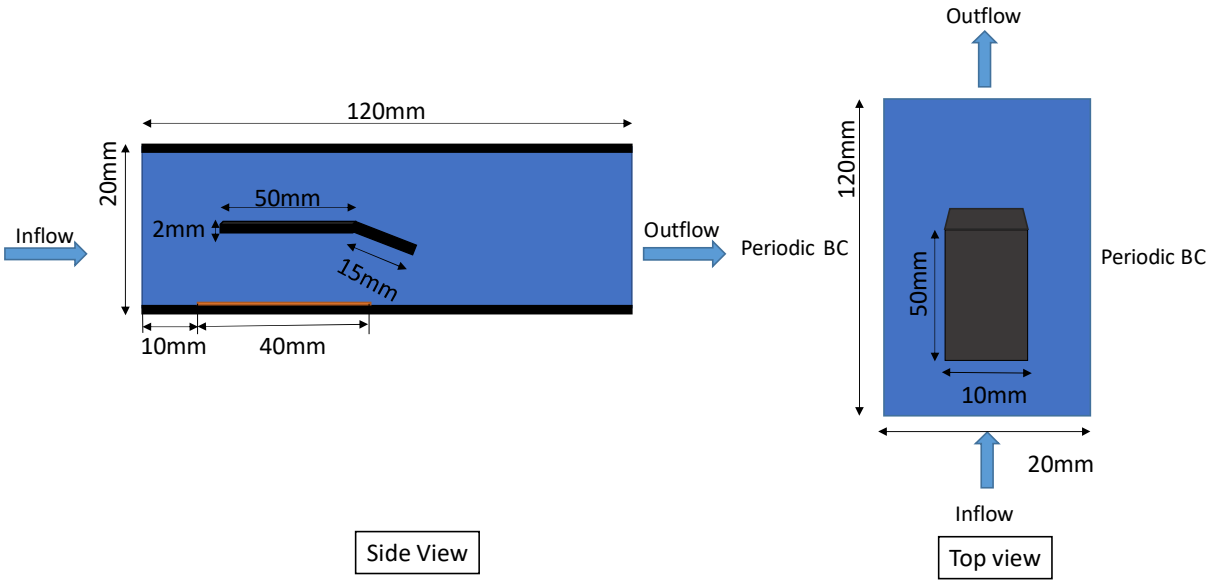

Figure 5.22. The schematic picture of the domain design.

Table 5-8: The fluid properties in the multi-bubble flow boiling simulation.

Parameters	Water	Vapor
Density kg/m^3	958.0	0.579
Thermal conductivity W/(m · ℃)	0.679	0.025
Specific heat kJ/(kg · ℃)	2.80	2.034
Saturation temperature ℃	100	
Latent heat kJ/kg	2260.0	

5.6.2. The Results of Single-Phase Flow with Heat Transfer

The single-phase flow simulation is performed first. Figure 5.24 shows the fully developed velocity and temperature profile. The block in the center invokes the flow instabilities, which results in a significant increase in velocity field in the region near the inclined block and a stagnant region near the top wall. The existence of the block insulates the heat transfer from the heated wall to the top wall region. Meanwhile, the vortex in the wake region enhances the temperature mixing and the heat transfer rate in the region after the block.

Four identical bubbles are initialized in the domain with different hydrodynamic and thermodynamic conditions. The influence of local environment on bubble behavior is investigated. The initial bubble positions are deliberately selected according to the local velocity and temperature distribution shown in Figure 5.23. The local refinement (Appendix.A) is applied to

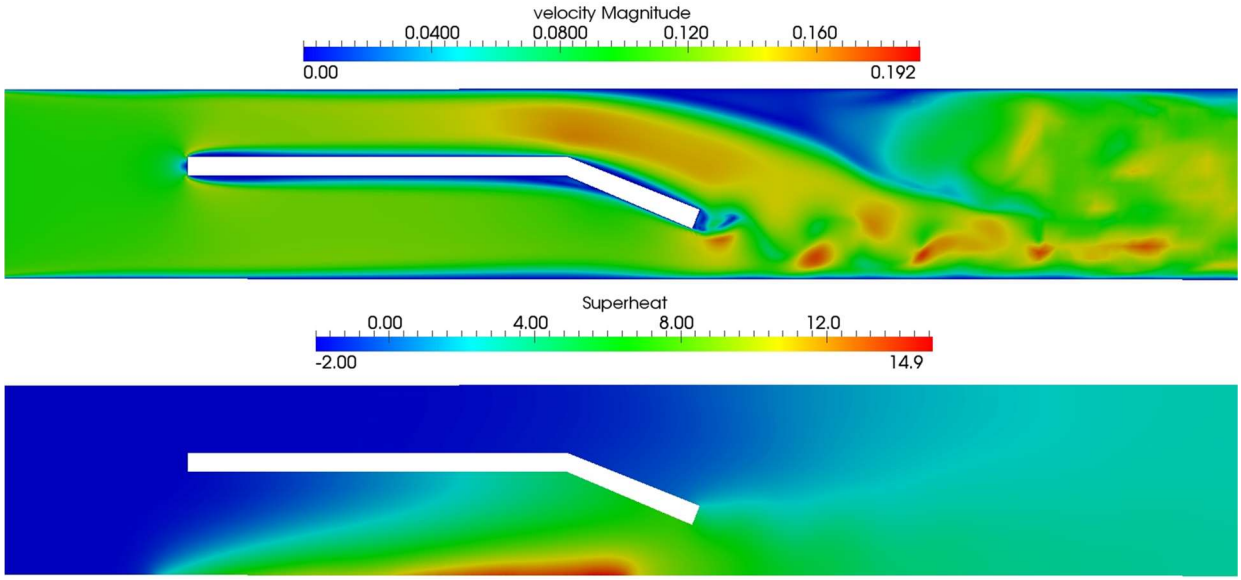

Figure 5.24. The fully developed velocity and temperature profile of single phase simulation. The left picture is the distribution of velocity from the side view; the right picture is the temperature distribution (the saturation temperature is 100°C).

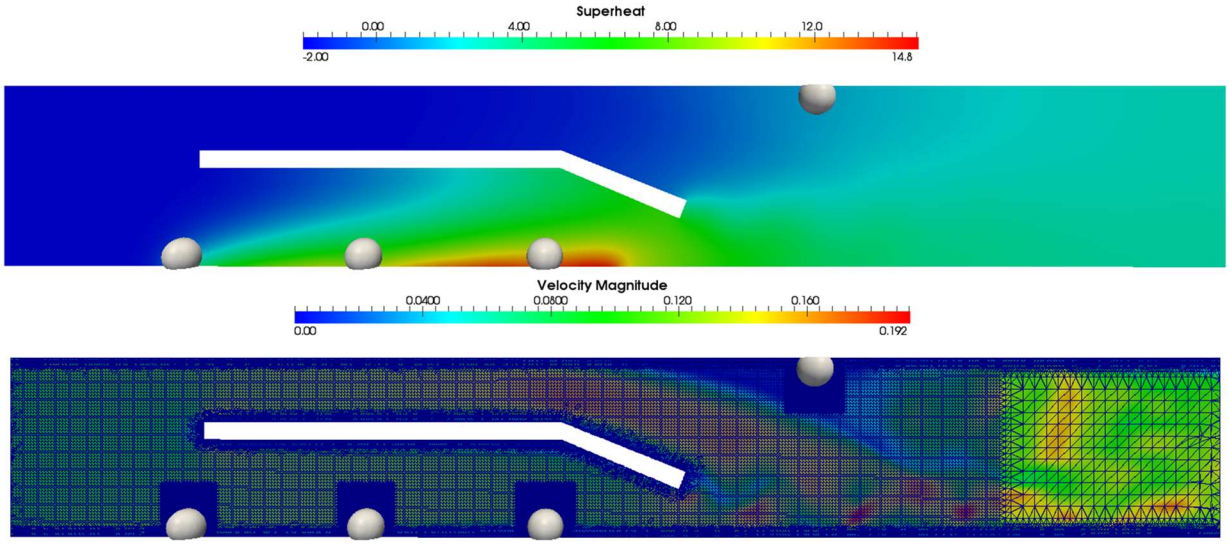

Figure 5.23. The initial bubble positions in the domain. The temperature field is shown on the top picture while the velocity field is shown on the bottom with the mesh design in the background.

the bubble region to resolve the bubble shape, the interface and the sharp temperature gradients at the bubble interface accurately. The prism boundary layer elements (Appendix.C) are applied to the near wall region for an accurate estimation of the local contact angle and proper hydrodynamic and thermal boundary layer development.

5.6.3. The Results of Multiple Bubble Flow Boiling

The first bubble is placed near the subcooled inlet flow. Bubble condensation is expected to occur at this location according to the single-phase temperature distribution. The second and the third bubble are under the simulated spacer grid. The superheat rate is relatively high in this region. The heat accumulates along the channel as the flow develops, so the third bubble is expected to have a higher evaporation rate compared with the second bubble and depart earlier due to the high local velocity. The fourth bubble is expected to depart later compared to other bubbles because of the low local velocity in its vicinity which may result in smaller drag and lift force on the growing bubble.

The snapshots in Figure 5.25 show the bubbles' growth and departure during the flow boiling. The evolution of the local contact line (the triple contact line between solid, liquid and gas phase) indicates the movement of the interface due to the application of contact angle control algorithm. The local superheat/subcooling results in various temperature gradients around each bubble. The first bubble is the earliest one to depart from the wall ($t = 1.83ms$) and its followed by the second bubble ($t = 2.11ms$). The third bubble lift off from the wall at around $t = 2.62ms$ and is followed by the forth bubble. The BTA is utilized in the multiple bubble flow boiling simulation to collect the information on the individual bubbles. The evolution of bubble radius over time is presented in Figure 5.26. After the departure from the wall, the first bubble is observed to condense after $5ms$ due to the increasing local subcooled condition created by the subcooled

inlet flow. The volume of the second bubble keeps increasing from beginning to about 14ms, and decreases when the bubble moves upward to the subcooled region. The evolution of the third bubble follows the same trend as with the second bubble. However, the superheat in Figure 5.25 indicates that the local temperature field around the third bubble is positive through all the simulation time. The shrink of the bubble sizes may result from the deformation of bubble shape after lifting off from the wall. The sharp curvature of the interface is under-resolved and may lead to mass loss. This issue can be improved in the future simulations by applying finer mesh to the region of interest (the whole region from the location of the first bubble to the one of the forth bubble). Another possible reason is delay response of the thermal boundary layer developing around the bubble. In the evaporation and condensation model (CHAPTER 3), the temperature gradient is collected at 1ε to 2ε region outside the bubble. In transient simulation, the thermal boundary layer may not fully develop around the bubble as the bubble moves, which results in the under-estimation of the average temperature gradient in the evaporation and condensation model. The average superheat value at the interface is very small for the forth bubble, therefore the size of the forth bubble does not change much in the near wall region and gets smaller when it reaches the cooler liquid. The fluctuation in the bubble equivalent diameter may be caused by the bubble deformability while lifting off from the wall. In the evaporation and condensation model, the heat transfer through interface is calculated using the equation for spherical surface area (Eq.(3-10)). The effect of bubble Eotvos number on the growth rate could be investigated in the future to improve the current boiling model.

To summarize, the multiple bubble flow boiling scenario has been tested for the boiling model without any numerical issues (e.g. divergence). The local bubble behavior is investigated in the unstructured mesh domain at four locations which exhibit qualitatively different behaviors.

The bubble dynamics information is successfully collected for each bubble using BTA. The lesson learnt from the simulation including local refinement mesh design and possible limitation of the ITM boiling model will help guide the mesh design of future multiple bubble boiling simulations and improve the boiling model accuracy under complex flow conditions. In general, this multiple bubble flow boiling simulation demonstrates the potential of ITM boiling model in studying multi-bubble behavior under complex flow conditions.

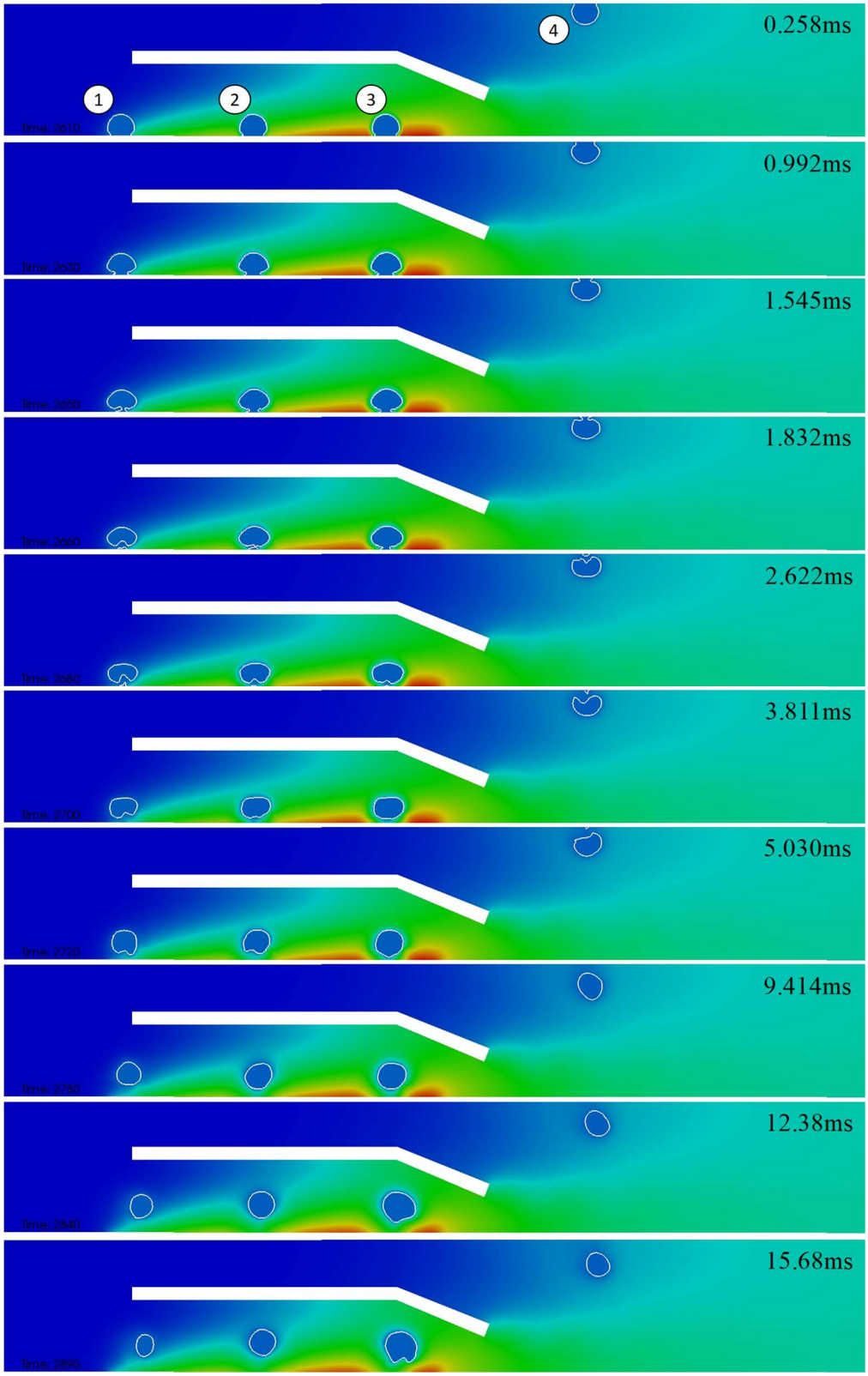

Figure 5.25. The results of multi-bubble flow boiling simulation. The snapshots show the temperature distribution evolution. The contour in white line shows the bubble interface.

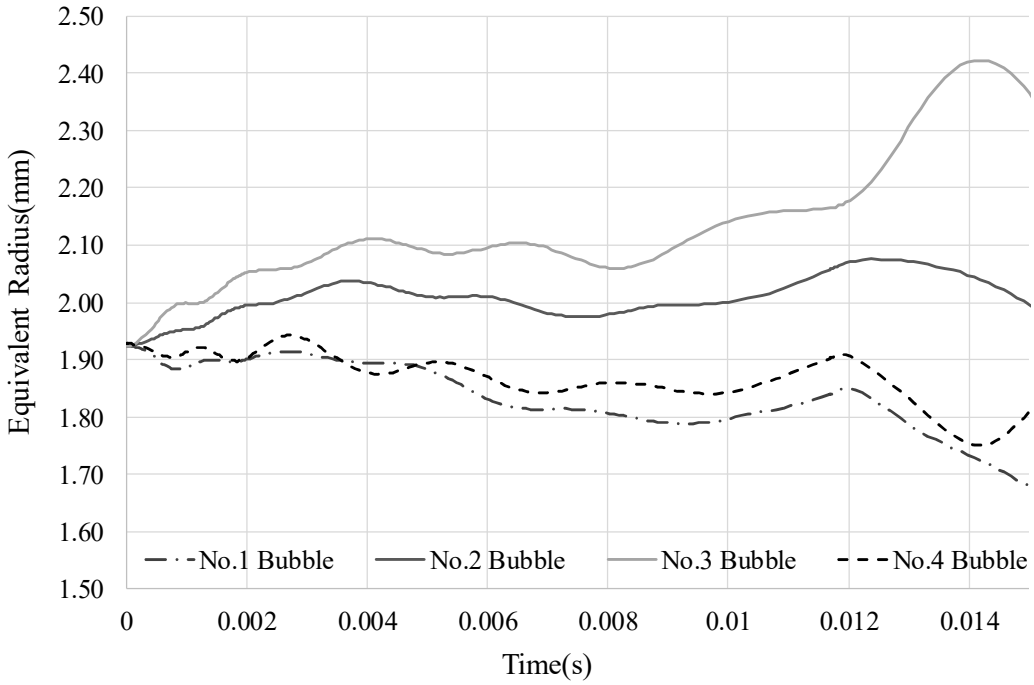

Figure 5.26. The growth rate of each bubble in flow boiling.

CHAPTER 6. CONCLUSIONS

6.1. Summary Remarks on ITM Boiling Model Development

The evaporation and condensation model is developed and implemented in the ITM multiphase flow solver – PHASTA. This model is designed to resolve 3D interface in complex geometries represented with the unstructured mesh. This unique capability allows us to investigate the boiling phenomenon in various conditions with lower computational cost (by utilizing localized mesh refinement for bubble growth region) compared to uniformly refined structured meshes. The verification of the evaporation and condensation model has been conducted by comparing the bubble growth rate with analytical solutions with good agreement. The mesh sensitivity study shows that the accuracy of the numerical results from the boiling simulations increases as the mesh becomes finer and converges to a stable small relative error (1.85%). The parametric study on different superheat values demonstrates that the boiling model has good performance over a wide superheat range. The evaporation and condensation model is successfully coupled with the bubble tracking algorithm (BTA) which collects the detailed information regarding the individual bubble behavior in level-set method to achieve multiple bubble growth capability. The multiple bubble evaporation is presented and verified against analytical solution with high accuracy (1.92%). The multiple bubble growth capability is essential for studying the characteristics of boiling phenomenon like bubble release frequency, bubble departure diameter, nucleation site density and for applying the boiling model to engineering applications. The contact angle control algorithm previously developed in the research group has been improved and verified in massively parallel interface tracking flow solver, PHASTA. This algorithm provides a novel approach to maintain the contact angle in three-dimensional interface tracking simulations with unstructured computational mesh. Two different scenarios are simulated to demonstrate the model

capability. The single bubble lift-off from the wall simulation verifies the model performance under bubble departure scenario. The contact angle observed in the simulation is compared with the analytical contact angle from force balance analysis, which shows good agreement. The mesh resolution sensitivity study and parametric study are conducted to demonstrate the reliability of the contact angle control algorithm. The contact angle model is capable of maintaining correct contact angle under various conditions. This unique feature will fill the gap in PHASTA boiling model development, which is essential for accurate modeling of the boiling phenomenon.

6.2. Summary Remarks on ITM Boiling Simulations

The boiling simulations presented in the thesis is the first-of-its-kind high-resolution ITM boiling simulations conducted in the domain with 3D unstructured mesh. The local refinement, unstructured mesh and highly scalable performance are essential for conducting high resolution large scale boiling simulation. To be more specific, both pool boiling and flow boiling simulations are performed with the ITM boiling model implemented in this work. The Single Bubble Growth with Non-uniform Temperature Distribution (5.1) and Single Bubble Growth and Departure (5.2) demonstrate the successfully coupling between different capabilities including evaporation and condensation model, contact angle control algorithm, and bubble tracking algorithm. The Nucleate Boiling from Single Site (5.3) validates the numerical bubble release frequency in pool boiling simulation with commonly-used experimentally-based correlations. The Effect of Thermal Boundary Condition (5.4) on the temperature distribution and bubble growth is discussed. The overall behavior is close to the observation of boiling phenomena. This flow boiling simulation demonstrates the boiling model is not only able to correctly represent pool boiling phenomenon, but also convective flow boiling physics. The Single Boiling Flow Boiling Simulation (5.5) compared the bubble evolution and growth rate with experimental data. The multi-bubble flow

boiling simulation (5.6) explores the potential of the ITM boiling model in solving boiling problems with complex geometries.

6.3. Summary Remarks on High Resolution Boiling Simulation Methodology development

The development and validation of 3D multiphase computational fluid dynamics (M-CFD) model and physics-informed data-driven modeling require data of high-quality and high-resolution. Considering the difficulties in acquiring the corresponding experimental data in prototypic conditions, two-phase simulations by ITM-based models can be used for generating high-resolution numerical data in a consistent, best-estimate, and relatively economical manner. The presented research demonstrates the potential of the PHASTA boiling model in studying bubble dynamics and heat transfer mechanism of boiling phenomenon in large scale and its suitability for future engineering applications. This ITM boiling lays the foundation of high resolution boiling simulation in PHASTA. It fulfills the numerical data gap between the reduced scale and the engineering scale: the mechanism study on local boiling phenomenon can be considered in this ITM boiling model as subgrid model and utilized for study the quantities of interest in large scale boiling simulation for engineering applications. As a powerful tool to generating high-quality, high-resolution numerical data, this ITM boiling model could help improve multiphase computational fluid dynamics models and perform virtual experiments on the much larger scale (billions of mesh cells on tens of thousands of computing cores) which would fully represent light water nuclear reactor (LWR) subchannel geometries and conditions.

CHAPTER 7. FUTURE WORK

The systematic approach based on high-resolution boiling simulation by the interface tracking method (ITM) developed in the thesis will enhance the understanding of nucleate boiling phenomenon and support the development of system thermal hydraulics closures. The author envisions that high resolution ITM large scale boiling simulation in light water nuclear reactor (LWR) subchannel geometries and conditions, which provides detailed physics-based description associated with thermal and hydrodynamic processes and the shape of the evolving interface, will bring new insight on the understanding of boiling phenomenon in nuclear reactor. The numerical data of bubble nucleation and growth cycle generated from ITM boiling simulation can fill the need of mechanistic boiling model development and prediction and support the physics-informed data-driven modeling. This chapter provides four directions to improve the current boiling model and explore the potential of this model in engineering applications. The preliminary results for each direction are presented. The possible technical approaches for future work are discussed.

7.1. Further Development of ITM Boiling Model

The step-by-step verification approach is utilized to evaluate the correctness of the model implementation and to determine the possible source of uncertainties in the boiling simulation. The numerical bubble growth rate is compared with analytical solution for single bubble and multiple bubble simulations. In the verification simulation, the vapor bubble is growing in a quiescent, uniformly superheated liquid and far away from the wall. In the pool and flow boiling simulation presented in CHAPTER 5, a small size bubble is initialized in the domain to avoid the early stage of bubble growth, where the heat transfer was primarily by microlayer evaporation. In future application, the ITM boiling is expected to cover the early stage of bubble growth, which will improve the accuracy of bubble characteristics prediction (e.g. bubble release frequency). In

some circumstances where the bulk temperature is highly subcooled, the condensation may occur locally during the bubble growth. A more sophisticate temperature gradient averaging approach may be needed to simulate such boiling scenarios. In this subsection, two essential improvements of the boiling model are discussed.

7.1.1. Micro-layer Evaporation Model

In nucleate boiling on a heated surface, the very thin liquid layer 'left behind' on the surface as vapor bubbles grow is named micro-layer. Vapor generated via microlayer evaporation is recognized as important contributor to the early stage of bubble growth in low-pressure boiling. The contribution of microlayer evaporation to bubble volumetric growth in boiling of water may be up to 60% according to Sato and Niceno [113] while other investigators suggest a smaller (about 20%) contribution [114]. Even though we still do not have a perfect answer to the mechanism of microlayer evaporation, the existence of micro-layer is confirmed by experiments.

Sharp [115] and Jawurek [116] experimentally observed the liquid thin layer underneath the growing bubble. The recent measurements by Yabuki and Nakabeppu [117] reported that the temperature distributions in the vicinity of nucleation sits indicated dynamics heat transfer phenomena below an isolated bubble including microlayer, dry-out of the microlayer, and rewetting of the dry-out region. The pioneer work of numerically computing bubble growth with micro-layer effect was done by Lee and Nydahl [118]. The research group of Dhir proposed a micro-layer model for constant-temperature heater surface [119] and performed a series of boiling simulation including bubble merging processing during nucleate boiling [17, 18], single-bubble dynamics in flow boiling [13], and single-bubble dynamics in subcooled pool boiling utilizing this micro-layer model. Sato and Niceno [113] proposed a depletable micro-layer model for nucleate pool boiling and successfully utilized it for their boiling regime simulation [14]. However, the ITM

boiling simulations have been conducted so far all focuses on cuboid or tube-like domain with structured mesh. As further development of the ITM boiling model for 3D simulations using unstructured mesh, the micro-layer model is proposed to be implemented in PHASTA.

The micro-layer thickness $\delta(\mathrm{m})$ is treated as a variable stored in the wall-adjacent elements which is determined by their distance to the wall. The temperature at the liquid-vapor interface over the micro-layer region is set to be the saturation temperature (T_{sat}). The liquid in the micro-layer is assumed to be stagnant, so the heat convection mechanism is ignored in the micro-layer region. The upper surface of the micro-layer could move due to the evaporation, but the heat transfer caused by the movement of the liquid inside the micro-layer is negligible. Therefore, the heat flux through the micro-layer could be expressed as,

$$q_{ml} = \lambda_l \left(\frac{T_w - T_{sat}}{\delta} \right) \quad (7\text{-}1)$$

where $\lambda_l(\mathrm{W/km})$ is the thermal conductivity of the liquid, $T_w(\mathrm{K})$ is the local wall temperature, and δ is the thickness of the micro-layer. Then the element-average heat flux of micro-layer ($\overline{q_{ml}}$)

$$V_{ml} = \frac{\overline{q_{ml}}}{h_{fg}(\rho_l - \rho_v)} \quad (7\text{-}2)$$

is calculated using q_{ml}. The phase-change rate per volume is estimated as,

The total change-phase rate added into the continuity equation is the summation of micro-layer phase-change rate (V_{ml}) and the original phase-change rate ($V_{interface}$) calculated by evaporation and condensation model shown as below,

$$V = V_{ml} + V_{interface} \quad (7\text{-}3)$$

7.1.2. Estimation of Average Temperature Gradient by Region

In the current version of the evaporation and condensation model, the temperature gradient is averaged around the bubble interface. This approach makes the phase-change estimation algorithm more efficiently, especially in large scale simulation (e.g. hundreds of bubble in subchannel geometry) and compresses the numerical fluctuations near the interface. However, in some circumstances like subcooled boiling scenario, this type of average approach may not be always accurate because it cannot separate the condensation in the top subcooled region and the evaporation in the bottom superheat region. Therefore, the region-average approach can be implemented to the boiling model as an option, which could be activated in simulations with complex temperature distribution. In consideration of computational cost and representation of correct physics, we propose to divide the vicinity of the bubble into several regions (e.g. three regions) according to their distance to the wall, collect the temperature gradient information for each region and estimate the phase-change volume separately. The typical temperature collection regions are suggested in Figure 7.1.

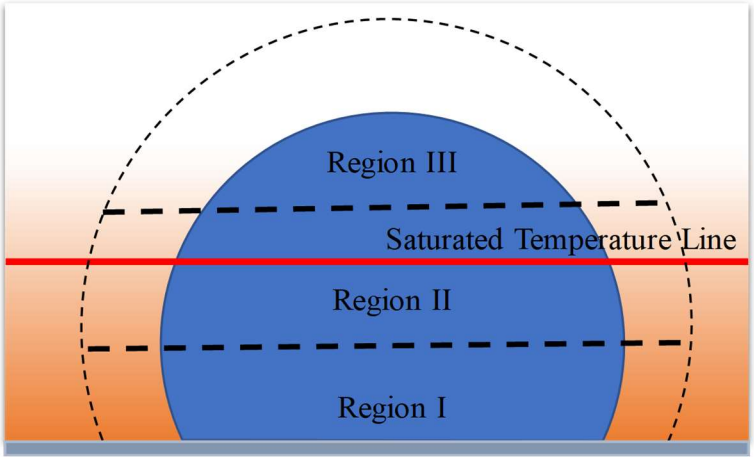

Figure 7.1. The schematic of different bubble regions for temperature gradient collection.

7.2. Investigate the physical mechanisms of the bubble nucleation sites interaction

As the distance between neighboring nucleation sites changes, one nucleation site could either promote or inhibit the nucleate process of the nearby sites. The interaction between the bubbles forming at adjacent nucleation sites has a significant influence on the characteristics of the nucleate boiling process, like bubble release frequency, departure diameter and active nucleation site density[120-122]. However this interaction between neighboring nucleation sites is either not considered [29, 50] or relies on empirical correlation[52] in most nucleate boiling models because the high-resolution experimental data are hard, expensive and time-consuming to obtain. With the advanced computation resources, the high-resolution boiling simulation with interface tracking method can provide detailed flow and interface dynamics information of nucleation site interaction [17, 92] to help developing nucleate boiling models with high accuracy.

A three-step approach to proposed to investigate the bubble nucleation site interaction with the ITM boiling model in PHASTA: 1) Implement the conjugate heat transfer model and the bubble waiting time model to represent the complete physics of nucleate boiling phenomenon. For conjugate heat transfer model, the near-wall cells in the domain will be blocked as “wall cell” with zero velocity, where the solid thermal properties are applied. The 3D energy equation can be solved for time- and position-dependent temperature field. The bubble waiting time will introduce 1D evaporation model in the cell with a nucleation site to be solved with a simple ordinary differential equation (ODE) based on local fluid conditions. Using a time-dependent wall temperature as the boundary condition, the growth rate of inside-cavity nucleation can be estimated; 2) Validate the nucleation site interaction model against the experimental results from two artificial nucleation site interaction in a pool boiling [122]. 3) The phenomenon of nucleation site interaction is governed by three physical mechanisms: hydrodynamic interaction between bubbles, thermal interaction between nucleation sites and horizontal and declining bubble coalescences. The

intensity, competition and dominance relations of these three factors determine the activation and inhibition between nucleation sites. A series of parametric studies can be performed on two and three neighboring nucleation site using high-resolution boiling simulation to investigate the nucleation site interaction in consideration of these three factors. The simulation results will help the understanding of physical mechanisms for the nucleation site interaction, and it can be applied in both pool boiling and flow boiling scenarios.

7.3. Provide high resolution numerical data for the mechanistic heat flux partitioning model

The partitioning of wall heat flux can provide valuable information of bubble characteristics in the reactor coolant channel, which is essential for two-phase thermal hydraulics and M-CFD model development. As the understanding of boiling phenomenon deepens, the mechanistic models of heat flux partitioning [47, 123] have been proposed in recent years to replace the empirical correlations in the M-CFD simulations. These mechanistic models require necessary inputs like nucleation site density, bubble departure diameter and release frequency. Therefore, the need for the high-quality high-resolution data on the bubble nucleation and growth cycle is increasing. The subprocesses of nucleate boiling including density of active nucleation sites, thermal response of heater, bubble dynamics and heat transfer mechanisms are tightly coupled. These complex interactions can be considered simultaneously in high-resolution boiling simulation with interface tracking method.

The multi-bubble nucleate flow boiling simulations in subchannel geometry under PWR temperature / pressure normal operating conditions is proposed. The adiabatic turbulent bubbly flow simulation in PWR subchannel geometries has been successfully performed using PHASTA [124]. In the nucleate boiling simulation, 300 randomly distributed pre-defined nucleation sites will be introduced to the wall surface of the PWR subchannel. With unstructured meshes and mesh

adaptivity, the addition meshing requirements are affordable with hundreds of pre-defined nucleating sites (less than 1% mesh increase compared to the adiabatic simulation) [125]. Information about the heat removed by the boiling fluid can be extracted from the high-resolution simulation: The latent heat of evaporation is estimated from bubble growth rate; The results of nucleation site interaction is applied to determine the conductive heat transfer to the liquid in between bubble growth as quench heat flux; The heat transferred to the liquid phase outside the zone of influence of the bubble is estimated as convection heat flux.

The ITM boiling model with information extraction approach can fulfill the needs of mechanistic heat transfer models. In addition, this attempt of high-resolution nucleation boiling simulation in the PWR subchannel geometries demonstrate a framework for supporting the model developments with the high-resolution boiling simulation data. Such framework can be used for guiding the development of M-CFD.

7.4. Develop a high-quality high-resolution simulation database of local boiling phenomenon

The advances in high-performance computing (HPC) dramatically reduce the computation and data storage cost and make it possible for high-resolution simulations to produce more and more data in the future. Meanwhile, the validation of 3D multiphase computational fluid dynamics (M-CFD) model and physics-informed data-driven modeling require huge amount of high-quality high-resolution data. Therefore, we propose to develop a high-quality high-resolution simulation database of local boiling phenomenon to build the bridge from data producer to the user. Furthermore, this database can be integrated into the NE-KAMS framework developed in Oak Ridge National Lab to help promoting and supporting nuclear knowledge management and computational simulation code validation.

There are four steps to build the high-quality high-resolution simulation database of local boiling phenomenon**:** (1) Standardizing data formats: The concept of "virtual container" proposed in the NE-KAMS program is adopted [126]. The physical regime map will be employed to categorize the boiling simulations. For each category, the datasets from the same domain geometry will be stored in one sub-category. Under each sub-category, simulations with the same initial and boundary conditions will be stored in one 'virtual container'. (2) Simulation data management: The Python package—Pandas will used to store and query the virtual container. (3) Data transfer and access control: The cloud computing is considered to centrally store and distribute the dataset (e.g. Amazon Web Service (AWS)). (4) Simulation data analysis: The temporal- and spatial-averaging algorithm will be developed in Python for postprocessing raw data, extracting physical mechanisms, identifying important physical features, and so on.

The database will be built for storing, managing, and analyzing the high-resolution boiling simulation data. The database can improve the transparency of data generation, reduce the difficulty of data acquisition, and potentially boost the process of model development and validation.

REFERENCES

[1]. Fletcher, C., and Schultz, R., 1995, "RELAP5/MOD3 Code Manual Volume V: User's Guidelines," Idaho National Engineering Laboratory, Idaho Falls, ID, .

[2]. Bajorek, S., 2008, "TRACE V5. 0 Theory Manual, Field Equations, Solution Methods and Physical Models," United States Nuclear Regulatory Commission, .

[3]. George, T.L., 2001, "GOTHIC Containment Analysis Package Installation and Operations Manual ," Numerical Applications, Inc, Richland, WA, .

[4]. Cuervo, D., Avramova, M., Ivanov, K., 2006, "Evaluation and Enhancement of COBRA-TF Efficiency for LWR Calculations," Annals of Nuclear Energy, **33**(9) pp. 837-847.

[5]. Ustinenko, V., Samigulin, M., Ioilev, A., 2008, "Validation of CFD-BWR, a New Two-Phase Computational Fluid Dynamics Model for Boiling Water Reactor Analysis," Nuclear Engineering and Design, **238**(3) pp. 660-670.

[6]. Anglart, H., and Nylund, O., 1996, "CFD Application to Prediction of Void Distribution in Two-Phase Bubbly Flows in Rod Bundles," Nuclear Engineering and Design, **163**(1) pp. 81-98.

[7]. Drew, D., and Lahey Jr, R., 1990, "Some Supplemental Analysis Concerning the Virtual Mass and Lift Force on a Sphere in a Rotating and Straining Flow," International Journal of Multiphase Flow, **16**(6) pp. 1127-1130.

[8]. Moraga, F., Larreteguy, A., Drew, D., 2003, "Assessment of Turbulent Dispersion Models for Bubbly Flows in the Low Stokes Number Limit," International Journal of Multiphase Flow, **29**(4) pp. 655-673.

[9]. Kurul, N., and Podowski, M. Z., 1990, "Multidimensional effects in forced convection subcooled boiling," Proceedings of the Ninth International Heat Transfer Conference, Hemisphere Publishing New York, **, 2,** pp. 19-24.

[10]. Moser, R., and Moin, P., 1984, "Direct Numerical Simulation of Curved Turbulent Channel Flow," .

[11]. Lee, M., Malaya, N., and Moser, R. D., 2013, "Petascale direct numerical simulation of turbulent channel flow on up to 786k cores," Proceedings of SC13: International Conference for High Performance Computing, Networking, Storage and Analysis, ACM, pp. 61.

[12]. Dabiri, S., and Tryggvason, G., 2015, "Heat Transfer in Turbulent Bubbly Flow in Vertical Channels," Chemical Engineering Science, **122**pp. 106-113.

[13]. Li, D., and Dhir, V. K., 2007, "Numerical Study of Single Bubble Dynamics during Flow Boiling," Journal of Heat Transfer, **129**(7) pp. 864-876.

[14]. Sato, Y., and Niceno, B., 2017, "Nucleate Pool Boiling Simulations using the Interface Tracking Method: Boiling Regime from Discrete Bubble to Vapor Mushroom Region," International Journal of Heat and Mass Transfer, **105**pp. 505-524.

[15]. Son, G., and Dhir, V. K., 2008, "Numerical Simulation of Nucleate Boiling on a Horizontal Surface at High Heat Fluxes," International Journal of Heat and Mass Transfer, **51**(9) pp. 2566-2582.

[16]. Son, G., Dhir, V., and Ramanujapu, N., 1999, "Dynamics and Heat Transfer Associated with a Single Bubble during Nucleate Boiling on a Horizontal Surface," Journal of Heat Transfer, **121**(3) pp. 623-631.

[17]. Mukherjee, A., and Dhir, V., 2004, "Study of Lateral Merger of Vapor Bubbles during Nucleate Pool Boiling," Transactions of the ASME-C-Journal of Heat Transfer, **126**(6) pp. 1023-1039.

[18]. Son, G., Ramanujapu, N., and Dhir, V., 2002, "Numerical Simulation of Bubble Merger Process on a Single Nucleation Site during Pool Nucleate Boiling," Journal of Heat Transfer, **124**(1) pp. 51-62.

[19]. Fang, J., 2016, "Development of Advanced Analysis Toolkit for Turbulent Bubbly Flow Simulations." .

[20]. Ghiaasiaan, S.M., 2007, "Two-phase flow, boiling, and condensation: in conventional and miniature systems," Cambridge University Press, .

[21]. Nukiyama, S., 1966, "The Maximum and Minimum Values of the Heat Q Transmitted from Metal to Boiling Water Under Atmospheric Pressure," International Journal of Heat and Mass Transfer, **9**(12) pp. 1419-1433.

[22]. Hsu, Y., 1962, "On the Size Range of Active Nucleation Cavities on a Heating Surface," Journal of Heat Transfer, **84**(3) pp. 207-213.

[23]. Hsu, Y., and Graham, R. W., 1986, "Transport Processes in Boiling and Two-Phase Systems," .

[24]. Howell, J. R., and Siegel, R., 1967, "Activation, Growth, and Detachment of Boiling Bubbles in Water from Artificial Nucleation Sites of Known Geometry and Size," .

[25]. Wang, C., and Dhir, V., 1993, "On the Gas Entrapment and Nucleation Site Density during Pool Boiling of Saturated Water," Journal of Heat Transfer, **115**(3) pp. 670-679.

[26]. Wang, C., and Dhir, V., 1993, "Effect of Surface Wettability on Active Nucleation Site Density during Pool Boiling of Water on a Vertical Surface," Journal of Heat Transfer, **115**(3) pp. 659-669.

[27]. Basu, N., Warrier, G. R., and Dhir, V. K., 2002, "Onset of Nucleate Boiling and Active Nucleation Site Density during Subcooled Flow Boiling," Transactions-American Society of Mechanical Engineers Journal of Heat Transfer, **124**(4) pp. 717-728.

[28]. Theofanous, T., Tu, J., Dinh, A., 2002, "The Boiling Crisis Phenomenon: Part I: Nucleation and Nucleate Boiling Heat Transfer," Experimental Thermal and Fluid Science, **26**(6) pp. 775-792.

[29]. Mikic, B., and Rohsenow, W., 1969, "A New Correlation of Pool-Boiling Data Including the Effect of Heating Surface Characteristics," Journal of Heat Transfer, **91**(2) pp. 245-250.

[30]. Kocamustafaogullari, G., and Ishii, M., 1983, "Interfacial Area and Nucleation Site Density in Boiling Systems," International Journal of Heat and Mass Transfer, **26**(9) pp. 1377-1387.

[31]. Fritz, W., 1935, "Maximum Volume of Vapor Bubbles," Phys.Z, **36**(11) pp. 379-384.

[32]. Basu, N., Warrier, G. R., and Dhir, V. K., 2005, "Wall Heat Flux Partitioning during Subcooled Flow Boiling: Part II—Model Validation," Journal of Heat Transfer, **127**(2) pp. 141-148.

[33]. Plesset, M. S., and Zwick, S. A., 1954, "The Growth of Vapor Bubbles in Superheated Liquids," Journal of Applied Physics, **25**(4) pp. 493-500.

[34]. Forster, H., and Zuber, N., 1954, "Growth of a Vapor Bubble in a Superheated Liquid," Journal of Applied Physics, **25**(4) pp. 474-478.

[35]. Birkhoff, G., Margulies, R., and Horning, W., 1958, "Spherical Bubble Growth," The Physics of Fluids, **1**(3) pp. 201-204.

[36]. Scriven, L., 1959, "On the Dynamics of Phase Growth," Chemical Engineering Science, **10**(1-2) pp. 1-13.

[37]. Mikic, B., Rohsenow, W., and Griffith, P., 1970, "On Bubble Growth Rates," International Journal of Heat and Mass Transfer, **13**(4) pp. 657-666.

[38]. Moore, F. D., and Mesler, R. B., 1961, "The Measurement of Rapid Surface Temperature Fluctuations during Nucleate Boiling of Water," AIChE Journal, **7**(4) pp. 620-624.

[39]. Hendricks, R. C., and Sharp, R. R., 1964, "Initiation of Cooling due to Bubble Growth on a Heating Surface," .

[40]. Cooper, M., and Lloyd, A., 1969, "The Microlayer in Nucleate Pool Boiling," International Journal of Heat and Mass Transfer, **12**(8) pp. 895-913.

[41]. Chi-Yeh, H., and Griffith, P., 1965, "The Mechanism of Heat Transfer in Nucleate Pool Boiling—part I: Bubble Initiaton, Growth and Departure," International Journal of Heat and Mass Transfer, **8**(6) pp. 887-904.

[42]. Griffith, P., and Wallis, J. D., 1958, The Role of Surface Conditions in Nucleate Boiling, .

[43]. LABUNSTO. DA, KOLCHUGI. BA, Golovin, V., 1964, "Study of Growth of Bubbles during Boiling of Saturated Water within a Wide Range of Pressures by Means of High-Speed Moving Pictures," High Temperature, **2**(3) pp. 404-&.

[44]. Pioro, I., Rohsenow, W., and Doerffer, S., 2004, "Nucleate Pool-Boiling Heat Transfer. I: Review of Parametric Effects of Boiling Surface," International Journal of Heat and Mass Transfer, **47**(23) pp. 5033-5044.

[45]. Cole, R., and Rohsenow, W., 1969, "Correlation of bubble departure diameters for boiling of saturated liquids," Chem. Eng. Prog. Symp. Ser, 211 213, **, 65,** pp. 211-213.

[46]. Kocamustafaogullari, G., 1983, "Pressure Dependence of Bubble Departure Diameter for Water," International Communications in Heat and Mass Transfer, **10**(6) pp. 501-509.

[47]. Podowski, M. Z., 2008, "Multidimensional Modeling of Two-Phase Flow and Heat Transfer," International Journal of Numerical Methods for Heat & Fluid Flow, **18**(3/4) pp. 491-513.

[48]. Hsu, Y., and Graham, R. W., 1961, An Analytical and Experimental Study of the Thermal Boundary Layer and Ebullition Cycle in Nucleate Boiling, .

[49]. Hatton, A., 1966, "Photographic study of boiling on prepared surfaces," Proc. Third Int. Heat Transfer Conf., Chicago, Illinois, USA, Aug. 7-12, 1966, **, 4,** pp. 24-37.

[50]. Zuber, N., 1959, Hydrodynamic Aspects of Boiling Heat Transfer (Thesis), .

[51]. Jakob, M., and Fritz, W., 1931, "Versuche Über Den Verdampfungsvorgang," Forschung Im Ingenieurwesen, **2**(12) pp. 435-447.

[52]. Basu, N., Warrier, G. R., and Dhir, V. K., 2005, "Wall Heat Flux Partitioning during Subcooled Flow Boiling: Part 1—model Development," Journal of Heat Transfer, **127**(2) pp. 131-140.

[53]. Young, T., 1832, "An essay on the cohesion of fluids," Abstracts of the Papers Printed in the Philosophical Transactions of the Royal Society of London, The Royal Society, **, 1,** pp. 171-172.

[54]. Wenzel, R., 1936, "Surface Roughness and Contact Angle Ind," Eng.Chem, **28**pp. 988-994.

[55]. Cassie, A., 1948, "Contact Angles," Discussions of the Faraday Society, **3**pp. 11-16.

[56]. Lam, C., Wu, R., Li, D., 2002, "Study of the Advancing and Receding Contact Angles: Liquid Sorption as a Cause of Contact Angle Hysteresis," Advances in Colloid and Interface Science, **96**(1-3) pp. 169-191.

[57]. Ramanujapu, N., and Dhir, V., 1999, Dynamics of Contact Angle during Growth and Detachment of a Vapor Bubble at a Single Nucleation Site, .

[58]. Sobolev, V., Churaev, N., Velarde, M., 2000, "Surface Tension and Dynamic Contact Angle of Water in Thin Quartz Capillaries," Journal of Colloid and Interface Science, **222**(1) pp. 51-54.

[59]. Kandlikar, S. G., Kuan, W. K., and Mukherjee, A., 2005, "Experimental Study of Heat Transfer in an Evaporating Meniscus on a Moving Heated Surface," Journal of Heat Transfer, 127(3) pp. 244-252.

[60]. Fukai, J., Shiiba, Y., Yamamoto, T., 1995, "Wetting Effects on the Spreading of a Liquid Droplet Colliding with a Flat Surface: Experiment and Modeling," Physics of Fluids, **7**(2) pp. 236-247.

[61]. Bussmann, M., Mostaghimi, J., and Chandra, S., 1999, "On a Three-Dimensional Volume Tracking Model of Droplet Impact," Physics of Fluids, **11**(6) pp. 1406-1417.

[62]. Abarajith, H., and Dhir, V., 2002, "A numerical study of the effect of contact angle on the dynamics of a single bubble during pool boiling," ASME 2002 International Mechanical Engineering Congress and Exposition, American Society of Mechanical Engineers, pp. 467-475.

[63]. Son, G., and Hur, N., 2005, "A Level Set Formulation for Incompressible Two-Phase Flows on Nonorthogonal Grids," Numerical Heat Transfer, Part B: Fundamentals, **48**(3) pp. 303-316.

[64]. Mukherjee, A., and Kandlikar, S. G., 2007, "Numerical Study of Single Bubbles with Dynamic Contact Angle during Nucleate Pool Boiling," International Journal of Heat and Mass Transfer, **50**(1-2) pp. 127-138.

[65]. Sato, Y., and Ničeno, B., 2012, "A New Contact Line Treatment for a Conservative Level Set Method," Journal of Computational Physics, **231**(10) pp. 3887-3895.

[66]. Harlow, F. H., and Welch, J. E., 1965, "Numerical Calculation of Time-dependent Viscous Incompressible Flow of Fluid with Free Surface," The Physics of Fluids, **8**(12) pp. 2182-2189.

[67]. Madhavan, S., and Mesler, R. B., 1970, "A Study of Vapor Bubble Growth on Surfaces," International Heat Transfer Conference 4, Begel House Inc., **, 23**.

[68]. Unverdi, S. O., and Tryggvason, G., 1992, "A Front-Tracking Method for Viscous, Incompressible, Multi-Fluid Flows," Journal of Computational Physics, **100**(1) pp. 25-37.

[69]. Tryggvason, G., Bunner, B., Esmaeeli, A., 2001, "A Front-Tracking Method for the Computations of Multiphase Flow," Journal of Computational Physics, **169**(2) pp. 708-759.

[70]. Tryggvason, G., Esmaeeli, A., and Al-Rawahi, N., 2005, "Direct Numerical Simulations of Flows with Phase Change," Computers & Structures, **83**(6) pp. 445-453.

[71]. Esmaeeli, A., and Tryggvason, G., 2004, "Computations of Film Boiling. Part I: Numerical Method," International Journal of Heat and Mass Transfer, **47**(25) pp. 5451-5461.

[72]. Osher, S., and Sethian, J. A., 1988, "Fronts Propagating with Curvature-Dependent Speed: Algorithms Based on Hamilton-Jacobi Formulations," Journal of Computational Physics, **79**(1) pp. 12-49.

[73]. Sussman, M., Fatemi, E., Smereka, P., 1998, "An Improved Level Set Method for Incompressible Two-Phase Flows," Computers & Fluids, **27**(5) pp. 663-680.

[74]. Sussman, M., Smereka, P., and Osher, S., 1994, "A Level Set Approach for Computing Solutions to Incompressible Two-Phase Flow," Journal of Computational Physics, **114**(1) pp. 146-159.

[75]. Son, G., and Dhir, V. K., 2008, "Numerical Simulation of Nucleate Boiling on a Horizontal Surface at High Heat Fluxes," International Journal of Heat and Mass Transfer, **51**(9) pp. 2566-2582.

[76]. Wu, J., Dhir, V. K., and Qian, J., 2007, "Numerical Simulation of Subcooled Nucleate Boiling by Coupling Level-Set Method with Moving-Mesh Method," Numerical Heat Transfer, Part B: Fundamentals, **51**(6) pp. 535-563.

[77]. Fang, J., and Bolotnov, I. A., 2017, "Bubble Tracking Analysis of PWR Two-Phase Flow Simulations Based on the Level Set Method," Nuclear Engineering and Design, **323**pp. 68-77.

[78]. Feng, J., and Bolotnov, I. A., 2017, "Development of Interfacial Forces Closures Based on DNS Data," 17th International Topical Meeting on Nuclear Reactor Thermal Hydraulics (NURETH17), .

[79]. Li, M., Feng, J., and Bolotnov, I., 2017, "Heat Transfer Efficiency in Various Prandtl Number Turbulent Flows using DNS approach," 2017 ANS Annual Meeting, San Francisco, CA.

[80]. Li, M., and Bolotnov, I. A., 2016, "Interface Tracking Simulation of Phase-Change Phenomena: Boiling and Condensation Verification," ASME 2016 conference proceedings, Washington,DC.

[81]. Hirt, C. W., and Nichols, B. D., 1981, "Volume of Fluid (VOF) Method for the Dynamics of Free Boundaries," Journal of Computational Physics, **39**(1) pp. 201-225.

[82]. Ose, Y., and Kunugi, T., 2011, "Development of a Boiling and Condensation Model on Subcooled Boiling Phenomena," Energy Procedia, **9**pp. 605-618.

[83]. Cao, Y., Kawara, Z., Yokomine, T., 2016, "Experimental and Numerical Study on Nucleate Bubble Deformation in Subcooled Flow Boiling," International Journal of Multiphase Flow, **82**pp. 93-105.

[84]. Li, D., and Dhir, V. K., 2007, "Numerical Study of Single Bubble Dynamics during Flow Boiling," Journal of Heat Transfer, **129**(7) pp. 864-876.

[85]. Whiting, C. H., and Jansen, K. E., 2001, "A Stabilized Finite Element Method for the Incompressible Navier-Stokes Equations using a Hierarchical Basis," International Journal for Numerical Methods in Fluids, **35**(1) pp. 93-116.

[86]. Jansen, K. E., 1993, "Unstructured Grid Large Eddy Simulations of Wall Bounded Flows," Annual Research Briefs, Center for Turbulence Research, NASA Ames/Stanford University, pp. 151.

[87]. Sahni, O., Müller, J., Jansen, K., 2006, "Efficient Anisotropic Adaptive Discretization of the Cardiovascular System," Computer Methods in Applied Mechanics and Engineering, **195**(41) pp. 5634-5655.

[88]. Wilcox, D.C., 1998, "Turbulence modeling for CFD," D C W Industries, La Cañada, .

[89]. Tejada-Martínez, A. E., and Jansen, K. E., 2006, "A Parameter-Free Dynamic Subgrid-Scale Model for Large-Eddy Simulation," Computer Methods in Applied Mechanics and Engineering, **195**(23) pp. 2919-2938.

[90]. Nagrath, S., Jansen, K., Lahey Jr, R. T., 2006, "Hydrodynamic Simulation of Air Bubble Implosion using a Level Set Approach," Journal of Computational Physics, **215**(1) pp. 98-132.

[91]. Bolotnov, I. A., 2013, "Influence of Bubbles on the Turbulence Anisotropy," ASME J. Fluids Eng., **135**(5) pp. 051301.

[92]. Fang, J., Cambareri, J. J., Brown, C. S., 2018, "Direct Numerical Simulation of Reactor Two-Phase Flows Enabled by High-Performance Computing," Nuclear Engineering and Design, **330**pp. 409-419.

[93]. Li, M., and Bolotnov A., I., 2018, "Multi-bubble Flow Boiling Simulation using Interface Tracking Method," 2018 International Congress on Advances in Nuclear Power Plants, Charlotte, NC, USA.

[94]. Rasquin, M., Smith, C., Chitale, K., 2014, "Scalable Implicit Flow Solver for Realistic Wing Simulations with Flow Control," Computing in Science & Engineering, **16**(6) pp. 13-21.

[95]. Fang, J., Rasquin, M., and Bolotnov, I. A., 2017, "Interface Tracking Simulations of Bubbly Flows in PWR Relevant Geometries," Nuclear Engineering and Design, **312**pp. 205-213.

[96]. Brackbill, J. U., Kothe, D. B., and Zemach, C., 1992, "A Continuum Method for Modeling Surface Tension," Journal of Computational Physics, **100**(2) pp. 335-354.

[97]. Sussman, M., Almgren, A. S., Bell, J. B., 1999, "An Adaptive Level Set Approach for Incompressible Two-Phase Flows," Journal of Computational Physics, **148**(1) pp. 81-124.

[98]. Sussman, M., and Fatemi, E., 1999, "An Efficient, Interface-Preserving Level Set Re-Distancing Algorithm and its Application to Interfacial Incompressible Fluid Flow," Siam J.on Scientific Computing, **20**(4) pp. 1165-1191.

[99]. Sussman, M., and Smereka, P., 1997, "Axisymmetric Free Boundary Problems," Journal of Fluid Mechanics, **341**pp. 269-294.

[100]. Sethian, A.J., 1999, "Level set methods and fast marching methods," Cambridge University Press, .

[101]. Hewitt, G.F., and Yadigaroglu, G., 2018, "Introduction to Multiphase Flow,"Springer, pp. 39-77.

[102]. Fatemi, E., and Sussman, M., 1995, "An Efficient Interface Preserving Level-Set Re-Distancing Algorithm and its Application to Interfacial Incompressible Fluid Flow," SIAM J Sci Statist Comput, **158**(1) pp. 36.

[103]. Maity, S., 2000, Effect of Velocity and Gravity on Bubble Dynamics.

[104]. Wonnell, L., and Bolotnov, I. A., 2014, "A Study of Bubble Departure as a Function of Contact Angle using Interface Tracking Approach," Master's Supervised Report, .

[105]. Zeng, K., and Bolotnov, I. A., 2016, "Influence of Contact Angle on Interface Evolution using Level Set Method" .

[106]. Li, M., Zeng, K., Wonnell, L., "Development of A New Contact Angle Control Algorithm for Level-Set Method," Journal of Fluids Engineering, .

[107]. Mishra, A., and Bolotnov A., I., 2013, "Contact angle control algorithm development for level-set interface tracking method," Transactions of 2013 ANS Annual Meeting, .

[108]. Celik, I. B., Ghia, U., and Roache, P. J., 2008, "Procedure for Estimation and Reporting of Uncertainty due to Discretization in {CFD} Applications," Journal of Fluids {Engineering-Transactions} of the {ASME}, **130**(7) .

[109]. Clifford, A. A., 1973, "Multivariate Error Analysis: A Handbook of Error Propagation and Calculation in Many-Parameter Systems," .

[110]. Li, M., and Bolotnov, I. A., 2016, "Interface Tracking Simulation of Phase-Change Phenomena: Boiling and Condensation Verification," ASME 2016 Fluids Engineering Division Summer Meeting, **, 1A,** .

[111]. Zuber, N., 1959, Hydrodynamic Aspects of Boiling Heat Transfer (Thesis), .

[112]. Kays, W.M., 2012, "Convective heat and mass transfer," Tata McGraw-Hill Education, .

[113]. Sato, Y., and Niceno, B., 2015, "A Depletable Micro-Layer Model for Nucleate Pool Boiling," Journal of Computational Physics, **300**pp. 20-52.

[114]. Kim, J., 2009, "Review of Nucleate Pool Boiling Bubble Heat Transfer Mechanisms," International Journal of Multiphase Flow, **35**(12) pp. 1067-1076.

[115]. Sharp, R.R., 1964, "The nature of liquid film evaporation during nucleate boiling," National Aeronautics and Space Administration, .

[116]. Jawurek, H., 1969, "Simultaneous Determination of Microlayer Geometry and Bubble Growth in Nucleate Boiling," International Journal of Heat and Mass Transfer, **12**(8) pp. 843IN1847-846IN2848.

[117]. Yabuki, T., and Nakabeppu, O., 2014, "Heat Transfer Mechanisms in Isolated Bubble Boiling of Water Observed with MEMS Sensor," International Journal of Heat and Mass Transfer, **76**pp. 286-297.

[118]. Lee, R., and Nydahl, J., 1989, "Numerical Calculation of Bubble Growth in Nucleate Boiling from Inception through Departure," Journal of Heat Transfer, **111**(2) pp. 474-479.

[119]. Lay, J., and Dhir, V., 1995, "Shape of a Vapor Stem during Nucleate Boiling of Saturated Liquids," Transactions-American Society of Mechanical Engineers Journal of Heat Transfer, **117**pp. 394-394.

[120]. Mallozzi, R., Judd, R. L., and Balakrishnan, N., 2000, "Investigation of Randomness, Overlap and the Interaction of Bubbles Forming at Adjacent Nucleation Sites in Pool Boiling," International Journal of Heat and Mass Transfer, **43**(18) pp. 3317-3330.

[121]. Hutter, C., Sefiane, K., Karayiannis, T., 2012, "Nucleation Site Interaction between Artificial Cavities during Nucleate Pool Boiling on Silicon with Integrated Micro-Heater

and Temperature Micro-Sensors," International Journal of Heat and Mass Transfer, **55**(11-12) pp. 2769-2778.

[122]. Zhang, L., and Shoji, M., 2003, "Nucleation Site Interaction in Pool Boiling on the Artificial Surface," International Journal of Heat and Mass Transfer, **46**(3) pp. 513-522.

[123]. Warrier, G. R., and Dhir, V. K., 2006, "Heat Transfer and Wall Heat Flux Partitioning during Subcooled Flow Nucleate Boiling—a Review," Journal of Heat Transfer, **128**(12) pp. 1243-1256.

[124]. Fang, J., Cambareri, J. J., Rasquin, M., 2018, "Interface Tracking Investigation of Geometric Effects on the Bubbly Flow in PWR Subchannels," Nuclear Science and Engineering, pp. 1-18.

[125]. Bolotnov, I. A., Estrada-Perez, C. E., and Hassan, Y. A., "ITM Simulations of Subcooled Flow Nucleate Boiling Experiment at TAMU," .

[126]. Ren, W., 2016, FY2017 Pilot Project Plan for the Nuclear Energy Knowledge and Validation Center Initiative, .

[127]. Bolotnov, I. A., Jansen, K. E., Drew, D. A., 2011, "Detached Direct Numerical Simulations of Turbulent Two-Phase Bubbly Channel Flow," International Journal of Multiphase Flow, **37**(6) pp. 647-659.

APPENDICES

Appendix.A. Mesh Refinement in PHASTA-used computational meshes

Solidworks is utilized to generate the geometry domains in unstructured mesh simulations. The mesh settings is specified in Attributes.inp including the position, the size and shape of the refinement region. An example is shown below:

```
#refinement around the bubble
-1 3 2 0.025 0.01 0.005 1.0e-3 0 0 0 1.0e-3 0 0 0 1.0e-3
5.0E-05
```

The first three numbers represent a set of special codes to specify the shape of the refinement region. '-1 3 2' denotes cuboid shape (Figure.A. 1) while '-1 3 1' denotes cylinder shape in (Figure A. 2). In the cuboid shape refinement, the following three numbers ('0.025 0.01 0.005') are the center of the refinement region. The rest ('1.0e-3 0 0 0 1.0e-3 0 0 0 1.0e-3') is the

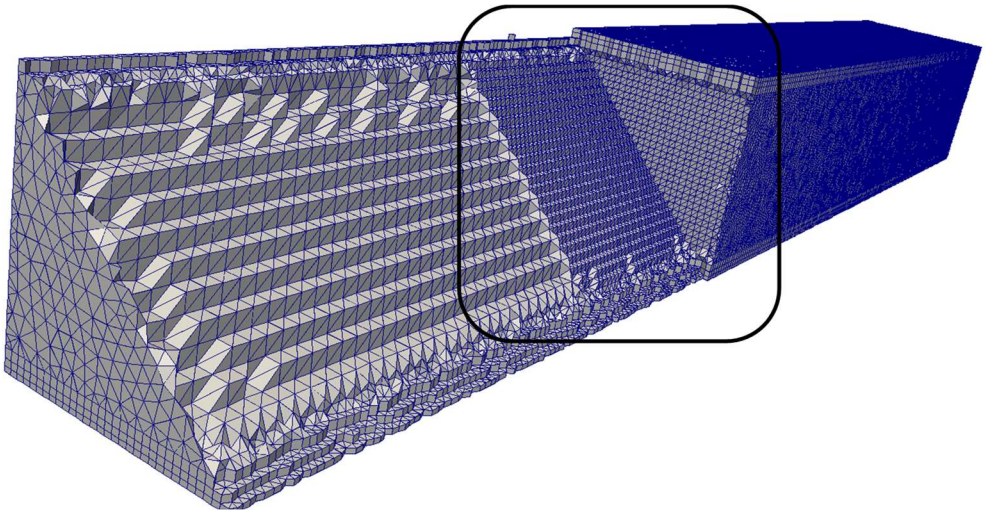

Figure.A. 1. The cuboid shape refinement region.

box half-width in x, y, and z directions. The number in the second line ('5.0E-05') is the refinement resolution. In cylinder shape refinement, the input format is different. The two numbers ('3.5E-03 3.5E-03') after the shape code are the radius and half length of the cylinder. The following three numbers ('0.012 0.005 0.005') are the coordinate of the center of the refinement region. The last

```
#refinement around the bubble
-1 3 1 3.5E-03 3.5E-03 0.012 0.005 0.005 0.000 1.000 0.000
1.4E-04
```

three numbers (‘0.000 1.000 0.000’) is the direction of the cylinder height. The number in the second line (‘1.4E-04’) is the refinement resolution.

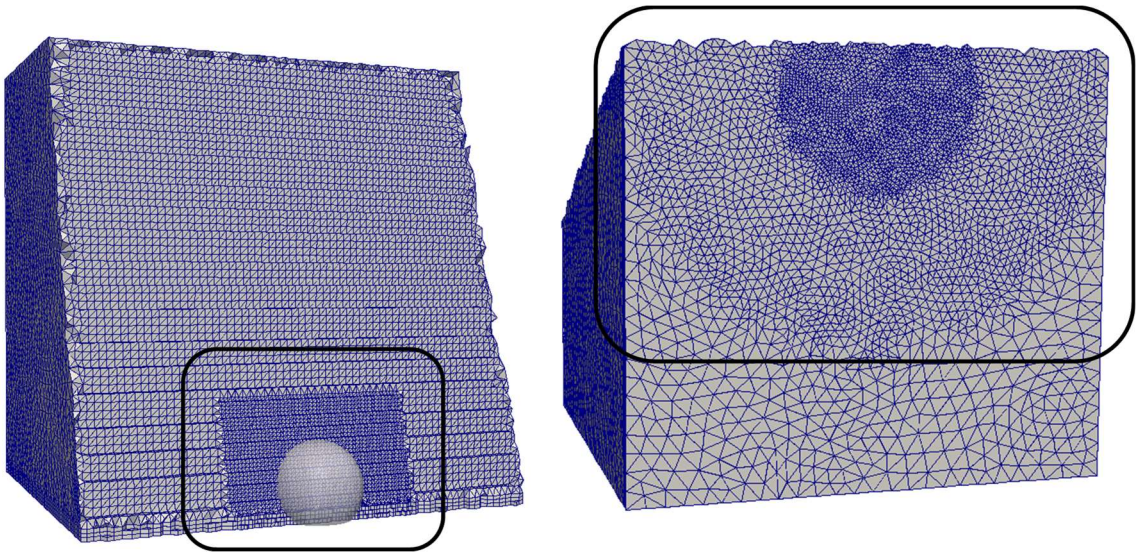

Figure A. 2. The cylinder shape refinement region.

Appendix.B. The Guidelines of Typical Computational Costs for Boiling Simulation

The minimum resolution requirement to fully resolve a single bubble using the ITM (e.g. level set method) is about 18 elements across the bubble diameter[127]. For unstructured meshes, it is possible to apply local refinement to relax bubble resolution in all regions where bubbles are not observed.

Given the information of the anticipated departure diameter and prescribed nucleating sites, it is affordable to model the bubble growth from a very small initial size. Since the departed bubbles can be resolved in the flow domain, the nucleating bubbles only require the resolution at the nucleation sites. Assuming that the diameter of the seeding bubble is D_s and the departure diameter is D_d. The 3D refinement region surrounding the nucleation site must resolve the smallest bubble with N_b elements, which is same as the resolution requirement for the largest bubble (N_b elements across the bubble diameter). The adapted mesh size for this region in the domain can be estimated as:

$$\Delta x_i(r_n) = max\left(\frac{r_n}{N_b}, \frac{D_s}{N_b}\right) \qquad (B - 1)$$

where r_n is the distance to the nucleation site.

The additional meshing requirements for various bubble sizes using local refinement is summarized in Table B-1. As listed in the table, the addition meshing requirements are affordable with hundreds of pre-defined nucleating sites with unstructured meshes and mesh adaptivity. In the nucleate boiling simulation, if 300 randomly distributed pre-defined nucleation sites is introduced to the wall surface of the PWR subchannel and ensure the bubble growing from 0.05mm to departure diameter of 0.5mm. The additional mesh increase is less than 1% compared to the adiabatic simulation.

Table B-1: Adaptive meshing requirement for individual nucleation site.

Bubble initial diameter	Bubble departure diameter	Elements across dimeter	Additional Mesh cost per nucleation site
0.05	0.5	18	128,156
0.05	1.0	18	234,360
0.1	0.5	18	59,584
0.1	1.0	18	128,156
0.2	0.5	18	24,520
0.2	1.0	18	59,584
0.1	0.5	16	46,620
0.1	1.0	16	95,500
0.2	0.5	16	17,604
0.2	1.0	16	46,620

Appendix.C. Prism-shaped Boundary Layer Mesh Design

The prism-shaped boundary layer mesh also is specified in Attributes.inp including the position, the thickness and the number of mesh layers. An example is shown below:

```
#Prim-shaped Boundary Layer Mesh
2 226 1 1 0 0 1E-4 7.44E-4 5 0 0 0
```

where '226' indicates the specific domain face that needs prism-shaped boundary layer, '1 1 0 0' is special code, '1E-4' is the thickness of the first layer, '7.44E-4' is the total thickness of the layers which is recommended to match the element size of the refinement region above the boundary layer region, '5' is the total number of layers applied in the boundary layer region.

Assuming the first layer is h_0, the refinement factor is 1.2, and the element size of the bulk region is h_1, we can use the following calculation sheet to decide the top layer thickness and number of layers needed, for example if $h_1 \approx (1.2^3 + 1.2^2 + 1.2 + 1)h_0$, then the top layer thickness is $(1.2^3 + 1.2^2 + 1.2 + 1)h_0$ and the number of layers needed is 4.

Table C-1: The boundary layer calculation sheet

Layer Number	Element Size of The Layer	Total Thickness
1	h_0	h_0
2	$1.2h_0$	$(1.2 + 1)h_0$
3	1.2^2h_0	$(1.2^2 + 1.2 + 1)h_0$
4	1.2^3h_0	$(1.2^3 + 1.2^2 + 1.2 + 1)h_0$
5	1.2^4h_0	$(1.2^4h_0 + 1.2^3 + 1.2^2 + 1.2 + 1)h_0$
…	…	…

Figure C. 1 presents the comparison between tetrahedralized boundary layer mesh and prism-shaped boundary layer mesh. As observed in Figure C. 1, the shape of the prism-shaped boundary layer mesh has advantage to obtain the accurate representation of the wall normal vector, which is essential for contact angle estimation and thermal and hydrodynamic boundary layer development in the boiling simulation.

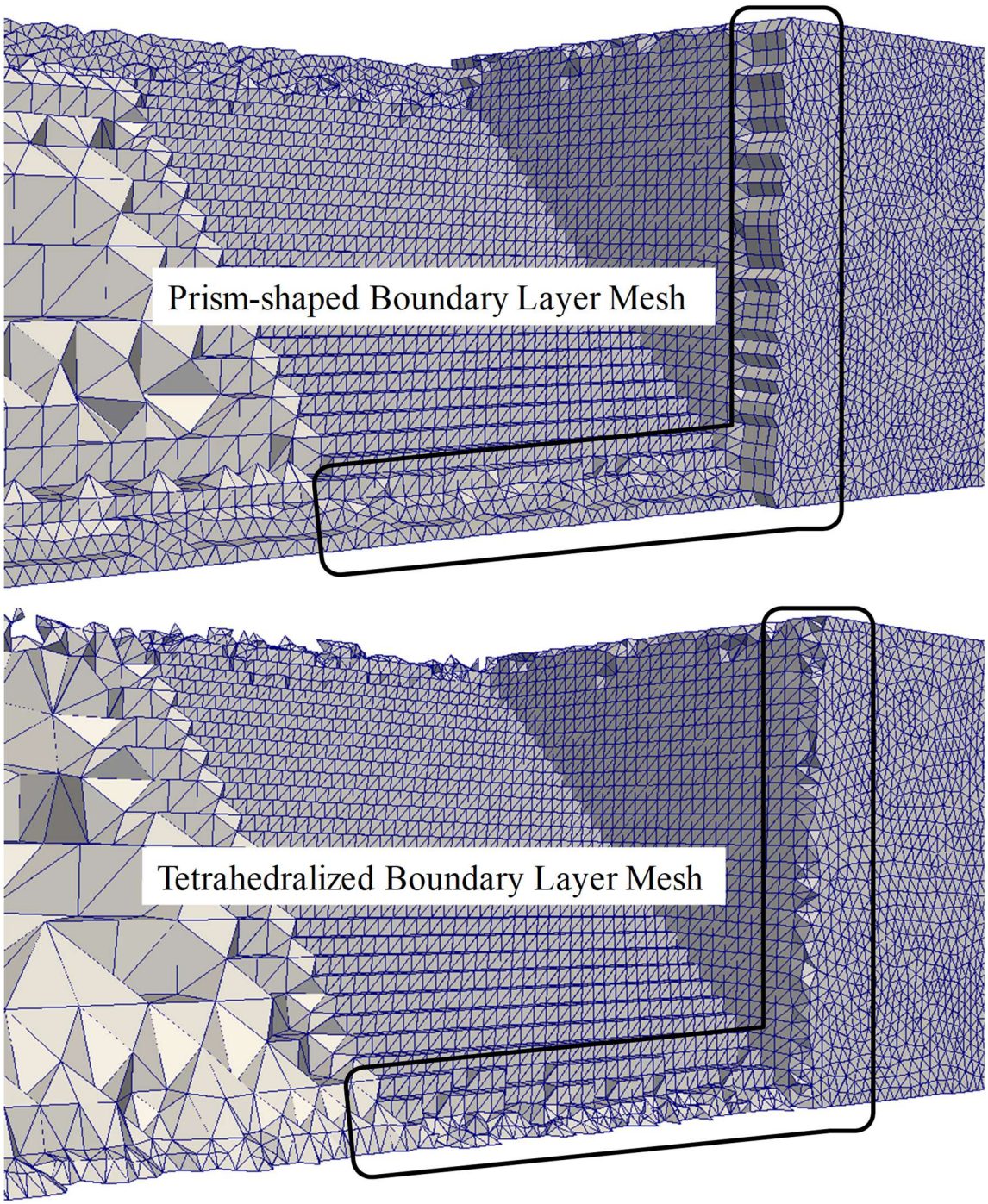

Figure C. 1. The comparison between the tetrahedralized boundary layer mesh and prism-shaped boundary layer mesh.

Appendix.D. The Snap Shots of Bubble Condensation Simulation

The velocity and temperature distribution on the center slice of the domain is presented.

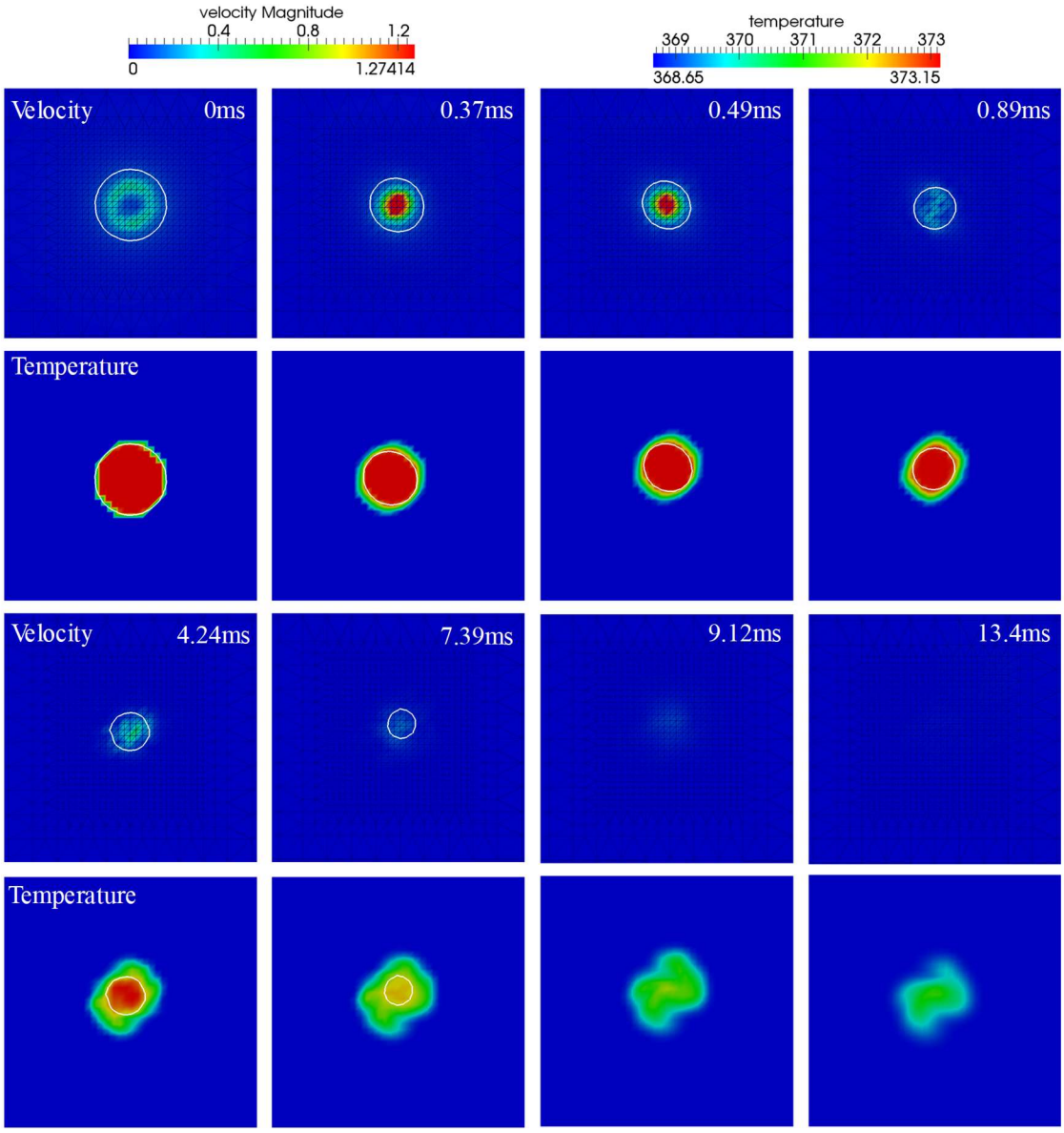

Figure D. 1. The snap shots of the velocity and temperature distribution during bubble condensation.

Appendix.E. The Additional Simulation Results of Nucleate Boiling from Single Site

The nucleation boiling simulation presented here demonstrates that the boiling model is capable of continuing boiling from a single nucleation site. Three successive bubbles depart from the heated bottom wall in sequence. Unlike the validation simulation (Section 5.3), the initial bubble size is larger ($r_{initial} = 0.8mm$) and the domain size is smaller. The mesh design and initial condition are shown in Figure E. 1. The total mesh resolution for this simulation is 0.7 million. The snap shots of temperature distribution (Figure E. 2) and bubble ID field (Figure E. 3) in the center slice of the domain are shown below.

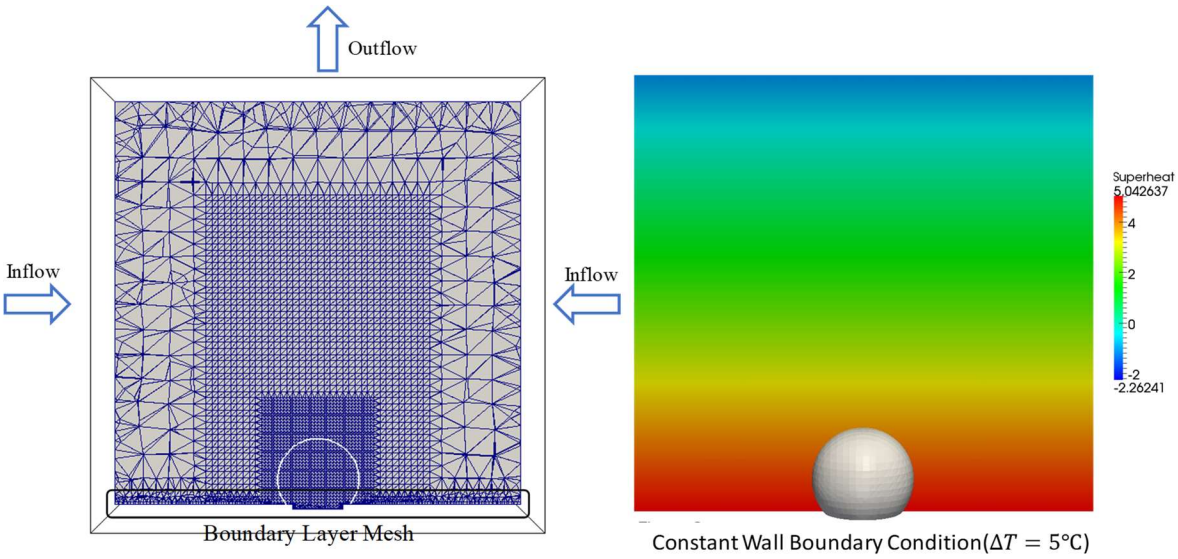

Figure E. 1. The mesh design and the initial condition of the domain in additional nucleation boiling simulation.

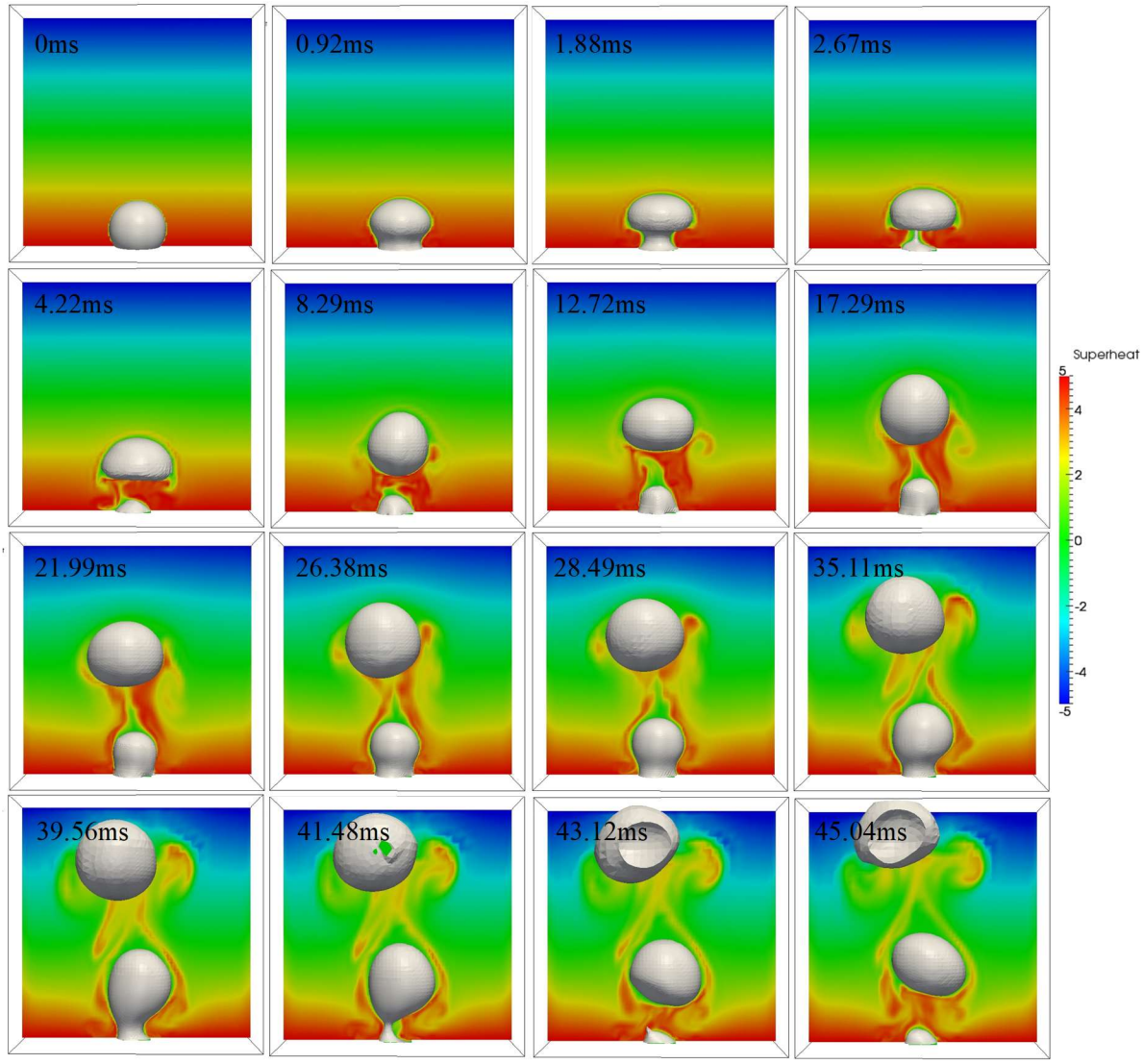

Figure E. 2. The temperature distribution in nucleation boiling simulation. The saturated temperature is 100°C.

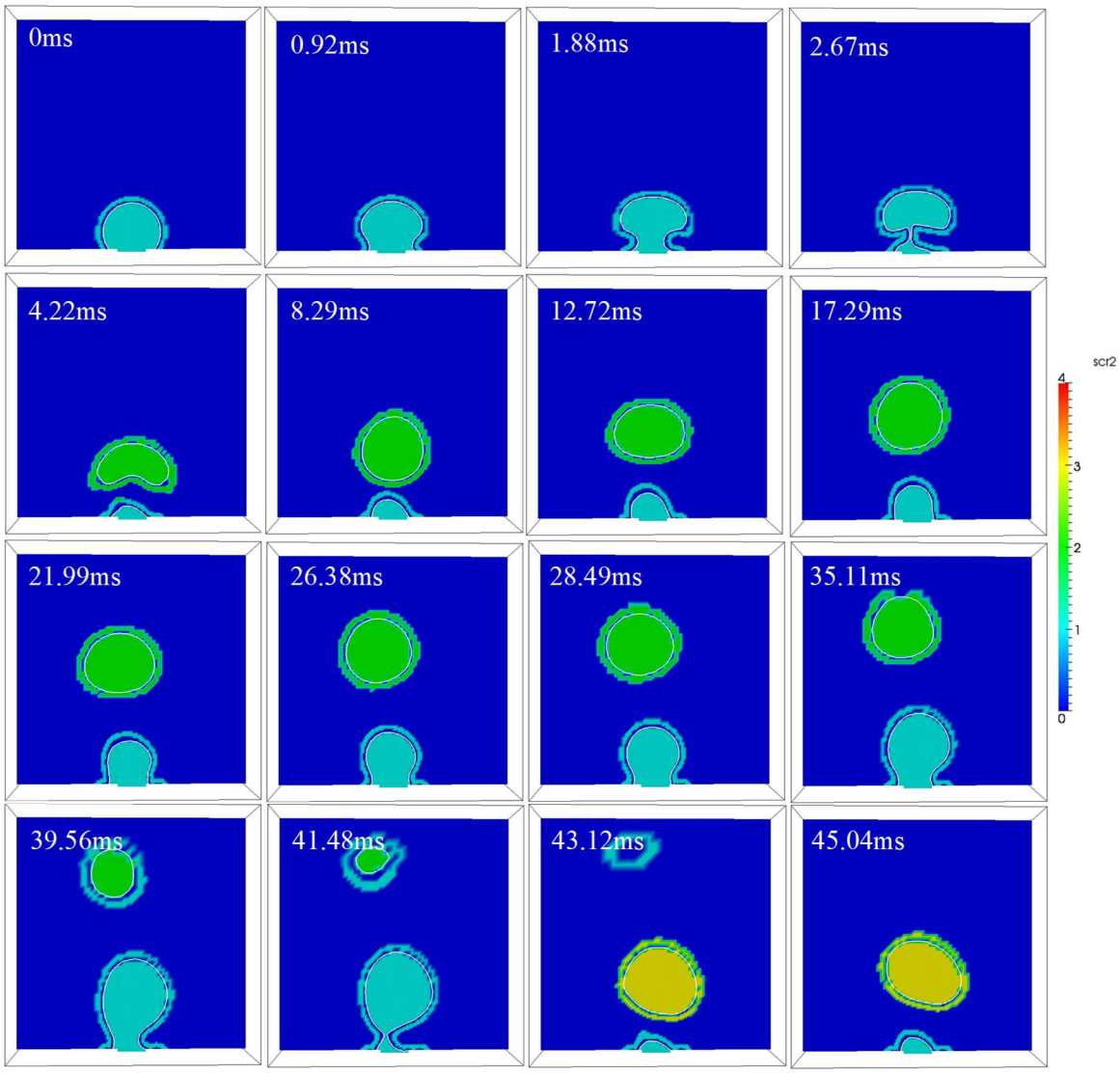

Figure E. 3. The bubble ID field in nucleation boiling simulation. The bubble ID of the nucleating bubble at the nucleation site is set to be '1'.

Appendix.F. The Constant Wall Heat Flux and Constant Wall Temperature Boundary Condition

In heat transfer at a boundary within a fluid, the Nusselt number (Nu) is the ratio of convective to conductive heat transfer across the boundary. If the flow is hydrodynamically and thermally fully developed laminar duct flow, the Nusselt number is,

$$Nu_D = \begin{cases} \dfrac{q''_w}{T_w(x) - T_m(x)} \dfrac{D}{k}, & \text{for uniform heat flux} \\ \dfrac{q''_w(x)}{T_w - T_m(x)} \dfrac{D}{k}, & \text{for constant wall temperature} \end{cases} \quad (D - 1)$$

where q''_w is the constant wall heat flux, T_w is the wall temperature and T_m is the mean temperature of the bulk flow, D is the equivalent dimeter of the duct and k is the thermal conductivity.

The conjugate heat transfer is still on-going work, so the wall temperature is constant in the flow boiling simulation for both thermal boundary condition. Therefore, the corresponding uniform heat flux used in the flow boiling simulation is estimated as,

$$q''_w = \left(T_w - T_m(x)\right) \cdot \frac{D}{k} \cdot Nu_D \quad (D - 2)$$

where $Nu_D = 3.614$ for laminar flow through ducts.

Appendix.G. The Energy Transfer from Heated Wall to The Gas Phase

In the evaporation and condensation model, the temperature of the vapor phase is constant and equal to the saturation temperature, T_{sat}. When the bubble submerges in the superheat liquid, this assumption is valid, and the numerical growth rate has good agreement with the analytical solution. In the nucleate boiling where the bubble is attached to the heated wall before departure, the vapor is directly heated by the wall, but the constant vapor temperature assumption still restricts the vapor temperature to be saturated. The energy transfer from heated wall to the vapor phase is ignored in such condition. This section aims to estimate how much this assumption may affect the total heat transfer from the wall and quantify the error.

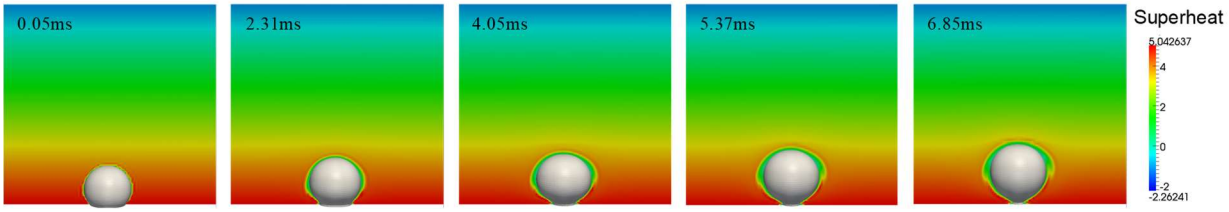

Figure G. 1. The screen shot of the bubble departure from the wall. The background color shows the temperature distribution.

Let's take the single bubble growth and departure case as an example (Section 5.2).The energy transfers from the heated wall to the vapor phase via the area of the bubble base. We define the relative energy transfer ratio between the wall and the vapor phase as,

$$r = \frac{Q_{gas}}{Q_{total}} = \frac{\int_0^{t1} q''_w \cdot S_{base}(t)dt}{\Delta V_{bubble}\rho_g h_{fg}} \qquad (G-1)$$

where q''_w is the wall heat flux, S_{base} is the area of the bubble base, t_1 is the departure time, ΔV_{bubble} is the bubble volume increase before departure, ρ_g is the gas density and h_{fg} is the latent heat.

As observed in Figure G. 1, the bubble volume increases due to the phase-change heat transfer and the base area decreases as the bubble lifts from the wall. Therefore, the relative energy

transfer ratio decreases as the bubble grows. In the single bubble growth and departure case the boiling occurs under atmosphere pressure and the wall heat flux q''_w is equal to $1000\ \mathrm{W/m^2}$. Given contact angle ($\theta = 30°$), the base area (S_{base}) can be express using bubble radius (R) as,

$$S_{base} = \pi(Rsin\theta)^2 \qquad (G-2)$$

Therefore, we can estimate the relative energy transfer ratio using (G - 1). In the single bubble growth and departure case, the relative energy transfer ratio is equal to 0.75%, which means the energy transfer from the wall to the vapor phase is not a main contribution to bubble growth. The maximum vapor temperature increase due to the direct heat from the wall is $0.0528℃$.

As a further step, the relative energy transfer ratio and the maximum vapor temperature increase are estimated in nuclear reactor condition. Assuming the bubble growth rate stays the same, the pressure is selected at $12\mathrm{MPa}$ which is higher than the typical PWR pressure ($7.6\mathrm{MPa}$) but lower than the BWR pressure ($16\mathrm{MPa}$). The thermal properties are listed in Table . The relative energy transfer ratio is calculated to be 0.081% and the maximum vapor temperature increase due to the direct heat from the wall is $0.0038℃$. In reactor condition, the bubble departure diameter and time decrease compared to those in the atmosphere condition. The vapor density, thermal conductivity and specific heat increases due to the high pressure, but at the same time the direct heating time and heating area from the wall to the vapor decrease significantly, which may lead to lower relative energy transfer ratio and the maximum vapor temperature increase in reality.

Table G-1: Thermodynamic properties at 12MPa.

	Water	**Vapor**
Density $\mathrm{kg/m^3}$	878.15	6.13
Thermal conductivity $\mathrm{W/(m \cdot ℃)}$	0.670	0.087
Specific heat $\mathrm{kJ/(kg \cdot ℃)}$	4.438	2.687
Saturation temperature ℃	187.96	
Latent heat kJ/kg	1984.3	

Based on the analysis above, we can conclude that constant vapor temperature assumption is valid for the pool boiling simulation where small bubbles grow on the wall.

Appendix.H. The Evaporation and Condensation Algorithm in PHASTA

H.1. Semi-analytical Growth Model (bubboil.f)

```
48          Rho_l = datmat(1,1,1)  !958
49          Rho_v = datmat(1,1,2) !0.579
50          cp_l = datmat(1,3,1)!1.22
51          k_l = datmat(1,4,1)!0.679
52          dVolume(:) = 1.0e-10
53          shell_num(:)=1.0e-10


56          do i=1, i_num_bubbles
57           if (lstep.lt.1)then
58           elem_shell_num(i) = 2000
59           bubvol(i)=(4.0/3.0)*pi*((2E-4)**3.0)
60           bubble_tempG(i)=1.0E-12
61           else
62           elem_shell_num(i) = numshell_in(i)
63           bubvol(i)=bubble_vol(i)
64           endif
65           R(i) =(((3.0E0/4.0E0)*bubvol(i))/pi)**(1.0E0/3.0E0)
66  !       deactivate the evaporation model for poor resolution bubble
67          if(elem_shell_num(i).le.10.0d0)then
68            bubboil = 0.0
69          else
70            bubboil = 1.0
71          endif


75          if(bubboil.eq.0 .and. bubgrow.eq.1.0d0)then
76           a_l = k_l/(Rho_l*cp_l)
77           B_factor(i) = ((12.0E0*a_l/pi)**(0.5E0))*
78       &             ((delt_T(i)*cp_l*Rho_l)/(h_fg*Rho_v))
79           do j = 1, npro
80               bubdVolume(j,i) = 2.0E0*pi*R(i)*(B_factor(i)**(2.0E0))
81           enddo
82          endif
```

H.2. Thermal Properties at the Interface (getdiff.f)

```
92 !---------Thermal properties mixture for boiling----------------------
---
93           if (solheat.eq.1.0)then
94             do i = 1, npro
95               epsilon_lst_tmp = epsilon_lsd *
96      &                    elem_local_size(lcblk(1,iblk)+i-1)
97               if (sclr(i) .lt. - epsilon_lst_tmp) then
98                  prop_blend(i) = zero
99               elseif  (abs(sclr(i)) .le. epsilon_lst_tmp) then
100                 prop_blend(i) = 0.5*(one + sclr(i)/epsilon_lst_tmp +
101     &                    (sin(pi*sclr(i)/epsilon_lst_tmp))/pi)
102              elseif (sclr(i) .gt. epsilon_lst_tmp) then
103                 prop_blend(i) = one
104              endif
105            enddo
106           cp = datmat(1,3,2)+(datmat(1,3,1)-datmat(1,3,2))*prop_blend
107           k_T = datmat(1,4,2)+(datmat(1,4,1)-datmat(1,4,2))*prop_blend
108!          write(*,*)'rho,cp,k_T',rho,cp,k_T
109          endif
110!----------------------------Mengnan 9/15/15-------------------------
```

H.3. Energy Equation Diffusion Term (e3ql.f)

```
245c.....When isclr=1, heat diffusion term ........Mengnan Li
246          qdi(:,1) =  diffus * gradT(:,1)
247          qdi(:,2) =  diffus * gradT(:,2)
248          qdi(:,3) =  diffus * gradT(:,3)
```

H.4. Energy Equation Advection Term and Source Term (e3res.f)

```
381c.... Na multiplier
382c
383       tmps = one-flmpr  ! consistant mass factor
384       rcp  = one ! rho * cp
385c.............. Heat Advection Term ...................Mengnan Li
386          rNa = rcp*(tmps*Sdot + uMod(:,1) * gradS(:,1)
387     &                         + uMod(:,2) * gradS(:,2)
388     &                         + uMod(:,3) * gradS(:,3))
389     &        - src
```

H.5. Heat Flux Boundary Layer (e3b.f)

```
c
c.... heat or scalar  flux
c
        if(isclr.eq.0) then
           iwalljump=0
        else
           iwalljump=1  !turb wall between heat and scalar flux..jump
over
        endif
        ib=4+isclr+iwalljump
        ibb=6+isclr
        do iel=1, npro
c
c  if we have a nonzero value then
c  calculate the fluxes through this surface
c
           if (iBCB(iel,2) .ne. 0 .and. ires.ne.2) then
              iface = abs(iBCB(iel,2))
              flxID(ibb,iface) =  flxID(ibb,iface)
     &                            - WdetJb(iel) * flux(iel)
           endif

           if (btest(iBCB(iel,1),ib-1)) then
              flux(iel) = zero
              nsurf = (nshl*6.0d0)/(nshl+4.0d0)
              if(ibb.eq.6)then ! Heat flux boundary condition

                 do n = 1, nshlb
                     nodlcl = lnode(n)
                     flux(iel) = flux(iel)
     &                     + shape(iel,nodlcl) * BCB(iel,n,ibb)*nsurf
     &                    *datmat(1,4,1)/(datmat(1,1,1)*datmat(1,3,1))
                 enddo

              else

                 do n = 1, nshlb
                     nodlcl = lnode(n)
                     flux(iel) = flux(iel)
     &                     + shape(iel,nodlcl) * BCB(iel,n,ibb)
                 enddo
              endif
           endif
        enddo
```

H.6. Fixed Saturation Temperature inside The Bubble (itrbc.f)

```
183c....------------Two phase heat conduction Temp BC----------- !6/8/15
Mengnan
184         if(isclr.eq.0 .and. iLSet.eq.2) then
185          do i=1, nshg
186!!          if (y(i,6).GT.0.0) then
187              if (y(i,6).LE.0.0) then
188              y(i,id) = T_sat ! Kelvin
189!            write(*,*) y(i,id)
190              endif
191!            elseif(banma(i,1).eq.1.0d0)then
192!               if (y(i,6).LE.0.0) then
193!               y(i,id) = 307.15 ! Kelvin
194!               endif
195!            endif
196          enddo
197          endif
```

H.7. Local Temperature Gradient Calculation(bubboil.f)

```
160         do i = 1, npro
161           do n = 1, nshl
162             Sclr(i) = Sclr(i) + shpfun(i,n) * yl(i,n,6) !scalar
163c
164c!      .... compute the global gradient of Scalar variable
165c
166             gyti(i,1) = gyti(i,1) + shg(i,n,1) * yl(i,n,6)
167             gyti(i,2) = gyti(i,2) + shg(i,n,2) * yl(i,n,6)
168             gyti(i,3) = gyti(i,3) + shg(i,n,3) * yl(i,n,6)
169c
170           enddo
171         enddo
172c
173c!  .... compute the global gradient of Temperature outside bubble 2
epsilon
174c
175
176
177         do i=1, npro
178          if (lstep.eq.irstart) then
179            R_0(i)=2.0E-4
180!           write(*,*) "R_0", R_0(i)
181          endif
182         enddo
183
184
185        do i=1, npro
186         do k=1, i_num_bubbles
187             do n = 1, nshl
188!                if(INT(bml(i,n,1)).eq.k) then
189               if((INT(bml(i,n,1)).eq.k).or.(INT(bml(i,n,1))
       &             .eq.(3*i_num_bubbles+k)))then
190!              specially for single nucleation site
191                R_0(i)=(((3.0E0/4.0E0)*bubble_vol(k))/pi)
192                R_0(i)=(R_0(i))**(1.0d0/3.0d0)
193
194               endif
195             enddo
196         enddo
197      enddo ! i_num_bubbles
```

```
199         do i = 1, npro
200           do n = 1, nshl
201                  R_1(i) = R_0(i) + 2.0d0*epsilonBT
202           enddo
203
204           if (Sclr(i).le. 2.0E0*epsilonBT
205      &       .and. Sclr(i).ge. 0.0E0*epsilonBT) then
206
207           do n = 1, nshl
                    !Temperature
208                 Tempb(i) = Tempb(i) + shpfun(i,n) * yl(i,n,5)
209                 gytemp(i,1) = gytemp(i,1) + shg(i,n,1) * yl(i,n,5)
210                 gytemp(i,2) = gytemp(i,2) + shg(i,n,2) * yl(i,n,5)
211                 gytemp(i,3) = gytemp(i,3) + shg(i,n,3) * yl(i,n,5)
212           enddo ! for nshl
213
214           gytemp(i,4)=(gytemp(i,1)*gyti(i,1)+gytemp(i,2)*gyti(i,2)
215      &          +gytemp(i,3)*gyti(i,3))
216
217          gytemp(i,5)=gytemp(i,4)*((R_1(i)/R_0(i))**2.0)
      &          *elemvol_local(i)/
218      &          (pi*R_0(i)*R_0(i)*epsilonBT)
219
220
221           else
222             gytemp(i,5)=0.0d0
223             Tempb(i)=0.0d0
224           endif
225
226
227        if(isnan(gytemp(i,5)))  gytemp(i,5) = 0.0d0
228
229      enddo
```

H.8. Average Temperature and Temperature Gradient Estimation with BTA (bubStat.f)

The local temperature and temperature gradient information is collected using **Bubcollect()**. Then the bubble information is assembled in **BubASSY()**. After that the bubble information passes to the MPI process.

```
811          subroutine BubCollect(u1,       u2,     u3,     Sclr, dist2w,
812       &                        xx,       yl,     bml,
elemvol_local,
813       &                        rho,      Tempb,  gytemp,   CurvInfo,
814       &                        CAnode,   CA_vector)
815  !-----------------------------------------------------------------
--
816  !       Called in e3ivar.f
817  !       This subroutine is dealing with the bubble information
818  !       collection at the very bottom level.
819  !       In bub_info(i_num_bubbls, 17)
820  !       bubble-wise: x,y,z coord, vel, elem vol, mass, levelset;
821  !       local liq  : x vel, y vel, z vel, d2wall;
822  !       BT field   : marker(bubble ID)
823  !       Interface curvature is weighted by volume of the interface
824  !       element.
825  !-----------------------------------------------------------------

881               if(Sclr(i) .gt. 2.0d0*epsilonBT) then
882  !-----------------------------------------------------------------
883
884  !       Collect the temperature and its gradient for boiling
885  !       18: temperature around the bubble
886  !       19: temperature gradient around the bubble
887  !       20: number of elements in the shell outside the bubble
888  !       21: number of elements in the shell inside the bubble
889  !       22: The total volume of the outside bubble collection shell
890  !-----------------------------------------------------------------
891                elseif(Sclr(i).gt.epsilonBT) then
892                  bub_info(i,6)  = u1(i)
893                  bub_info(i,7)  = u2(i)
894                  bub_info(i,8)  = u3(i)
895                  bub_info(i,9)  = dist2w(i)
896                  bub_info(i,17) = elemvol_local(i)
897               elseif(Sclr(i).gt.0.0d0) then
898                  bub_info(i,5)  = elemvol_local(i)*denswght*rhogas
899                  bub_info(i,15) = CurvInfo(i)
900
901  !-----------------------------------------------------------------
902                if (bubboil.eq.1.0 .or. bubgrow.eq.1.0)then
903                  bub_info(i,20)= 1.0d0
904                  bub_info(i,18)= Tempb(i)
905                  bub_info(i,19)= gytemp(i,5)
906                 endif
```

```
!=======================================================================
!-----------------------------------------------------------------------
!   This part is for temperature gradient collection
!                       -Mengnan Li
!-----------------------------------------------------------------------
!... Store temperature and temperature gradient around the bubble
!           if(unive_dataset(i,18).ne.0.0)then
            avg_info(i,18) = unive_dataset(i,18)/unive_dataset(i,20)
            avg_info(i,19) = unive_dataset(i,19)
!... Store the number of cell outside the bubble
            avg_info(i,20) = unive_dataset(i,20)
            avg_info(i,21) = unive_dataset(i,21)
!... Store the Contact Angle information
         if(unive_dataset(i,22).ne.0.0d0)then
            avg_info(i,22) = unive_dataset(i,23)/unive_dataset(i,22)
         endif
!           endif
         if(bubboil.eq.1.0.or.bubgrow.eq.1.0) then
            write(*,*)'No.',i,'Bubble'
            write(*,*)'# of elem(out),# of elem(in)',
     &              avg_info(i,20),avg_info(i,21)
         endif
         if(bubboil.eq.1.0.or.bubgrow.eq.1.0) then
            write(*,*)'temp,tempG',
     &              avg_info(i,18),avg_info(i,19)
         endif
```

H.9. MPI Broadcast and Communication (bubStat.f)

```
645         if (numpe.gt.1) then
646
647         do i=1,i_num_bubbles
648
649          if(myrank.eq.master)then
650          bubble_vol_temp    =  unive_dataset(i,4)
651          bubble_tempG_temp =  unive_dataset(i,19)
652          numshell_temp1     =  unive_dataset(i,20)
653          numshell_temp2     =  unive_dataset(i,21)
654          bubble_avgCA_temp =  avg_info(i,22)
655          endif
656 !         write(*,*) 'I am here', bubble_vol(i)
657            call MPI_Bcast(bubble_tempG_temp,1,MPI_DOUBLE_PRECISION,
658      &                          master,MPI_COMM_WORLD,ierr)
659 !           for average temperature gradient
660            call MPI_Bcast(numshell_temp1,1,MPI_DOUBLE_PRECISION,
661      &                          master,MPI_COMM_WORLD,ierr)
662 !           for number of element outside the bubble
663            call MPI_Bcast(numshell_temp2,1,MPI_DOUBLE_PRECISION,
664      &                          master,MPI_COMM_WORLD,ierr)
665 !           for number of element inside the bubble
666            call MPI_Bcast(bubble_vol_temp,1,MPI_DOUBLE_PRECISION,
667      &                        master,MPI_COMM_WORLD,ierr)
668 !           for each bubble vloume
669            call MPI_Bcast(bubble_avgCA_temp,1,MPI_DOUBLE_PRECISION,
670      &                        master,MPI_COMM_WORLD,ierr)
671
672            bubble_vol(i)   =  bubble_vol_temp
673            bubble_tempG(i)=  bubble_tempG_temp
674            numshell_out(i) =  numshell_temp1
675            numshell_in(i) =  numshell_temp2
676            bubble_avgCA   =  bubble_avgCA_temp
677
678         enddo
679
680         endif
```

H.10. Temperature Gradient Driven Growth (bubboil.f)

```
56          do i=1, i_num_bubbles
57           if (lstep.lt.1)then
58           elem_shell_num(i) = 2000
59           bubvol(i)=(4.0/3.0)*pi*((2E-4)**3.0)
60           bubble_tempG(i)=1.0E-12
61           else
62           elem_shell_num(i) = numshell_in(i)
63           bubvol(i)=bubble_vol(i)
64           endif
65           R(i) =(((3.0E0/4.0E0)*bubvol(i))/pi)**(1.0E0/3.0E0)

66  !        deactivate the evaporation model for poor resolution bubble
67           if(elem_shell_num(i).le.10.0d0)then
68             bubboil = 0.0
69           else
70             bubboil = 1.0
71           endif
72
73  !          write(*,*)'R', R
74  !         endif
75           if(bubboil.eq.0 .and. bubgrow.eq.1.0d0)then
76            a_l = k_l/(Rho_l*cp_l)
77            B_factor(i) = ((12.0E0*a_l/pi)**(0.5E0))*
78       &             ((delt_T(i)*cp_l*Rho_l)/(h_fg*Rho_v))
79            do j = 1, npro
80                bubdVolume(j,i) = 2.0E0*pi*R(i)*(B_factor(i)**(2.0E0))
81            enddo
82           endif
83
84           if(bubboil.eq.1.0d0)then ! loop over elements (at the local
level)
85            do j = 1, npro
86                bubdVolume(j,i) = bubble_tempG(i)*k_l
       &                          *(1.0/Rho_v-1.0/Rho_l)/h_fg
87                bubdVolume(j,i) = bubdVolume(j,i)*4.0d0*pi*(R(i)**(2.0))
88            enddo
89           endif
90
91           enddo ! i_num_bubbles
```

```
94          bubboil = 1.0    ! reset boiling flag
95
96  !       Assembly the source matrix
97          do i = 1, i_num_bubbles
98           do j = 1, npro
99
100          epsilon_ls_tmp = epsilon_lst*
101     &       elem_local_size(lcblk(1,iblk)+j-1)
102
103          if ((sclr_ls(j).GT.-2.0E0*epsilon_ls_tmp).and.
104     &        (sclr_ls(j).LT.-1.0E0*epsilon_ls_tmp)) then
105              do n = 1, nshl
106 !                if(INT(bml(j,n,1)).eq.i) then
107
if((INT(bml(j,n,1)).eq.i).or.(INT(bml(j,n,1)).eq.(3*i_num_bubbles+i)))the
n
108 !                 specially for single nucleation site
109                       dVolume(j) = bubdVolume(j,i)
110                       shell_num(j) = elem_shell_num(i)
111                  endif
112             enddo
113          else
114                   dVolume(j) = 0.0d0
115                   shell_num(j) = 0.0d0
116          endif
117          if(isnan(dVolume(j))) dVolume(j) = 0.0d0
118
119
120          enddo
121
122         enddo
```

H.11. Add the volumetric term into continuity equation (e3res.f)

```
257         do i = 1, npro  ! loop over elements (at the local level)
258
259         epsilon_ls_tmp = epsilon_lst *
260      &                   elem_local_size(lcblk(1,iblk)+i-1)
261
262         if ((bubgrow.eq.1.0.or. bubboil.eq.1.0).and.
263      &       (shell_num(i).ge.2.0d0))then
264
265         if ((sclr_ls(i).GT.-2.0E0*epsilon_ls_tmp).and.
266      &     (sclr_ls(i).LT.-1.0E0*epsilon_ls_tmp)) then
267
268!          if(shell_num(i).lt.1.0)
269!       &     write(*,*)shell_num(i)
270
271            do aa = 1, nshl
272                rl(i,aa,4) = rl(i,aa,4) + WdetJ(i)
273      &              * ( shg(i,aa,1) * uBar(i,1)
274      &                + shg(i,aa,2) * uBar(i,2)
275      &                + shg(i,aa,3) * uBar(i,3) )
276      &                + shpfun(i,aa)*(dVolume(i)/shell_num(i)/nshl)
277c           bubsource(i) = bubsource(i) + shpfun(i,aa)
278c     &                   *(dVolume(i)/shell_num(i)/nshl)
279            enddo
280c          write(*,*)'shpfun(i,aa)', shpfun(i,aa)
281
282c           shell_num_old(i)=shell_num_new(i)
283c         if(dVolume(i).ne.0.0d0)write(*,*)
284c     &                   dVolume(i),shell_num(i)
285
286           else
287
288           do aa = 1,nshl
289
290            rl(i,aa,4) = rl(i,aa,4) + WdetJ(i)
291      &              * ( shg(i,aa,1) * uBar(i,1)
292      &                + shg(i,aa,2) * uBar(i,2)
293      &                + shg(i,aa,3) * uBar(i,3) )
294           enddo
295         endif
```

```
296         else
297          do aa = 1,nshl
298
299c
300c.... continuity(without bubble growth)
301c
302             rl(i,aa,4) = rl(i,aa,4) + WdetJ(i)
303      &                 * ( shg(i,aa,1) * uBar(i,1)
304      &                   + shg(i,aa,2) * uBar(i,2)
305      &                   + shg(i,aa,3) * uBar(i,3) )
306          enddo
311          endif  ! boiling flag
312        enddo ! i = 1, npro - loop over elements at local level
```

Appendix.I. Contact Angle Control Algorithm

I.1. Initialization of Contact Angle Control Algorithm (e3ivar.f)

```
153 c... Contact Angle Mengnan
154 ! ------------------------------------------------------------------
155 !------------------------------------------------------------------
156
157            if (CA_flag.eq.1.0d0) then !LBW Summer 2014
158                 gcntang = 0.0 !60.0 !110.0 !60.0
159
160                 interval=5.0 !15.0 !20.0 !10.0
161                 min_delta=25.0 !25.0
162                 mid_taninv=15.0 !15.0
163                 CAnode = zero
164                 flag=1
165                 velmodel=1 !decide which vel model 1: Sine
interpolation, 2: Linear
166 !3: Step
167 !###   Implementaiton of dynamic contact angle
168
169                 delta_high=-0.5   !5!20.0 !5 worked well !
170                 mid_high=20
171                 delta_const_max=40
172
173                 delta_low=-0.5 !5!20.0 !-5 worked well
174                      ! signed minimum deviation from static contact
angle = 40
175                 mid_low=-20
176                 delta_const_min=-40
177                 CA_alpha = 0.2  ! Relaxation factor
178
179                offset_low=(1/2-1/3.141*atan((delta_low-
mid_low)/stretch))
180 !offset along the y axis to ensure continuity of the contact fforce
funciton
181
182                offset_high=(1/2+1/3.141*atan((delta_high-
mid_high)/stretch))
183 !the elusive offset of the tan inverse function along the y axis
184            endif
185 !Ramping constact angle control force
186            if (CAramp.eq.1.0d0)then
187                if (CA_temp.lt.Forcecont)CA_temp = Forcecont
188                    CA_temp = CA_temp + CAF_interval*(lstep-
CA_startT)
189                    if(CA_temp .gt. CAF_upper)then
190                        CA_constant = CAF_upper
191                    else
192                        CA_constant = CA_temp
193                    endif
194                else
195                    CA_constant = Forcecont
196            endif
```

I.2. Estimation of Local Contact Angle for Each Element (e3ivar.f)

```
c! Caculate distance to the wall for Contact Angle:
      if(CA_flag.eq.1.0d0) then
         dist2w = zero
         do n = 1, nenl
            dist2w = dist2w + shpfun(:,n) * dwl(:,n)
         enddo
      endif

c! Caculate distance to the wall for Contact Angle:
      if(CA_flag.eq.1.0d0) then
         x2w = zero
         y2w = zero
         z2w = zero
         do n = 1, nenl
            x2w = x2w + shpfun(:,n) * xwl(:,n)
            y2w = y2w + shpfun(:,n) * ywl(:,n)
            z2w = z2w + shpfun(:,n) * zwl(:,n)
         enddo
      endif

c ...    Contact Angle Mengnan  ------------------------------------
       if(CA_flag.eq.1.0d0) then

       wnrm_new(1) = (-x2w(i))/(dist2w(i))
       wnrm_new(2) = (-y2w(i))/(dist2w(i))
       wnrm_new(3) = (-z2w(i))/(dist2w(i))


       cntfdir(i,:)=gyti(i,:)-wnrm_new(:)*gyti(i,:)
! opoints towards outward direction of bubble
       cntfdir(i,:)=cntfdir(i,:)
     &  /sqrt(cntfdir(i,1)**2+cntfdir(i,2)**2+cntfdir(i,3)**2)
!dynamic contact angle implentation contact line speed
      CLS=u1(i)*cntfdir(i,1)+u2(i)*cntfdir(i,2)+u3(i)*cntfdir(i,3)

!model
      CLS_max=1.0E-2
      if(velmodel.eq.1) then ! sine model

        if(CLS.ge.CLS_max) gcntang=theta_adv
        if(CLS.le.-1.0*CLS_max) gcntang=theta_rec
        if(CLS.gt.-1.0*CLS_max.and.CLS.lt.CLS_max) then
      gcntang=theta_adv/2.0*(sin(3.141*CLS/(2.0*CLS_max))+1)
     &         -theta_rec/2.0*(sin(3.141*CLS/(2.0*CLS_max))-1)
       endif
```

```
567         elseif(velmodel.eq.2) then ! linear model
568
569           if(CLS.ge.CLS_max) gcntang=theta_adv
570           if(CLS.le.-1.0*CLS_max) gcntang=theta_rec
571           if(CLS.gt.-1.0*CLS_max.and.CLS.lt.CLS_max) then
572         gcntang=(theta_adv-theta_rec)/(2*CLS_max)*CLS
573        &          +(theta_rec +theta_adv)/2.0
574            endif
575         elseif(velmodel.eq.3) then ! step model
576
577 !       if(myrank.eq.master) Write(*,*)  "step model",velmodel
578
579           if(CLS.ge.0.0) gcntang=theta_adv
580           if(CLS.le.0.0) gcntang=theta_rec
581
582         endif !end selection of models

586 ! initially before looping over the nodes in a block avgspeed was
zero now it
587 ! will add up within the bubble
588
589         if(sclr(i).le.0.0) then
590            avgspeed=avgspeed+sqrt(u1(i)*u1(i)+u2(i)*u2(i)+u3(i)*u3(i))
591            bubnode=bubnode+1
592         endif
596 ! find contact angle
597
cos_contact=(gyti(i,1)*x2w(i)+gyti(i,2)*y2w(i)+gyti(i,3)*z2w(i))
598        &
/((gyti(i,1))**2.0D0+(gyti(i,2))**2.0D0+(gyti(i,3))**2.0D0)**0.5
599        & /(dist2w(i))
600
601 !        if(myrank.eq.master)write(*,*)'cos_contact',cos_contact
602
603         if  (cos_contact.lt.0) then
604
605            contact_angle=180.0-acos(-cos_contact)*180.0/3.141
606         else
607            contact_angle=acos(cos_contact)*180.0/3.141
608         endif
609
610         upperlimit = max(bubble_avgCA, gcntang)
611         lowerlimit = min(gcntang, bubble_avgCA)
615
if((contact_angle.gt.upperlimit).and.(upperlimit.ne.0.0))then
616           contact_angle = (1-CA_alpha)*bubble_avgCA +
CA_alpha*contact_angle
617              elseif(contact_angle.lt.lowerlimit)then
618           contact_angle = (1-CA_alpha)*bubble_avgCA +
CA_alpha*contact_angle
619           endif
```

```
623         delta_contact=(gcntang-contact_angle)
624
625 !-----------------------initial guess ends--------------------------
---------
626 !         Print *, "Contact Angle Section Line 543"
627
628 ! find if current contact angle is what we want
629          if((delta_contact.gt.delta_low)
630       &      .and.(delta_contact.lt.delta_high))then
631                                CA_achieved2(i)=.true.
632                  else
633                                CA_achieved2(i)=.false.
634          endif
```

I.3. Estimation of The Contact Angle Control Force (e3ivar.f)

```
635 ! if we are not in the force application region then we don't
consider contact
636 ! angle and node. so putting them to zero:
637                       F_app=0.0
638                       CA_vector(i)=0.0
639                       contact_force_vector(i)=0.0
640
641                       tag(i)=0  ! tag 0 is not in advancing region, 1
advancing, 2
642                                 ! receding
643     !                      Print *, "Contact Angle Section Line 560"
644                        if (i_spat_var_eps_flag.eq.0) then
645                           eps_thick = epsilon_ls*Fapp_thick
646                           eps_height = epsilon_ls*Fapp_heigh
647
648                        elseif ((i_spat_var_eps_flag.eq.1)
649       &                      .or.(i_spat_var_eps_flag.eq.2)) then
650                           epsilon_ls_tmp = epsilon_ls*
651       &                   elem_local_size(lcblk(1,iblk)+i-1)
652                           eps_thick = epsilon_ls_tmp*Fapp_thick
653                           eps_height = epsilon_ls_tmp*Fapp_heigh
654                        endif
655 c-----------------------------------------------------------------------
656
c_______________________________________________________________________
657 !              Print *, "Contact Angle Section Line 567"
658 ! FORCE APPLICATION REGION
659 !           if (1.eq.0) then ! Initial force formulation to disable
force
660 !           if ((sclr(i)).le.Fapp_thick*eps.and.
661
662 !            if(sclr(i).le.Fapp_thick*eps.and.sclr(i).ge.0.0.and.
663             if(abs(sclr(i)).le.eps_thick.and.(dist2w(i).le.eps_height)
664       &          .and.(.not.CA_achieved2(i)))then
665
666                if(delta_contact.le.delta_const_min) then
667                   delta_contact=delta_const_min
668                elseif(delta_contact.ge.delta_const_max) then
669                   delta_contact=delta_const_max
670                endif
671
```

```
672 !............INITIAL FPRCE FORMULATION.............................
673
674
675                if (delta_contact.le.delta_low) then ! push interface
in
676                   F_app=CA_constant*
677       &      (-1.0/2.0+1.0/3.141*atan((delta_contact-mid_low)/stretch)
678       &                 +offset_low)*cos(sclr(i)*3.141/2.0/(eps_thick))
679       &                   *(eps_height-dist2w(i))**2.0*rho(i)
680                elseif(delta_contact.ge.delta_high) then ! pull
interface out
681
F_app=CA_constant*(1.0/2.0+1.0/3.141*atan((delta_contact-
682       &                           mid_high)/stretch)-offset_high)
683       &                           *cos(sclr(i)*3.141/2.0/(eps_thick))
684       &                           *(eps_thick-dist2w(i))**2.0*rho(i)
685
686
687                 else
688
689                         F_app=0.0
690                 endif
691
692
693                sforce(i,:) = sforce(i,:) + F_app*cntfdir(i,:)
```

I.4. Contact Angle Information Output (e3ivar.f)

```
696           if(abs(sclr(i)).le.eps_thick.and.
697      &      (dist2w(i).le.eps_height).and.
698      &      (.not.CA_achieved2(i))) then
699           if (lstep.eq.5) then
700 !               open(unit=3460, file="FAR_Coord.txt")
701 !               open(unit=3461, file="CA_Force.txt")
702 !               open(unit=3462, file="wnrm.txt")
703 !               open(unit=3463, file="wnrm_new.txt")
704 !               open(unit=3464, file="TotalForce.txt")
705 !               open(unit=3465, file="Eps.txt")
706 !               open(unit=3466, file='Contact_angle.txt')
707 !               open(unit=3467, file='CAF_direction.txt')
708 !
709 !               write(3460,*) xl(i,1,1),xl(i,1,2),xl(i,1,3)
710 !               write(3461,*) F_app
711 !               write(3462,*) wnrm(i,1), wnrm(i,2), wnrm(i,3)
712 !               write(3463,*) wnrm_new(1), wnrm_new(2), wnrm_new(3)
713 !               write(3464,*) sforce(i,1), sforce(i,2), sforce(i,3)
714 !               write(3465,*) epsilon_ls_tmp, eps_thick, eps_height
715 !               write(3466,*) contact_angle, delta_contact
716 !               write(3467,*) cntfdir(i,1),cntfdir(i,2), cntfdir(i,3)
717           endif
718
719           ! out of Force application region, end of writing
720           endif
721
722         endif ! ENDING FORCE APPLICATION REGION IF STATEMENT
723 !                 Print *, F_app,rho(i),cntang,gcntang
724 !                  Print *, "gcntang", gcntang !LBW
725
726
727           if(abs(sclr(i)).le.eps_thick.and.
728      &      (dist2w(i).le.eps_height).and.
729      &      (.not.CA_achieved2(i))) then
730                CAnode(i)=1.0d0
731                CA_vector(i)=contact_angle
732                contact_force_vector(i)=F_app
733 !           Print *, "Contact Angle Section Line 683"
734           endif
735
736          endif !contactangle_flag
```

Appendix.J. Continuing Nucleate Boiling Algorithm

J.1. Breakup Detector for Nucleating Bubble (bubStat.f)

```
1246              bub2w_temp = YLEN*0.5d0-abs(Ymid-bub2w(ib,2))
1247              D_eq_temp1 = D_eq(ib)*breakup2w     !0.64d0
1248              D_eq_temp2 = D_eq(ib)*(breakup2w + 1.5d0)
1249!              write(*,*)breakup2w
1250              if((mod(lstep,10).eq.0).and.
1251         &
(bub2w_temp.gt.D_eq_temp1).and.(bub2w_temp.lt.D_eq_temp2))
1252         &       iseeding     = 1
1253              write(*,*)bub2w_temp,D_eq_temp1
```

J.2. Breakup Confirmation for Nucleating Bubble (bubStat.f)

```
1238         do ib = 1,i_num_bubbles
1239!             write(*,*) 'breakupSeeder in detector 1= ',
1240!     &                  breakupSeeder(ib,:)
1241             iseeding     = 0
1242             breakupSeeder(ib,1) = real(ib)
1243             iactionFlag  = int(breakupSeeder(ib,2))
1244             if(iactionFlag.eq.0.and.avg_info(ib,4).gt.0.0d0) then
1245             iauxBubID    = int(breakupSeeder(ib,1))
1246             bub2w_temp = YLEN*0.5d0-abs(Ymid-bub2w(ib,2))
1247             D_eq_temp1 = D_eq(ib)*breakup2w    !0.64d0
1248             D_eq_temp2 = D_eq(ib)*(breakup2w + 1.5d0)
1249!             write(*,*)breakup2w
1250             if((mod(lstep,10).eq.0).and.
1251      &
(bub2w_temp.gt.D_eq_temp1).and.(bub2w_temp.lt.D_eq_temp2))
1252      &       iseeding     = 1
1253             write(*,*)bub2w_temp,D_eq_temp1
1254!    more sophisticated condition can be developed to determine when
1255!    setting iseeding to be 1.
1256             if(iseeding.eq.1) then
1257!             if(lstep+1.eq.17403) then
1258!                write(*,*) 'ID seeding is switched on manually'
1259                iPossibleBreakup = iPossibleBreakup + 1
1260                iactionFlag      = 1
1261                iauxBubID        = 3*MaxAuxID + iPossibleBreakup
1262             endif
1263
1264             breakupSeeder(ib,2) = real(iactionFlag)
1265             breakupSeeder(ib,3) = avg_info(ib,14)
1266             breakupSeeder(ib,6) = real(iauxBubID)
1267
1268             endif !iactionFlag = 0
1269!             write(*,*) 'breakupSeeder in detector = ',
1270!     &                  breakupSeeder(ib,:)
1271
1272         enddo  !ib
```